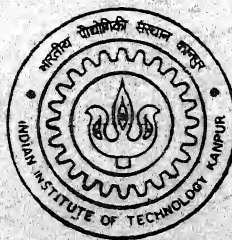


# BUOYANCY DRIVEN FLOW IN SUPERIMPOSED AIR-WATER LAYERS

by  
**ANAMIKA SETHIA**



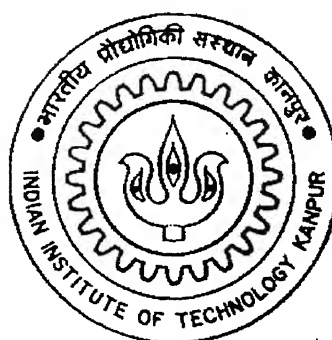
TH  
LT/2001/M  
Sc 75b

**LASER TECHNOLOGY PROGRAMME**  
**Indian Institute of Technology, Kanpur**  
**April, 2001**

# **BUOYANCY DRIVEN FLOW IN SUPERIMPOSED AIR-WATER LAYERS**

A THESIS SUBMITTED  
IN PARTIAL FULFILMENT OF THE REQUIREMENTS  
FOR THE DEGREE OF  
**MASTER OF TECHNOLOGY**

by  
**Anamika Sethia**



**LASER TECHNOLOGY PROGRAMME  
INDIAN INSTITUTE OF TECHNOLOGY KANPUR  
April 2001**

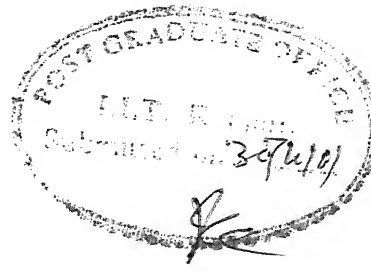
18 JUL 2001/

प्रबोधन प्रदीपक लेखक पुस्तकालय  
भारतीय प्रौ. वि. संस्थान कानपुर  
अवधि क्र० A...134238...

TH  
LT/2001/M  
Se75 b



A134238



## CERTIFICATE

It is certified that the work contained in the thesis entitled "*Buoyancy Driven Flow In Superimposed Air-Water layers*", by *Ms. Anamika Sethia*, has been carried out under my supervision and that this work has not been submitted elsewhere for a degree.

K Muralidhar

K. Muralidhar

Professor

Dept. of Mechanical Engineering and

Laser Technology Programme

I.I.T. Kanpur 208016

April, 2001



# Abstract

Buoyancy-driven flow in a superimposed air-water layer has been experimentally studied, using a Mach-Zehnder interferometer. Two methodologies were employed, namely experimental and numerical. The cavity containing the fluid layers has dimensions of  $447 \times 32.1 \times 32.1 \text{ mm}^3$ . The cavity temperature difference was maintained at  $\Delta T = 10^\circ\text{C}$  during the experiments. The fluid properties and Rayleigh numbers have been evaluated at the average cavity temperature. The sequence of experiments conducted were with a (i) cavity filled with air, (ii) cavity filled with water and (iii) cavity half-filled with water. All fringe patterns have been recorded in the infinite fringe setting of the interferometer. The experiments have been conducted till steady state is reached.

To examine the experimental results, a two-dimensional numerical simulation has been carried out for flow and heat transfer in air ( $\text{Pr} = 0.71$ ) and liquid metal ( $\text{Pr} = 0.05$ ). Closed as well as open cavities have been considered.

The present research is directed towards examining the following issues: (a) the influence of Rayleigh number on the steady thermal field, (b) the transient evolution of the thermal field at a given Rayleigh number, (c) temperature distribution at the interface, (d) heat flux at the solid wall, and (e) the shape of the interface

In air, a steady state two-dimensional convection pattern was observed. The average Nusselt number for the cavity matched well with the published correlations. In water filled cavity, due to an extremely high Rayleigh number, unsteady and turbulent flow was observed. For a cavity half-filled with water, the interface temperature calculated from the water side was found to be quite close to that from the air side. The direction of circulation in the air phase was found to depend on the average cavity temperature. For a cavity average temperature of  $21^\circ\text{C}$ , mechanical coupling was observed between the two layers and for  $29^\circ\text{C}$ , thermal coupling was observed.

# ACKNOWLEDGMENT

I express my sincere gratitude, regards and thanks to my supervisor Prof. K. Muralidhar for his excellent guidance, invaluable suggestions and generous help at all the stages of my research work. It is indeed very difficult to find words to thank him for the kind of motivation and the urge for academic pursuits he instilled in me. His interest and confidence in me was the reason for all the success I have made.

I am grateful to Dr. P.K.Panigrahi for his help and suggestions extended on different occasions during my thesis.

Special thanks to Mr. Shambhunath Sharma for the fabrication of my experimental setup and other accessories.

My parents were a constant source of encouragement for me throughout this work. They provided a fruitful environment to carry out my research successfully. Due to their blessings, I have successfully completed my work.

I extend my sincere gratitude to Mr. Sunil Punjabi and Mr. Atul Srivastava for their timely suggestions and the much needed encouragement during the course of my thesis work.

I am thankful to Mr. Andallib Tariq, Mr. Debashish Karmakar, Mr. Sushanta Dutta, Ms. Tanuja Sheroy to help me in software and graphics related problems. I am thankful to all the persons of Central Workshop, Glass blowing section for helping me.

I take this opportunity to thank Mr. Subrata Samanta, Mr. Tara Singh Chahar, Mr. Sangram Singh Swain, Mr. Vivek Singh and Mr. Srinivas Rao for giving me a good company and encouraging, helpful atmosphere in the laboratory.

At last I am thankful to the All Mighty for giving me enough perseverance, patience and strength to rise after every debacle.

**Anamika Sethia**

# Contents

Certificate	1
Abstract	1
Acknowledgements	2
List of Figures	xii
Nomenclature	xv
<b>1 Introduction</b>	<b>1</b>
1.1 Convection in Fluids	1
1.2 Literature Review based on the Two Layer Convection	3
1.2.1 Analytical studies	3
1.2.2 Numerical studies	4
1.2.3 Experimental studies	5
1.3 Objectives of the present study	5
<b>2 Apparatus and Instrumentation</b>	<b>7</b>
2.1 Laser Interferometry	10
2.2 Alignment of the Interferometer	13
2.3 Experimental Procedure	14
2.4 Uncertainty and Measurement errors	16
<b>3 Data Reduction</b>	<b>17</b>
3.1 Interferometry	18
3.2 Image Enhancement	20
3.3 Calculation of Fringe Temperatures	24
3.4 Nusselt Number Calculations	26
<b>4 Results and Discussion</b>	<b>27</b>
4.1 Convection in air	28
4.2 Convection in a water filled cavity	39
4.3 Convection in a cavity half filled with water	42
4.3.1 Convection in the air phase	42
4.3.2 Convection in the water phase	45
4.3.3 Experiments with a new set of surface temperatures	52
<b>5 Conclusions and Scope for Future Work</b>	<b>58</b>
<b>Appendix A</b>	<b>62</b>

---

<b>A</b>	<b>Numerical Simulation for Interface Temperature</b>	<b>63</b>
A.1	Design of Test Cell . . . . .	63
<b>Appendix B</b>		<b>66</b>
<b>B</b>	<b>Numerical Simulation of Fluid Flow and Heat Transfer</b>	<b>67</b>
B.1	Numerical Simulation for $Ra=10,000$ and $Pr=0.05$ . . . . .	75
B.2	Effect of Surface-Tension on the shape of the Free Surface . . . .	80

# List of Figures

2.1	Schematic of the Test-cell	8
2.2	Various flow regimes in a horizontal fluid layer heated from below	9
2.3	Schematic Drawing of the Mach-Zehnder Interferometer	11
2.4	Schematic Drawing of the Traversing mechanism	11
2.5	Infinite Fringe Setting of the Interferometer	14
2.6	Complete View of the Experimental Setup	15
2.7	Closer View of the Test Cell	15
3.1	An Original Interferogram	21
3.2	Filtered Interferogram	21
3.3	Contrast Improved Interferogram	22
3.4	Superimposed Thinned Image with Original Image	23
3.5	Thinned Image	24
3.6	Schematic of an Idealized Fringe Skeleton for Temperature Calculations	25
4.1	Infinite Fringe setting (a) without and (b) with Candle Flame	29
4.2	Evolution Patterns for Air without Windows for $T_c=16^\circ\text{C}$ , $T_h=26^\circ\text{C}$ and $Ra=34,200$	29
4.3	(a) Original Interferogram (b) Filtered Interferogram (c) Thinned Image (d) Superimposed Thinned images for air when the cavity is filled with Air for $Ra=34,200$	31
4.4	Temperature Profiles in Air filled cavity for $Ra=34,200$ for (a) $x=1.07\text{ mm}$ and (b) $x=21.4\text{ mm}$	32

4.5	Local Nusselt number variation at the top and bottom walls	32
4.6	Infinite Fringe setting (a) without and (b) with Candle Flame in a Water filled Cavity	34
4.7	Evolution Patterns for Air with Optical Windows for $T_c=16^\circ\text{C}$ , $T_h=26^\circ\text{C}$ and $Ra=34,200$	34
4.8	(a) Original Interferogram (b) Filtered Interferogram (c) Thinned Image (d) Superimposed Thinned images for Air when the cavity is with optical windows for $Ra=34,200$	36
4.9	Fourier Filtered images with different filtering parameters (a) cutoff=50, (b) cutoff=100, (c) Thinned Image (d) Superimposed Thinned Image	37
4.10	Temperature Profiles for two equally spaced columns of cavity (a) $x=1.07$ mm and (b) $x=21.4$ mm	38
4.11	Local Nusselt number variation at the top and bottom walls for Air when cavity is with optical windows for $Ra=34,200$	38
4.12	Infinite Fringe setting (a) without and (b) with Candle Flame in a Water filled Cavity	40
4.13	Evolution Patterns for Water for $T_c=16^\circ\text{C}$ , $T_h=26^\circ\text{C}$ and $Ra=16,69314$	40
4.14	(a) Original Interferogram (b) Filtered Interferogram (c) Thinned Image (d) Superimposed Thinned image for water for $Ra=16,69,314$	41
4.15	Infinite Fringe setting (a) without and (b) with Candle Flame	43
4.16	Evolution Patterns for air when the cavity is half filled with water for $T_c=16^\circ\text{C}$ , $T_h=26^\circ\text{C}$ and $Ra_{air}=4,185$ and $Ra_{water}=16,413$	43
4.17	(a) Original Interferogram (b) Filtered Interferogram (c) Thinned Image (d) Superimposed Thinned Image for Air for $T_c=16^\circ\text{C}$ , $T_h=26^\circ\text{C}$ and $Ra_{air}=4,185$ and $Ra_{water}=16,413$	44

4.18	(a) Infinite Fringe setting without and (b) with Candle Flame	46
4.19	Evolution Patterns for Water when the cavity is half filled with water for $T_c=16^\circ\text{C}$ , $T_h=26^\circ\text{C}$ and $Ra_{air}=4,185$ and $Ra_{water}=16,413$	46
4.20	(a) Original Interferogram (b) Filtered Interferogram (c) Thinned Image (d) Superimposed Thinned Image for Water when the cavity is half filled with water for $Ra_{air}=4,185$ and $Ra_{water}=16,413$	47
4.21	(a) Raw image with extraneous features and (b) Modified image	48
4.22	Steady state pattern for (a) air and (b) water	49
4.23	Temperature Profiles in the cavity half filled with water at (a) $x=1.07$ mm and (b) $x=21.4$ mm	50
4.24	(a) Local Nusselt number variation at top and bottom walls (b) Rolls formation in air and water	50
4.25	Infinite Fringe setting (a) without and (b) with Candle Flame	53
4.26	Evolution Patterns for Air when the cavity is half filled with Water for $T_c=24^\circ\text{C}$ , $T_h=26^\circ\text{C}$ , $Ra_{air}=3,699$ and $Ra_{water}=22,350$	53
4.27	(a) Original Interferogram (b) Filtered Interferogram (c) Thinned Image (d) Superimposed Thinned Image for Air when the cavity is half filled with water for $Ra_{air}=3,699$ and $Ra_{water}=22,350$	54
4.28	Infinite Fringe setting (a) without and (b) with Candle Flame	55
4.29	Evolution Patterns for water when the cavity is half filled with Water for $T_c=24^\circ\text{C}$ , $T_h=26^\circ\text{C}$ , $Ra_{air}=3,699$ and $Ra_{water}=22,350$	55
4.30	(a) Original Interferogram (b) Filtered Interferogram (c) Thinned Image (d) Superimposed Thinned Image for water when the cavity is half filled with water for $Ra_{air}=3,699$ and $Ra_{water}=22,350$	56
4.31	Roll patterns in air and water phase for $Ra_{air}=3,699$ and $Ra_{water}=22,350$	57

B.1	Numerically generated (a) Velocity Vectors, (b) Streamlines, (c) Isovorticities, and (d) Isotherms for $Ra=34,200$ , $Pr=0.7$ , $Ma=0$ , $Bi=10.0$ for a Closed cavity	71
B.2	Numerically generated (a) Velocity Vectors, (b) Streamlines, (c) Isovorticities and (d) Isothermsfor $Ra=34,200$ , $Pr=0.7$ , $Ma=0$ , $Bi=10.0$ for an Open cavity	72
B.3	Numerically generated (a) Velocity Vectors, (b) Streamlines, (c) Isovorticities and (d) Isothermsfor $Ra=34,200$ , $Pr=0.7$ , $Ma=1.0$ , $Bi=10.0$ for an Open cavity with Surface-Tension	73
B.4	Temperature Profiles at 3 columns in (a) Closed cavity (b) Open cavity without and (c) with Surface-Tension at $x=0.25, 0.50, 0.75$ for $Ra=34,200$ , $Pr=0.7$ , $Bi=10.0$	74
B.5	Numerically generated (a) Velocity Vectors, (b) Streamlines, (c) Isovorticities and (d) Isotherms for $Ra=10,000$ , $Pr=0.05$ , $Bi=10.0$ , $Ma=0.0$ for a Closed cavity	76
B.6	Numerically generated (a) Velocity Vectors, (b) Streamlines, (c) Isovorticities and (d) Isotherms for $Ra=10,000$ , $Pr=0.05$ , $Bi=10.0$ , $Ma=1.0$ for an Open cavity	77
B.7	Numerically generated (a) Velocity Vectors, (b) Streamlines, (c) Isovorticities and (d) Isotherms for $Ra=10,000$ , $Pr=0.05$ , $Bi=10.0$ $Ma=1.0$ for an Open cavity with Surface-Tension	78
B.8	Temperature Profiles at 3 columns in (a) Closed cavity (b) Open cavity without and (c) with Surface-Tension at $x=0.25, 0.50, 0.75$ for $Ra=10,000$ , $Pr=0.05$ , $Bi=10.0$	79
B.9	Effect of (a) Constant Surface-Tension (b) Non-Constant Surface-Tension on the displacement of the free surface owing to convection in Water, $Ra=34,200$ , $Pr=7.0$ , $Bi=10.0$ , $Ma=1.0$	81
B.10	Effect of (a) Constant Surface-Tension (b) Non-Constant Surface-Tension on the displacement of the free surface owing to convection in a liquid metal, $Ra=10,000$ , $Pr=0.05$ , $Bi=10.0$ , $Ma=1.0$	82



# Nomenclature

$g$	Accelaration due to gravity,m/s <sup>2</sup>
$h$	Height of the cavity,m
$L$	Distance traversed by the laser beam through the test cell,m
$n$	Refractive index of the fluid
$n_o$	Reference value of refractive index
Nu	Nusselt number (line-of-sight and surface averaged)
Pr	Prandtl number of the fluid, $(\nu/\alpha)$
Ra	Rayleigh number
Bi	Biot number
Ma	Marangoni number
A	Aspect ratio
Gr	Grashoff number
$T$	Temperature,K
$T_o$	Reference temperature,K
$\Delta T_i$	Interface temperature,K
$\Delta T_e$	Temperature difference between successive fringes,K
$\alpha$	Thermal diffusivity of the fluid,m <sup>2</sup> /s
$\beta$	Coefficient of volume expansion of the fluid,K <sup>-1</sup>
$\lambda$	Wavelength of the laser,nm
$\nu$	Kinematic viscosity of the fluid,m <sup>2</sup> /s
$\rho$	Density of fluid,kg/m <sup>3</sup>
$\rho_o$	Reference value of density,kg/m <sup>3</sup>
$\sigma$	Surface-Tension,N/m
$\theta$	Non-dimensional temperature
$\psi$	Dimensionless stream function
$\omega$	Dimensionless vorticity

# Chapter 1

## Introduction

The heat transport processes augmented by fluid motion in a horizontal fluid layer confined between a pair of parallel plates heated from below and cooled from the above is often called Rayleigh-Benard Convection. Due to the temperature gradient imposed across the plates, the fluid layer near the lower wall expands and thereby becomes less dense than the overlying layers. This is a gravitationally unstable configuration. In order to achieve stability, the warmer lighter layer at the bottom will tend to rise and the cooler heavier layer at the top will tend to sink. This will result in a convective flow, leading to a cellular pattern of fluid motion.

### 1.1 Convection in Fluids

In Rayleigh-Benard convection a thin layer of the fluid is confined between two flat, rigid, horizontal plates. The fluid completely fills the space between the plates. In particular, there is no free surface formed. The fluid layer is heated from below and cooled from the top resulting in a convective motion. Buoyancy is the driving force responsible for the convective motion. If buoyancy force is smaller than a certain threshold, the viscous forces between the fluid layers acts as internal friction and inhibit fluid motion. Heat transfer across the fluid layer is then purely by conduction. Once buoyancy forces exceed the threshold value, convective motion starts.

The non-dimensional parameter Rayleigh number  $Ra$  is linked with buoyancy

and viscous forces in terms of energy as

$$\text{Ra} = \frac{\text{gravitational potential energy}}{\text{viscous dissipation}} = \frac{g\beta(T_{\text{hot}} - T_{\text{cold}})H^3}{\nu\alpha} \quad (1.1)$$

The Prandtl number is a second dimensionless quantity arising in thermal convection. It is a measure of ratio of the molecular diffusivity of momentum to that of thermal energy and is a fluid property. The Prandtl number is defined as

$$\text{Pr} = \frac{\text{molecular diffusivity of momentum}}{\text{molecular diffusivity of thermal energy}} = \frac{\nu}{\alpha} \quad (1.2)$$

Flow transitions are generally described in terms of Rayleigh number and Prandtl number.

Two-layer convection studied in the present work comprises of differentially heated superposed fluid layers. The layers are confined between two solid, horizontal isothermal surfaces heated from below and cooled from top. It is a transport problem that is affected by the ratios of thermo-physical properties such as  $\mu$ ,  $\rho$ ,  $\kappa$  of the two fluid layers and geometrical factors. The main difference between one and two-layer convection is in the formation of a free surface. This is possible with a liquid-gas combination which gives rise to surface-tension-driven convection apart from being buoyancy-driven. In superimposed immiscible liquids, two-layer convection gives rise to deformable interfaces. Interfacial surface-tension-gradient-driven convection is caused by the variation of surface tension with temperature. Like density, the surface tension decreases as temperature increases. Therefore the cooler region will tend to draw fluid particles towards itself in comparison to warmer region.

Marangoni number  $\text{Ma}$  is a non-dimensional parameter which links surface tension and viscous forces in terms of energy as

$$\text{Ma} = \frac{\text{surface tension energy}}{\text{viscous dissipation}} = \frac{\sigma_T \Delta T H}{\mu \kappa} \quad (1.3)$$

Convective motion can be initiated by surface tension alone, even in the absence of a gravity field.

Benard-Marangoni convection combines the effect of buoyancy and surface tension. This typically occurs in a liquid-gas system. Buoyancy is initiated in the upper gas layer, and simultaneously sends a thermal signature to the surface. This generates either surface tension or buoyancy convection in the lower layer.

Rayleigh-Benard-Marangoni convection is of interest in a variety of engineering applications and has a great scientific importance. It has direct relevance to atmospheric convection. The importance can be seen from geophysical studies to astronomical research. The need to study fluid convection is very strongly felt for theoretical as well as fundamental reasons.

The Rayleigh-Benard convection is an important mechanism of fluid flow and heat transfer in natural as well as many engineering systems. Important applications of two-layer convection are:

1. convection in the earth's mantle.
2. liquid-encapsulated crystal growth.
3. development of new generation boilers.
4. weather prediction programme.
5. glass processing in low gravity conditions.

## **1.2 Literature Review based on the Two Layer Convection**

Literature for two layer convection can be categorized into:

1. Analytical studies
2. Numerical studies
3. Experimental studies

Convection in these studies could be dominated by buoyancy alone, surface tension alone or a combination of both.

### **1.2.1 Analytical studies**

Zeren and Reynolds (1972) predicted that the instability response is dependent on the properties of the fluids. Instability also varies with the total depth of layer and depth fraction of one fluid.

Through a mathematical model Busse (1989) has investigated the onset of convection in two layers. The two superimposed immiscible fluids with combinations of ethylene glycol-oil and ethylene glycol-decane were heated from below. He showed that the convection in two layers may occur in the form of either viscous or thermally coupled motions. He concluded that oscillatory instability exists and corresponds to a cyclic variation between above motions. Narayanan (1996) has determined the pattern formation at the bifurcation point from the quiescent state. The critical conditions which determine the critical Marangoni number  $Ma$  for different aspect ratios were found. The patterns for the onset of three-dimensional convection in a bounded circular container were theoretically obtained. Golovin (1997) presented a theory of secondary instabilities in silicone-oil system with a deformable interface. He concluded that this instability is seen to be either monotonic or oscillatory.

### 1.2.2 Numerical studies

Busse (1996) has analyzed the complex interaction between rolls of different orientations. The stability of undulating roll states and their modulations in the two-layer system were also analyzed. He concluded that through controlled initial conditions rolls with wavelength in the zigzag unstable regime can be generated.

Johnson and Narayanan (1997) concluded that if depths of fluids layers are approximately equal, then the respective convective fields can have two couplings: viscous (or mechanical) or thermally. In viscous coupling, the convection rolls rotate in the opposite direction while in thermal coupling, they rotate in the same direction. Dijkstra (1992) studied the problem of pattern selection in small aspect ratio containers. Because of limited computational resources, he restricted the work to two-dimensional containers. He concluded that no-slip sidewalls greatly influence the multiplicity of the stable steady patterns. Nield (1964) has combined the two rival theories of buoyancy-driven and surface tension-driven convection. He showed that the two theories causing instability reinforce each other and are tightly coupled. The corresponding cells formed are of same size. Dauby *et al.* (1997) presented a study of Benard-Marangoni instability in small rigid container. They determined the critical conditions for onset of motion as well as the convection patterns at the threshold.

### 1.2.3 Experimental studies

Andereck *et al.* (1996) have presented preliminary results from their experiments in a system consisting of two immiscible fluid layers in a rectangular geometry, driven by a vertical temperature gradient. Time-dependent variations in the type of coupling observed between layers have been characterized and described. Prakash and Koster (1996) have studied the two-dimensional convection in a two layer system the with real-time holographic interferometry. They concluded that thermal and mechanical coupling mechanisms are both possible between the layers. Johnson and Narayanan (1996) studied the appearance of the codimension-two point in a silicone-oil-air combination placed between conductive plates. The upper plate consisted of zinc selenide, which is transparent to infrared radiation. The flow visualization technique used an infra-red IR camera as the sensor. It was placed above the apparatus and viewed down upon the surface to catch the flow patterns at the interface.

Schatz *et al.* (1999) recently investigated the transition between hexagonal and square patterns. It occurred as the heating is increased in a fluid of Prandtl number 81. The flow visualization technique used in the silicone-air system was Shadowgraph. Busse (1996) has discussed two-layer convection from experimental as well as theoretical point of view. He presented the results from an experiment with two-fluid layer in an annular channel with 1:2 ratio of layer heights.

Johnson, Narayanan, and Dauby(1999) in their experimental studies have presented the effect of air height on the pattern formation in liquid-air bilayer convection. For visualizing the flow patterns in the silicone oil-air combination in the test cell an inframetric camera was used. The camera was directly placed above the test- section. The camera measured the infrared radiation being emitted by the silicone oil and thus helped in finding the temperature distribution at the interface.

## 1.3 Objectives of the present study

The present study is concerned with Rayleigh-Benard convection in superposed fluid layers of air and water. The cavity is rectangular in plan and square in cross-section. The length of the cavity is 447 mm and the height is 32.1 mm.

Five different experiments are done. In these experiments, the cavity temperature difference was kept constant at  $\Delta T=10^{\circ}\text{C}$ . The values of Rayleigh numbers have been calculated by using Equation 1.1 and the fluid properties have been evaluated at the average cavity temperature in all the experiments conducted.

The present work is directed towards achieving the following objectives:

1. The influence of Rayleigh number on the steady state thermal field.
2. The transient evolution of the thermal field at a given Rayleigh number.
3. Temperature distribution at the interface.
4. Heat flux at the solid walls.
5. Shape of the interface.

It is proposed to study buoyancy-driven convection in superposed layers of air and water using laser-interferometry. The fluid layers are taken to be enclosed in a cavity. The interferograms have been obtained as a collection of fringe patterns. The interferograms give line-averaged information along the direction of the light ray. The interferograms can be used to identify the flow pattern prevailing within the cavity.

## Chapter 2

# Apparatus and Instrumentation

A Rayleigh-Benard experimental setup is apparently simple in design. It comprises of two horizontal surfaces of high thermal conductivity which are maintained at different constant temperatures. The vertical side walls are perfect insulators. Though simple in design, various factors are taken into account during the fabrication of the test cell and also while performing the experiments. For example, uniformity and constancy of surface temperatures, parallelism of the walls defining the fluid layer, parallelism of the optical windows and properties of the insulating surfaces are all factors that determine the quality of the experiments. Further, some extraneous factors such as building vibrations, air motion and changes in the ambient temperature strongly affect the recorded interferograms. Hence these experiments have to be performed with due care and precautions.

The apparatus used to study the convection phenomenon in the horizontal layer of fluid is shown schematically in Figure 2.1. The test cell consists of three sections namely the top tank, the test section and the bottom tank. The effective length of the fluid layer is 447 mm. The fluid layer is confined by two aluminium plates of thickness 3 mm above and below. The two longer sides are confined by insulated walls and the other two square sides by optical windows. The hot and the cold surfaces were maintained at uniform temperatures by circulating water over them. To reduce edge effects, the heat transfer areas of the two tanks were made quite large compared to the cavity.

For the designing of the test cell for Rayleigh-Benard convection the important steps taken are as follows: Firstly air and water were selected.



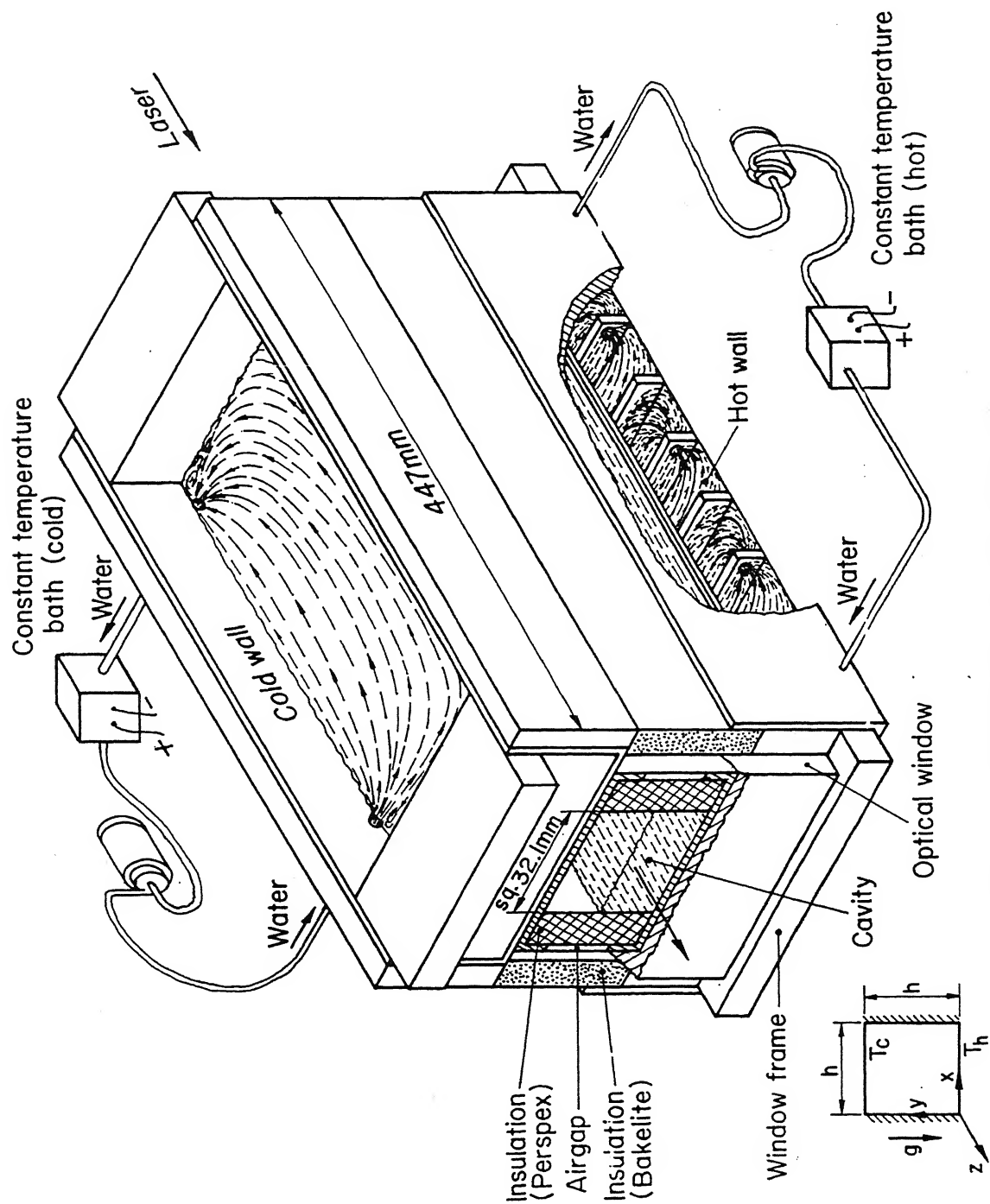


Figure 2.1: Schematic of the Test Cell

The selection was based on the transparency of two fluids for studying bi-layer convection using laser interferometry. The thermophysical properties of fluids were selected in a specific temperature range that meets the experimental requirement.

The law of conservation of energy holds here while dealing with heat transport in fluids. Thus heat conducted to water from the lower wall is to be equal to heat convected to air which in turn is conducted to the top wall. With this approach, the interface temperature is calculated using the Nusselt number correlation given by Hollands *et al.* (1975). The correlation for air is

$$Nu = 1 + 1.44\left[1 - \frac{1708}{Ra}\right] + \left[\left(\frac{Ra}{5830}\right)^{1/3} - 1\right] \quad (2.1)$$

For water, the correlation is given by:

$$Nu = 1 + 1.44\left[1 - \frac{1708}{Ra}\right] + \left[\left(\frac{Ra}{5830}\right)^{1/3} - 1\right] + 2\frac{(Ra)^{1/3}}{140}\left[1 - \ln\frac{(Ra)^{1/3}}{140}\right] \quad (2.2)$$

After getting the interface temperature  $T_i$ , and layer heights  $H$ , the Rayleigh number for each of the fluids is evaluated for air and water by using Equation 1.1.

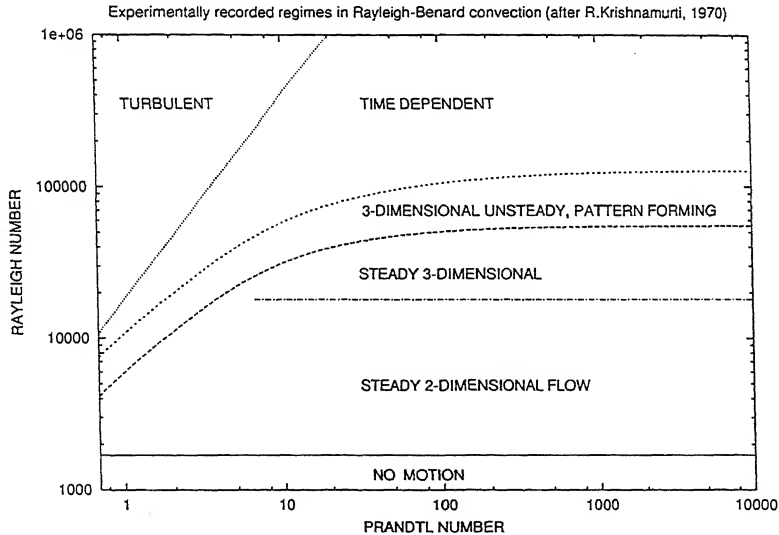


Figure 2.2: Various flow regimes in a horizontal fluid layer heated from below

The dimensions of the cavity which is square in cross-section, have been finalised on the basis of individual Rayleigh numbers. The length of the test cell was decided on the basis of aspect ratio  $A$ . To realize an infinitely long two-dimensional cavity aspect ratio should be high. The height of the cavity is decided

on the basis of beam diameter (70mm), size of the optical window (50mm) and the size of the rectangular tube commercially available.

The individual heights of air and water have been selected on the basis of expected nature of convective flows as per Krishnamurti's (1970) flow regime diagram, Figure 2.2. In the present study the respective air and water heights were used to get the steady two-dimensional convective flow in each layer.

After getting the dimensions of the cavity, the material is selected for the top and bottom walls. Aluminium owing to its high thermal conductivity was selected for the two walls. Aluminium provides isothermal conditions at the top and bottom walls. Thus perfectly conducting walls required for Rayleigh-Benard convection can be achieved. The thickness of the wall were selected by considering the two factors (a) minimum thickness for negligible temperature gradient and (b) sufficiently thick walls to support water tanks. Thus optimally 3 mm thick wall was selected for forming the cavity.

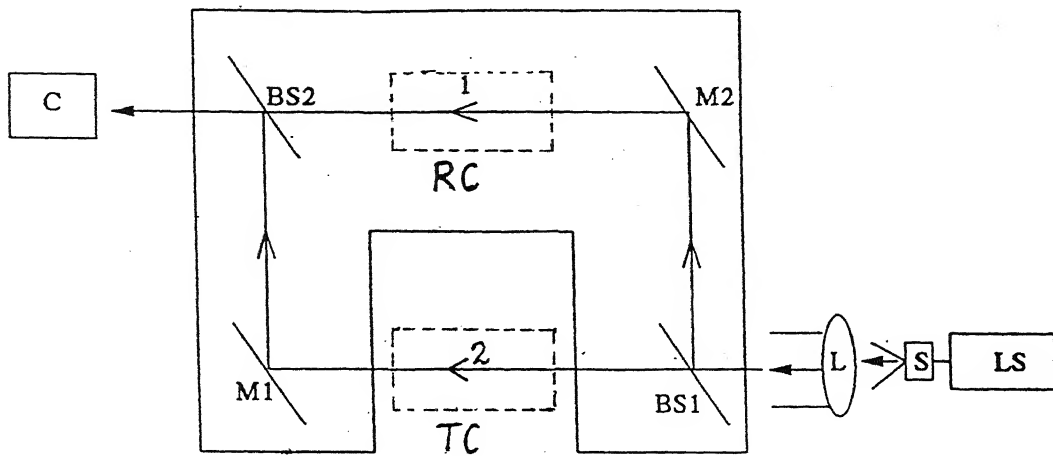
Now the spacer was chosen on the basis of two factors (a) providing accurate vertical spacing between two walls and (b) acts as an insulated side walls. Highly polished polyglass (perspex) with very low thermal conductivity was chosen to meet the above requirements.

For the visualization of flow the high grade optical windows of material Fused Silica of thickness 10 mm was selected for the front and back walls of the test cell. The term *high grade* refers to the excellent surface quality and parallelism of optical window surfaces.

## 2.1 Laser Interferometry

For the temperature measurement in the fluid medium, the primary instrument employed in the present work is the Mach-Zehnder interferometer. Figure 2.3 is a schematic diagram of the Mach-Zehnder interferometer.

The optical components of the interferometer are the beam splitters BS1 and BS2, mirrors M1 and M2. These components are oriented at  $45^\circ$  angle with respect to the laser beam direction. The first beam-splitter BS1 splits the incoming collimated beam into two equal parts, the transmitted and the reflected beams. The transmitted beam is the test beam whereas the reflected one is the reference



M	Mirror	L	Convex lens	1	Reference beam
BS	Beam splitter	LS	Laser source	2	Test beam
C	CCD camera	S	Spatial filter		

Figure 2.3: Schematic Drawing of the Mach-Zehnder Interferometer

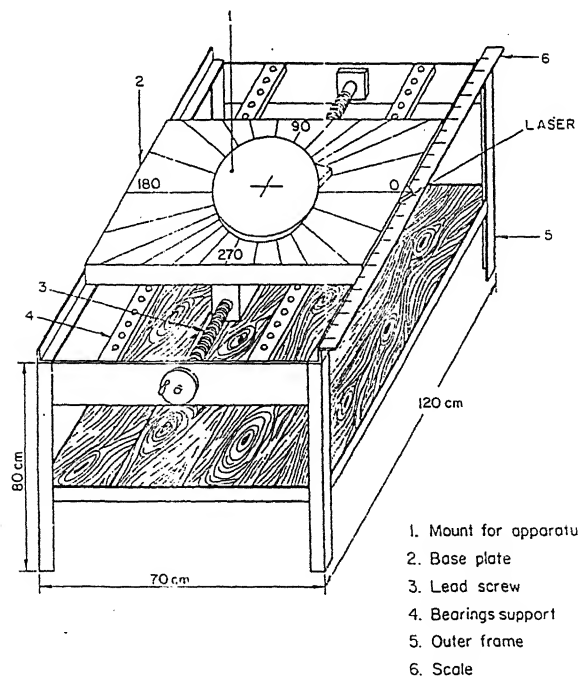


Figure 2.4: Schematic Drawing of the Traversing mechanism

beam. The test beam passes through the experimental apparatus where the convection process is in progress. This test beam is reflected by mirror M1 and recombines with the reference beam on the plane of second beam splitter BS2. The reference beam undergoes a reflection at M2 and passes through the reference medium and is superimposed with the test beam at BS2.

Due to superposition of the test and the reference beams, an interference pattern is produced at BS2. This pattern contains the information of the variation of the refractive index in the test region. For measurements in liquid a compensation chamber is required to introduce an appropriate reference environment.

The mirrors and beam splitters used in this configuration are of 150 mm diameter. Beam splitter has 50% reflectivity and 50% transmittivity. The mirrors are coated with 99.9% pure silver and employ a silicon dioxide layer as a protective layer against oxidation.

The Mach-Zehnder interferometer can be operated in two modes; namely (a) Infinite fringe setting and (b) Wedge fringe setting. In (a) the test and reference beams are set to have zero path difference in the absence of any thermal disturbance and fringes form due to density and temperature changes alone. Since each fringe is a line of constant phase, it is also a line of constant refractive index, a line of constant density and temperature and hence an isotherm. The infinite fringe setting is employed for high accuracy temperature measurements in the fluid. In (b), the mirrors and beam splitters are deliberately misaligned to produce an initial fringe pattern of straight lines. When a thermal disturbance is introduced in the path of the test beam, these lines deform and represent temperature profiles in the fluid. In general for the measurement of wall heat flux the wedge fringe setting is preferred.

A 35 mW, continuous wave He-Ne laser ( $\lambda=632.8$  nm) is employed as the coherent light source for the interferometer. The original laser beam is of the diameter 2 mm. A spatial filter is used here to expand the beam to 70 mm diameter and a planoconvex lens is used to collimate the beam.

A CCD (Charge Coupled Device) camera of spatial resolution of  $512 \times 512$  pixels has been used to capture the interferograms. This camera is connected to a PC-based image processing system through an 8-bit A/D card. The fringe pattern is stored in the form of a matrix of integers, with intensities varying between 0 and 255, where 0 indicates black and white is 255. In the frame

grabber used, the image acquisition is at the rate of 50 images per second.

The thermocouples which are used to monitor the temperature of the two horizontal aluminium surfaces of the cavity and the ambient temperature were connected to a 30 channel recorder. The temperature of the plates were monitored throughout the experiment. In the experiments 5 K-type thermocouples are used.

The optical components of the interferometer are extremely sensitive to vibrations. To avoid ground vibration from reaching the optics, the entire interferometer is placed over four pneumatic isolation mounts. These mounts are connected to an air compressor for pressurization. Once the mounts are pressurized the entire interferometer floats over the mounts. The operating pressure for the mounts is  $5 \text{ kg/cm}^2$ . This stabilizes the interferometric images and facilitates image acquisition.

A traversing mechanism is needed to mount the apparatus in which the desired experiment is in progress. This enables translation and rotation of the test cell with respect to the fixed positions of the laser source and the optics. The traversing mechanism is schematically shown in Figure 2.4. The base of the traversing mechanism is padded with a rubber sheet of 30 mm thickness to damp any external vibration from reaching the test cell.

## 2.2 Alignment of the Interferometer

Before the start of the experiment the interferometer has to be aligned. All the experiments in the present work are performed with the infinite fringe setting mode of the interferometer. Adjustment of the infinite fringe setting is delicate and requires efforts. The initial field of view is one of complete brightness since the interference is constructive. The geometrical and the optical path lengths of the test and reference beams are same in the absence of any thermal disturbance in the path of the test beam. As the interferometer approaches the infinite fringe setting the distance between the fringes increases and the number of fringes decreases.

Figure 2.5 shows the infinite fringe setting mode of the interferometer.

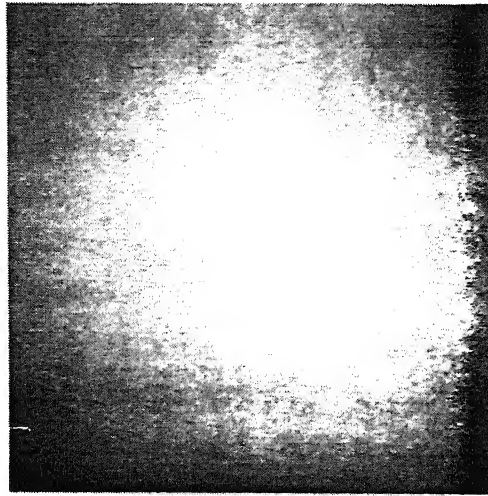


Figure 2.5: Infinite Fringe Setting of the Interferometer

## 2.3 Experimental Procedure

Firstly the pneumatic isolation mounts, on which the interferometer lies are pressurized. This ensures that the floor vibrations and other external disturbances do not disturb the initial setting. Before the start of the experiments, the Mach-Zehnder interferometer is set in the infinite fringe setting mode.

Isothermal conditions on the lower and upper plates of the test cell are ensured by circulating a large volume of water in the lower and upper tank. Temperature measurements are made at regular intervals of time during the experiments. Total experimental run time of around one and half hours enables the plates to acquire a constant and uniform temperature through out their surfaces and hence leading to isothermal conditions.

The interferograms have been recorded at regular intervals of time in order to show the transients that the fluid undergoes before reaching the steady state. At steady state, three to four interferograms have been recorded in a gap of 10 minutes to ensure that the steady state condition prevails in the cavity. In all the experiments the position of the CCD camera is fixed. The lights of the room

are switched-off at the time of recording of the interferograms.

The complete view of the experimental setup with the accessories are shown in Figure 2.6 and figure 2.7 shows the closer view of the test cell used to study the convection patterns of two phase fluid layer.

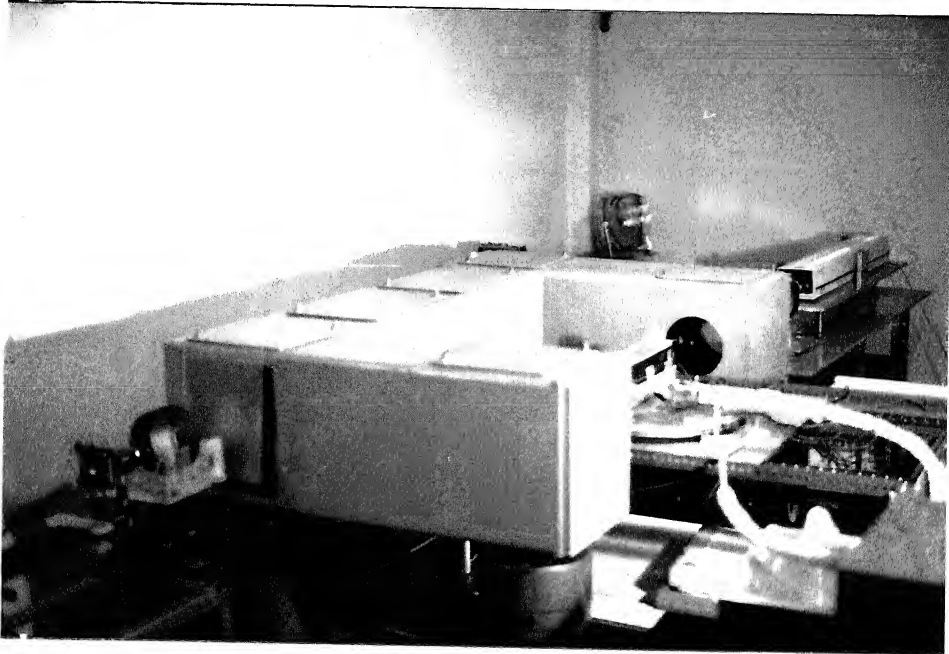


Figure 2.6: Complete View of the Experimental Setup

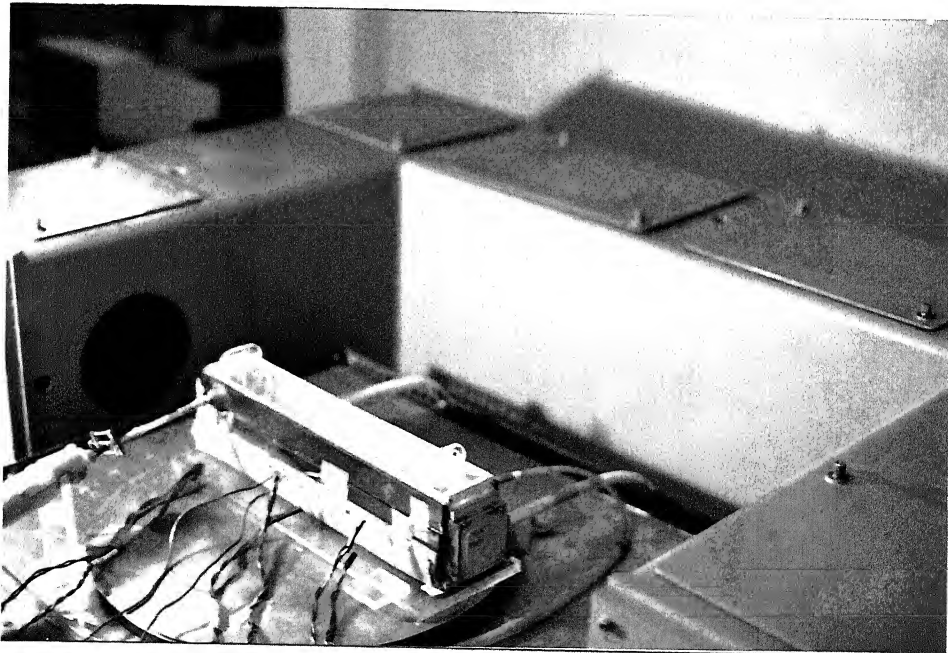


Figure 2.7: Closer View of the Test Cell



## 2.4 Uncertainty and Measurement errors

Errors in the experimental data are associated with misalignment of the apparatus with respect to the light beam, image processing operations including filtering, thinning and assigning temperature of fringes. Errors related to refraction effects in case of water is found to be high. All experiments were conducted several times to establish the repeatability of the fringe patterns. In the two phase problem, main error occurs during the experiment in air phase due to the dew formation on the optical windows. For all experiments except the one in which cavity is fully filled with water, the plate-averaged Nusselt number is found to be in good agreement with published correlations.

# Chapter 3

## Data Reduction

Optical techniques employed in fluid-flow measurements can be classified into three categories: (i) direct flow visualization by injecting some tracer particles (e.g., dyes, bubbles, solid particles), (ii) laser-Doppler systems where the frequency shift of scattered illumination from an injected tracer medium in the flow field is measured and (iii) measurement of index of refraction of the fluid or its spatial derivatives. Three popular methods that fall into the third category are:

1. **Shadowgraph Technique:** Here the reduction in light intensity or beam divergence is employed. It measures the variation of the second order derivative of the index of refraction normal to the light beam. The focus is on the reduction of light intensity as the beam diverges.
2. **Schlieren Technique:** Here the deflection of light in a variable refractive index field is captured. It handles the variation of first order derivative of the index of refraction normal to the light beam. Here the focus is on the reduction of light in a variable refractive index field is captured.
3. **Interferometric Technique:** Here the image formation is related to change in the refractive index with respect to a reference environment. It responds directly to the refractive index field of the flow system. Here the image formation is related to changes in the refractive index with respect to a reference environment.

This chapter discusses the principles of interferometry and procedures for the evaluation of the interferograms. The concepts of interferometry with reference to temperature field in the infinite fringe setting of Mach-Zehnder interferometer

have been discussed. Apart from these features this chapter also discusses the techniques used to improve the image quality and fringe thinning.

### 3.1 Interferometry

With the infinite fringe setting, the optical path difference between the test and the reference beam is zero in the absence of any thermal disturbance. Hence interference is constructive and a bright field of view is obtained. In practice, the image obtained is fringe-free but may show imperfection associated with the spatial filter and the interferometer optics. When nonisothermal conditions prevail in the path of the test beam (example, a candle flame) each ray of light undergoes a change of phase, depending on the extent of change of the refractive index of the medium. Hence an optical path difference is established between the test and the reference beams, resulting in a fringe pattern.

As discussed, in interferometry, the image formation is related to the changes in the refractive index of the fluid with respect to the reference environment. Here attention is restricted to the image patterns that form in the infinite fringe setting. When isothermal conditions prevail in the test beam path each ray of light undergoes a change of phase, depending on the extent of change of the refractive index of the medium. Hence an optical path difference is established between the test and the reference beams, resulting in a fringe pattern. For temperature measurements, the refractive index variation has to be related to that of temperature. The relationship between the refractive index  $n$  and density  $\rho$  is

$$\frac{n^2 - 1}{\rho(n^2 + 2)} = \text{constant} \quad (3.1)$$

holds for transparent media. For gases, the refractive index is close to unity and the expression reduces to

$$\frac{n - 1}{\rho} = \text{constant} \quad (3.2)$$

where  $\rho$  is the density of the fluid. This relationship is called the Gladstone-Dale equation (Goldstein, 1983). It follows that  $dn/d\rho = \text{constant}$ . Now for moderate changes in temperature, density varies linearly with temperature as

$$\rho = \rho_o(1 - \beta(T - T_o)) \quad (3.3)$$

Hence  $dn/dT$  is also a constant. This implies that changes in temperature simultaneously result in changes in refractive index and this leads to changes in the phase of the wave. This is the origin of fringe formation in interferometry.

Let  $n(r, z)$  and  $T(r, z)$  be the refractive index and temperature field respectively in the test region. Let  $n_o$  and  $T_o$  be the reference values of  $n$  and  $T$  respectively as encountered by the reference beam. Let  $L$  be the geometrical path length covered by the test and reference beams. Now for the test beam, the optical length is defined as

$$PL = \int_0^L n(r, z) ds \quad (3.4)$$

and for the reference beam,

$$PL = \int_0^L n_o ds \quad (3.5)$$

is the optical path length. The interferogram is a fringe pattern arising from the optical path difference

$$\Delta PL = \int_0^L (n(r, z) - n_o) ds \quad (3.6)$$

which in terms of temperature is

$$\Delta PL = \frac{dn}{dT} \int_0^L (T(r, z) - T_o) ds \quad (3.7)$$

The integral is evaluated along the path of a light ray given by the coordinate  $s$ . The fringes seen on the interferograms are locus of points having the same optical path difference. Hence on any given fringe the optical path difference  $\Delta PL$  is a constant and

$$\int_0^L (T(r, z) - T_o) ds = \frac{\Delta PL}{dn/dT} = \text{constant} \quad (3.8)$$

Hence

$$\int_0^L (T(r, z)) ds - T_o L = \text{constant} \quad (3.9)$$

The integral  $\int_0^L (T(r, z)) ds$  is defined as  $\bar{T}L$ , where  $\bar{T}$  is the average value of  $T(r, z)$  over the length  $L$  of the laser beam through the test cell. This is also the line integral of the function  $T(r, z)$ . Hence

$$L(\bar{T} - T_o) = \text{constant} \quad (3.10)$$

In the infinite fringe setting Equation 3.10 holds good for all the fringes. When  $L$  is constant for all the rays, Equation 3.10 implies that  $\bar{T}$  is a constant over the fringe and hence each fringe represents a locus of points over which the average of the temperature field along the direction of the ray is a constant, hence fringes are isotherms.

Defining the function  $L(\bar{T} - T_o)$  in Equation 3.10 as  $f(\bar{T}, L)$ , the fringe temperature on two successive fringes for same value of  $L$  can be given as:

$$\text{fringe 1 : } f_1(\bar{T}, L) = \frac{\Delta PL}{dn/dT} \quad (3.11)$$

$$\text{fringe 2 : } f_2(\bar{T}, L) = \frac{(\lambda + \Delta PL)}{dn/dT} \quad (3.12)$$

where  $\lambda$  is the wavelength of the laser used. From these two equations, the temperature drop per fringe shift,  $\Delta T_\epsilon$ , can be calculated as

$$\Delta T_\epsilon = \frac{1}{L}(f_2(\bar{T}, L) - f_1(\bar{T}, L)) = \frac{\lambda/L}{dn/dT}. \quad (3.13)$$

The number of fringes expected in a projection can be estimated directly from the relation

$$\text{Number of fringes} = \frac{T_{hot} - T_{cold}}{\Delta T_\epsilon} \quad (3.14)$$

This equality was seen to be satisfied in most of the experiments reported in the work.

## 3.2 Image Enhancement

The images of the fringe pattern collected using the CCD camera and the A/D card tend to be noisy. Noise can be defined as extraneous and unwanted intensity variation which is superimposed over the useful portion of the data. There are various factors that are responsible for the generation of noise in the recorded data. Examples are the imperfection of the optical components, noise in the CCD array and digitization process itself. The most dominant factor is speckle which is the major source of noise in the interferometric images. Speckle is a super-saturation of the diffraction patterns over the basic interference pattern. It arises from the imperfection of the optical surfaces. The presence of microscopic unevenness on the optical surfaces leads to diffraction. The diffracted rays

interfere and generate local fringe patterns and corrupt the global intensity distribution. Filtering is required to extract the original intensity information from the recorded interferogram which is then processed for contrast improvement.

The Fourier Filtering method has been used to extract the useful information from the recorded interferograms. Figure 3.1 shows the original interferogram as recorded from the interferometer.

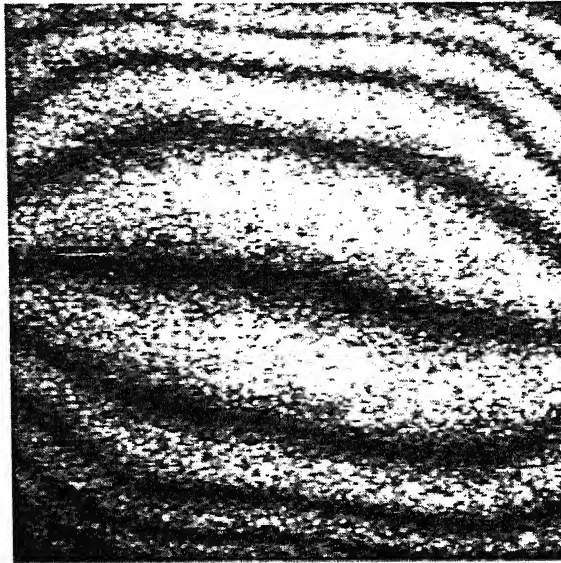


Figure 3.1: An Original Interferogram

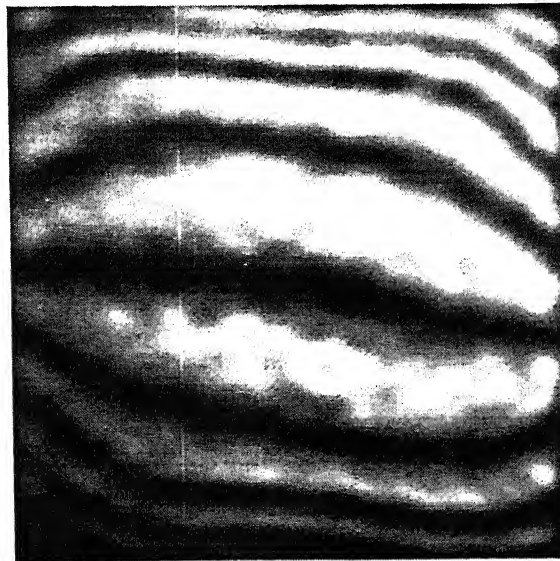


Figure 3.2: Filtered Interferogram

For Fourier filtering the image is first transformed to the wavenumber space with a two dimensional Fourier transform operation. The wavenumber is a kind

of a spatial frequency and is defined as the number of intensity cycles per pixel. Intuitively one can view the low wavenumber harmonics as information and high wavenumber harmonics as noise. Now in the wavenumber domain, a two-dimensional band pass filter can be used to effectively set the high wavenumber components to zero. An inverse Fourier transform restores the filtered image in the spatial domain. Figure 3.2 shows the filtered interferogram of the same image as shown in Figure 3.1.

The filtering removes the high wavenumber components of the intensity distribution and thereby removes the unwanted noise in the image data. At the same time, the image becomes blurred owing to the loss of contrast. Since the visual appearance of the original interferogram as recorded through the CCD camera is not good (as seen from Figure 3.1), the Fourier filtering operation further leads to the loss of the contrast. Hence there is a need for contrast improvement of the image that has to be analyzed. Different contrast improvement software packages are available through which one can enhance the quality of the image. Examples are GIMP and Electric Eyes available on the Linux platform. In the present work, Electric Eyes software has been used for this purpose. Figure 3.3 shows the contrast improved image of the same interferogram as shown in Figures 3.1 and 3.2. There is a definite improvement in the visual appearance of the image and the fringes are now more clearly visible.

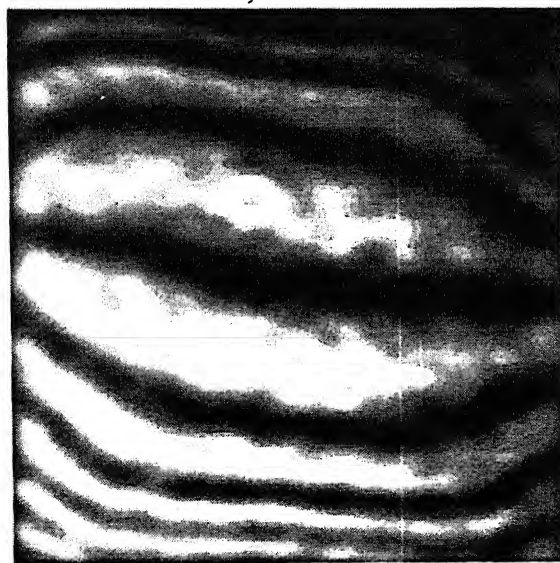


Figure 3.3: Contrast Improved Interferogram

There are three fringe thinning algorithms suitable for interferograms recorded

using the Mach-Zehnder interferometer. In the interferometric images, the fringes are represented by the alternate dark and bright bands. The quantitative information (temperature in the present work) is thus spread over the whole width of these bands that constitute the fringes. Hence fringe thinning is one of the most important operation in the extraction of quantitative information from the collected interferograms. It is the process of extraction of the set of points of minimum or maximum intensities in the dark and bright bands of the fringes. The minimum intensity corresponds to the points of complete destructive interference and hence will have a zero intensity. Similarly, a maximum intensity will appear at the points of constructive interference. In the present work, the fringe bands are reduced to fringe curves by locating the intensity minima in the dark fringe bands.



Figure 3.4: Superimposed Thinned Image with Original Image

In the present work, in order to reduce the fringe bands into fringe skeleton or curves the following approach has been adopted. This a free-hand drawing technique where the midpoints within a dark band of the interferogram are approximately located and joined by a smooth curve. It relies exclusively on eye judgment. The paint-brush utility of GIMP has been employed in this study. The image containing the fringe curves and the original image are subtracted to get the fringe skeleton. The superposition of the original interferogram and the fringe skeleton is shown in Figures 3.4 and 3.5. The paint-brush approach has the disadvantage of not locating the minimum intensity location, but does not



require code development and hence is reasonably fast.

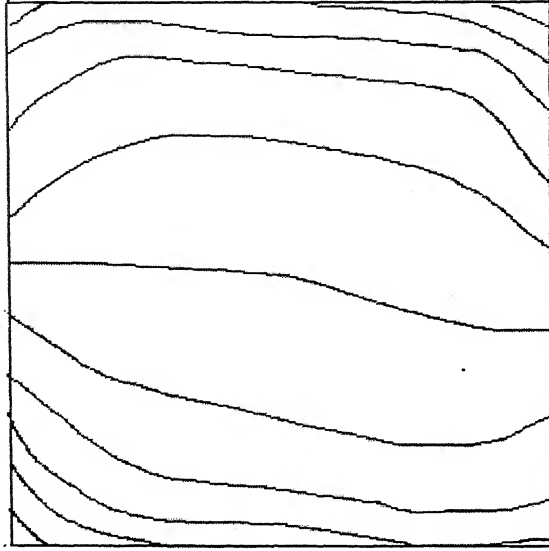


Figure 3.5: Thinned Image

### 3.3 Calculation of Fringe Temperatures

The calculation of temperature associated with the fringes is the most important step in interferometry. Figure 3.6 shows the schematic of a fringe skeleton after thinning. The upper and lower walls shown in the figure have known temperatures. Near the walls, a high temperature gradient results in a large number of thin fringes which are very closely spaced. Due to the finite resolution of the CCD camera, it may be possible that a few number of fringes near the walls could be lost during the recording of the interferograms. Hence the first fringe seen on the interferogram near the wall will be of some arbitrary order. Therefore one cannot assign a temperature to the fringes directly using the value of temperature difference per fringe shift  $\Delta T_c$  though the wall itself is an isotherm.

The interferogram is divided into two halves. The upper half is allotted temperature on the basis of upper wall temperature and the lower half on the

basis of lower wall temperature.

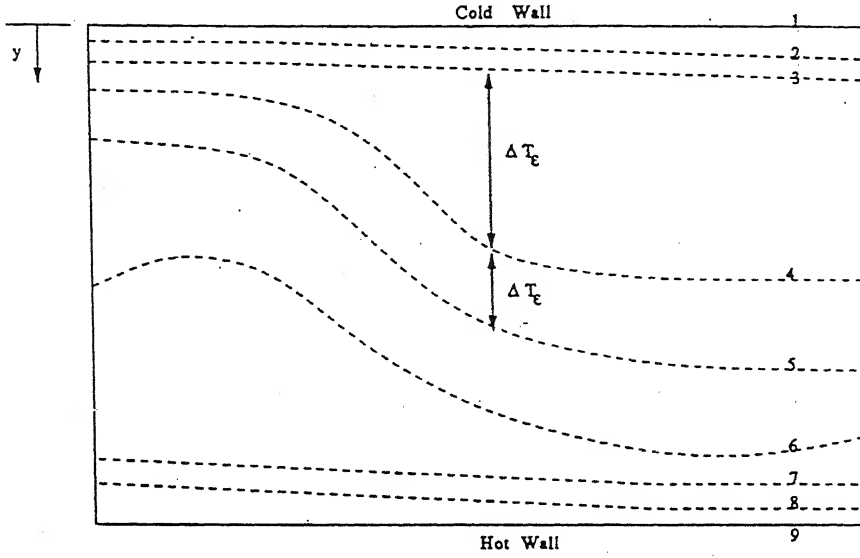


Figure 3.6: Schematic of an Idealized Fringe Skeleton for Temperature Calculations

Consider the fringes marked 2,3,4 in Figure 3.6. Fitting a function of type

$$T(y) = a + by + cy^2 \quad (3.15)$$

Where  $y$  is a vertical coordinate, we get

$$\Delta T_e = T_2 - T_3 = b(y_2 - y_3) + c(y_2^2 - y_3^2) \quad (3.16)$$

$$\Delta T_e = T_3 - T_4 = b(y_3 - y_4) + c(y_3^2 - y_4^2) \quad (3.17)$$

These two equations are solved for the constants  $b$  and  $c$ .

The local wall heat flux temperature is  $(\partial T / \partial y)_{y=y_1}$  and using Equation 3.15, this can be expressed as  $(b + 2cy_1)$ . Similarly, the gradient in temperature field at the first fringe is  $(b + 2cy_2)$ . Now the average of these two gradients is taken and is allotted as the wall temperature gradient. Finally, once this is known, the first fringe temperature near the top wall is calculated as

$$T_2 = (y_2 - y_1) \frac{(b + 2cy_1) + (b + 2cy_2)}{0.5} + T_1 \quad (3.18)$$

The subsequent fringe temperatures are found out by adding or subtracting the temperature gradient  $\Delta T_e$  to the temperature of the previous fringe when started from wall. In the present work, these temperature calculations were

carried along a particular column. The column was selected where the near wall fringes are dense.

### 3.4 Nusselt Number Calculations

Nusselt number calculations have been carried out to determine the heat transfer rates at the boundary walls of the cavity, Nusselt number is defined as

$$Nu = \frac{-h}{T_{hot} - T_{cold}} \frac{\partial T}{\partial y} \bigg|_{y=0,h} \quad (3.19)$$

In the present work average Nusselt number at the top and the bottom walls have been reported. The average Nusselt number for each of the plates has also been compared with the experimental correlation reported by Gebhart *et al.* (1968). For air, the correlation is given by:

$$Nu = 1 + 1.44 \left[ 1 - \frac{1708}{Ra} \right] + \left[ \left( \frac{Ra}{5830} \right)^{1/3} - 1 \right] \quad (3.20)$$

For water, the correlation is given by:

$$Nu = 1 + 1.44 \left[ 1 - \frac{1708}{Ra} \right] + \left[ \left( \frac{Ra}{5830} \right)^{1/3} - 1 \right] + 2 \frac{(Ra)^{1/3}}{140} \left[ 1 - \log \frac{(Ra)^{1/3}}{140} \right] \quad (3.21)$$

The Nusselt number calculations have been performed for all the cases and are compared with the reference value as given by the above mentioned correlations.

# Chapter 4

## Results and Discussion

Experiments performed in the present study are exploratory in nature. They have been conducted to examine various issues, such as, coupling between fluid motion in air and water, and interfacial effects. To this end, the temperature difference across the cavity has been maintained constant at a value of  $10^{\circ}\text{C}$ . Experiments have been performed in the following sequence:

1. Cavity filled with air,
2. Cavity filled with water,
3. Cavity half filled with water, with air above.

All experiments have been continued till steady state is reached. Interferograms during the transient as well as steady state have been recorded. A steady state calculation for the two layer problem that throws light on respective temperature drops in air and water is presented in Appendix A.

The present chapter discusses various qualitative and quantitative issues related to the evolution of the flow and thermal fields. Flow structures and roll pattern, transient evolution of the isotherms and the nature of the steady state have been reported. For all the experiments fringe temperature calculations, average Nusselt number at the top and the bottom walls and temperature variation over the height of the cavity have been presented in the following sections.

In order to examine the experimental results, a two dimensional numerical simulation has been carried out for flow and heat transfer in a square cavity. The parameters considered are (i)  $Ra=34,200$ ,  $Pr=0.7$  and  $Bi=10.0$  and (ii)  $Ra=10,000$ ,  $Pr=0.05$  and  $Bi=10.0$ . The governing equations, initial and boundary conditions

and the numerical technique used along with the results obtained have been discussed in Appendix B.

## 4.1 Convection in air

To study convection in air, it is not necessary to employ optical windows, particularly when the test cell is long in the direction of the light beam. Moreover, quartz windows exhibit a refractive index dependence on temperature, that is similar to air. Thus difference in the thermal field induced in the optical windows, between the test cell and the reference chamber can lead to additional fringes. There is also a possibility of a few fringes being lost. In case of liquids, one does not have the option of discarding the windows since the liquids has to be confined on all sides. The dependence of refractive index of liquids on temperature being very weak, in comparison to air as well as quartz, the possibility of distortion due to the presence of windows is minimized. In the present section, convection experiments in air with and without optical windows have been discussed.

The experiments in air without optical windows have been considered first. The top surface temperature is kept at 16°C and the bottom surface temperature at 26°C. Thus the temperature difference of 10°C is maintained across the cavity. This leads to a Rayleigh number of 34,200 in air. The transient evolution of the interferograms have been recorded at regular time intervals till the patterns become either repetitive or strictly steady in time.

Figure 4.1(a) and Figure 4.1(b) show the infinite fringe setting of the interferometer without and with a candle flame respectively. The candle flame test ensures that wedge fringes are not accidentally present in the field-of-view. Figure 4.2 shows the transient evolution of the thermal field till the steady state is reached.

The interferograms were collected in regular intervals of time as shown. The heat transfer process takes place between the fluid and the surfaces. Since the cavity is small, the time required for the temperature of the walls to become constant and the flow to reach steady state is also small. For early time, the wall temperatures had not stabilized and the corresponding fringe patterns have not been shown. With the passage of time, the number of fringes increases till steady state is reached.

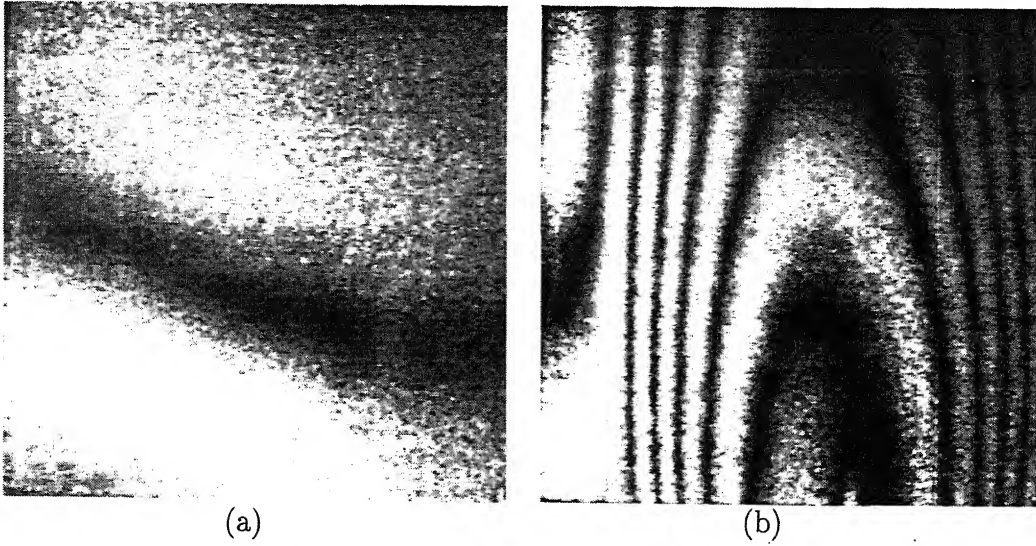


Figure 4.1: Infinite Fringe setting (a) without and (b) with Candle Flame

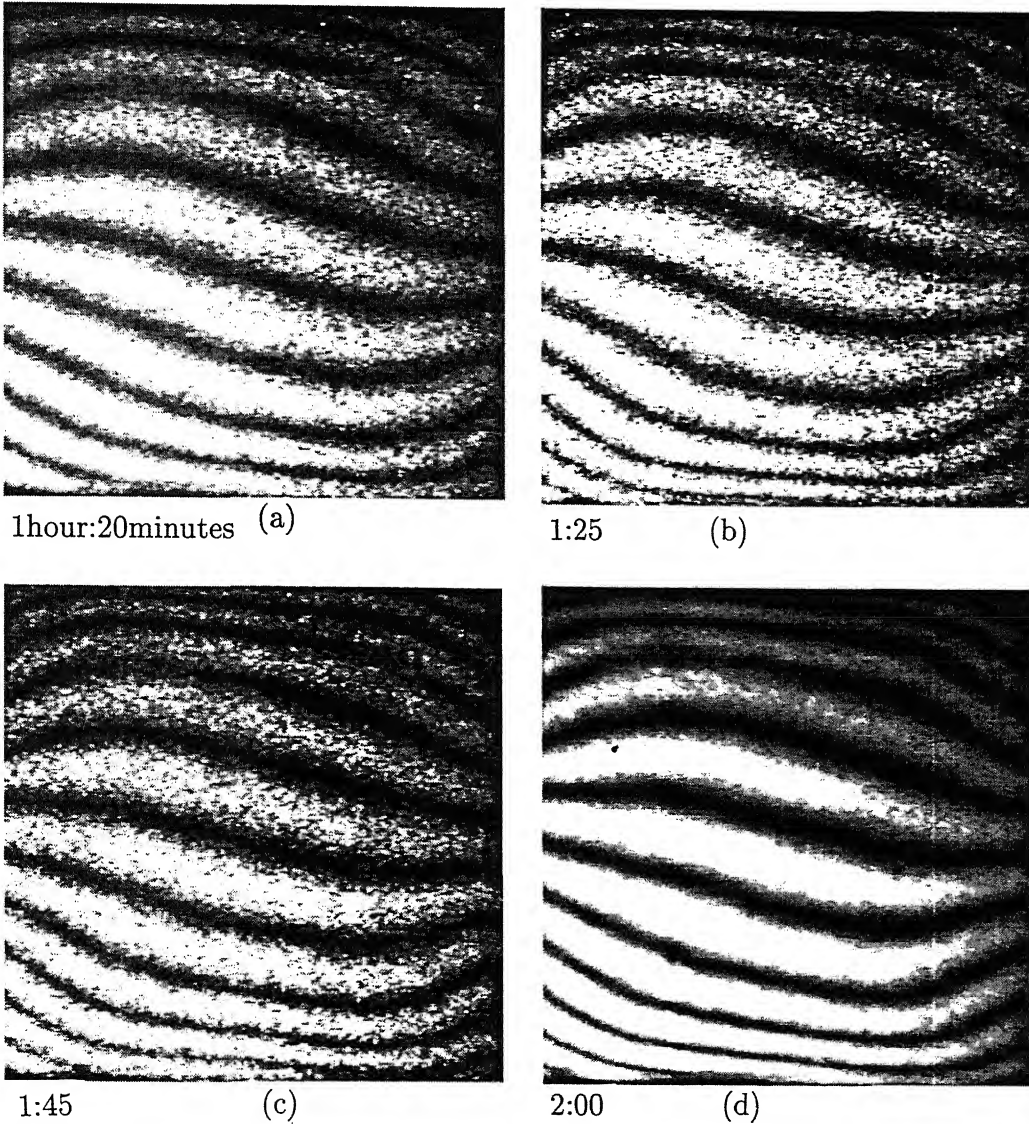


Figure 4.2: Evolution Patterns for Air without Windows for  $T_c=16^\circ\text{C}$ ,  $T_h=26^\circ\text{C}$  and  $Ra=34,200$

The spacing among the fringes near the wall are seen to be small compared to the mid-plane of the cavity. The spacing gradually increases towards the fringe edges. Since each fringe is an isotherm, a small fringe spacing gives rise to a large local heat flux. The largest local heat flux at the cavity walls at steady state occurs around the mid-plane of the cavity. The fluid accelerates on one side of the mid-plane, reaches a maximum at this point and decelerates to small values on the other side of the cavity, as it approaches the side walls. The overall flow pattern in the cavity is hence unicellular.

From Figures 4.2(a-d) it is clear that the isotherm spacings near the top and bottom walls of the cavity are less than the spacing in the central region of the test section. This is due to the reason that near the boundaries diffusive heat transfer rates are higher. In the central region of the test section, the conduction heat transfer is practically absent and the dominant mode is convection.

In the present experiment in a cavity with a square cross-section, the transient evolution of the thermal field took place over a substantially smaller time scale (for about one and a half hour) as compared to cavity square in plan and an axisymmetric cavity. Mishra *et al.*(1998) have reported a time scale of 4-5 hours in their experiments. Once the flow field has fully evolved, the fringe patterns were observed to be quite steady without any sideways movements of the fringes. This sideways movement of fringes was observed for higher Rayleigh numbers. Figure 4.2(b), Figure 4.2(c) and Figure 4.2(d) show the truly steady state nature of the flow field. These interferograms were recorded after one and half hours of the experimental run time to ensure the steady state behavior of the convection pattern. The number of fringes in the present experiment are more than that estimated by the formula  $N = (T_h - T_c)/\Delta T_e$ . Some false fringes are captured in the central region of the cavity where the temperature gradients are small.

Figure 4.3(a) and Figure 4.3(b) show the original steady state image and the Fourier filtered image respectively. Figure 4.3(c) shows thinned image and Figure 4.3(d) shows superimposed thinned image. From the thinned image, the calculations for the temperature of the fringes and the local Nusselt number can be performed. Figure 4.3(c) shows that the fringe thinning algorithm has been successful in the present work.

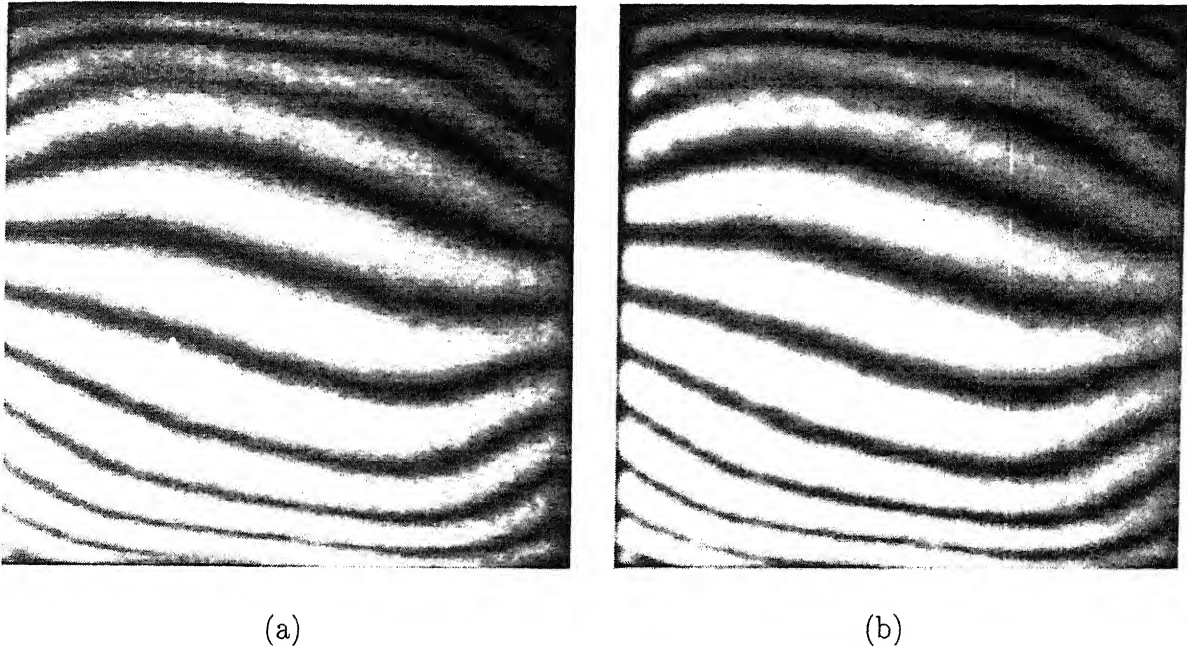


Figure 4.3: (a) Original Interferogram (b) Filtered Interferogram

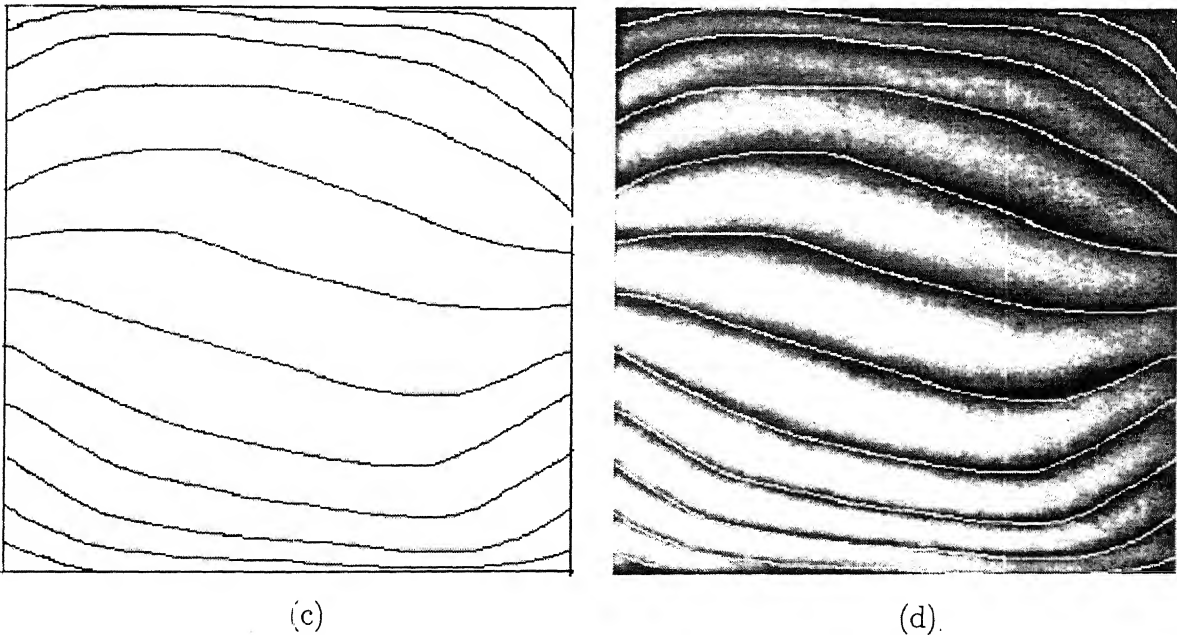


Figure 4.3: (c) Thinned Image (d) Superimposed Thinned Image  
for Air when the cavity is filled with Air for  $Ra=34,200$



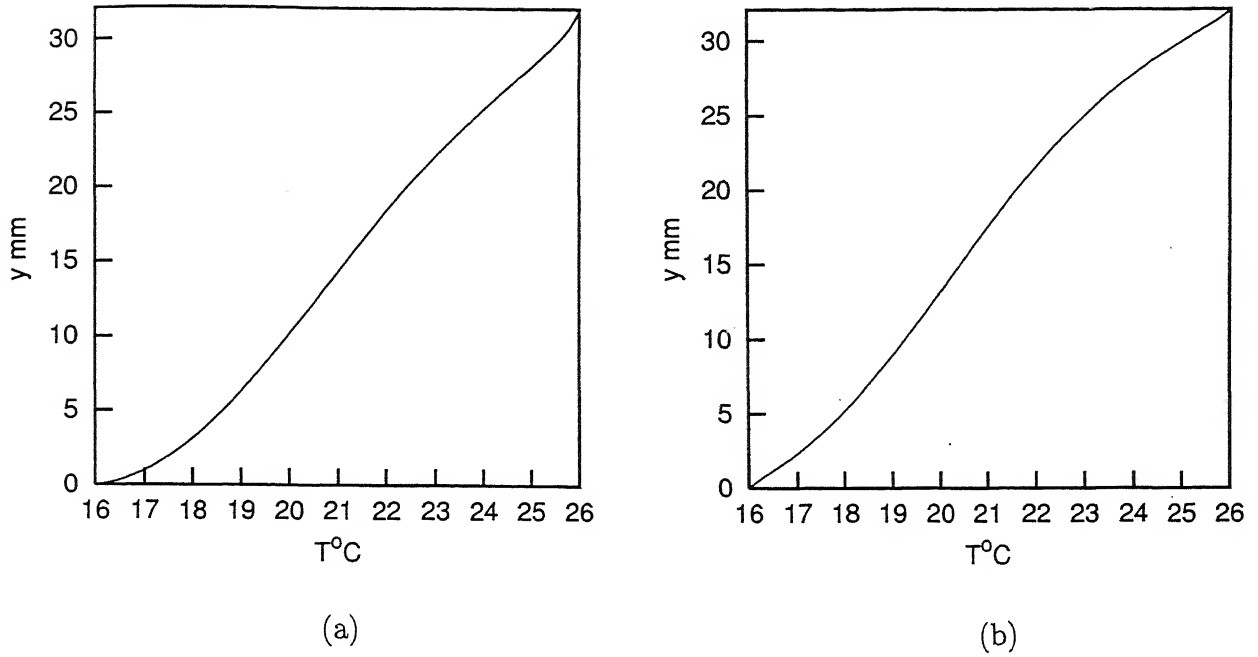


Figure 4.4: Temperature Profiles in air filled cavity for  $Ra=34,200$   
at (a)  $x=1.07$  mm and (b)  $x=21.4$  mm

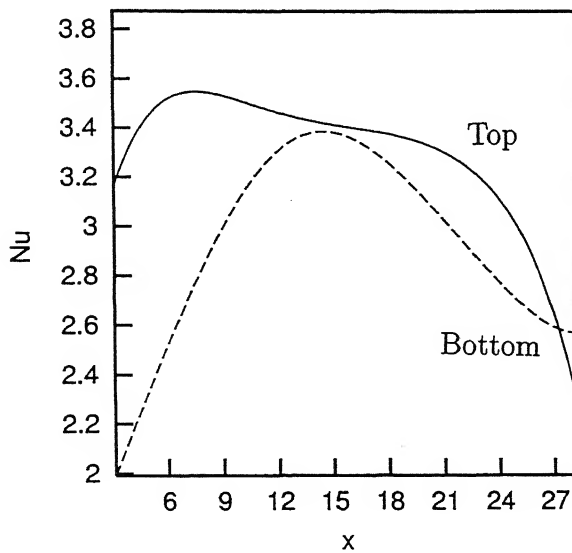


Figure 4.5: Local Nusselt number variation at the top and bottom walls

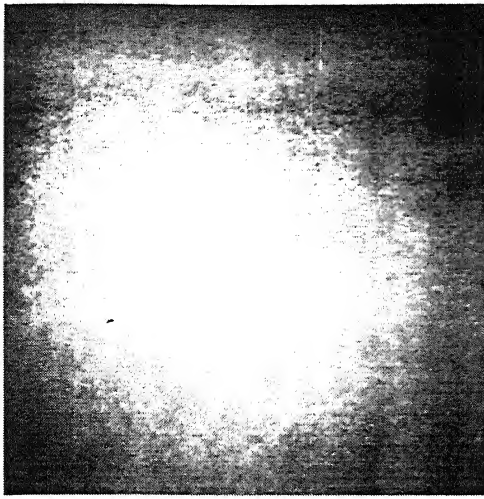
At steady state, the variation of the temperature field is plotted as a function of the vertical distance as shown in Figure 4.4 for two equally spaced columns along the width of the cavity.

Heat transfer rates at the boundary walls in terms of the local Nusselt number can be calculated by using Equation 3.19 as

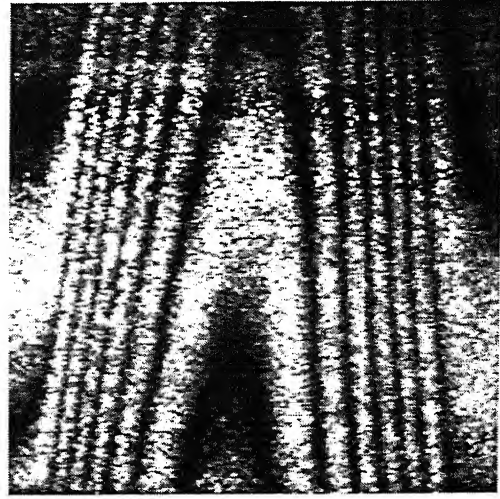
$$\text{Nu} = \frac{-h}{T_{hot} - T_{cold}} \frac{\partial T}{\partial y} \bigg|_{y=0,h}$$

Figure 4.5 shows the variation of local Nusselt number at the top and bottom walls of the cavity. The individual plate-averaged Nusselt numbers for the case of air without windows are 3.18 and 3.12 at the cold and the hot surfaces respectively of the cavity. The average Nusselt number for each of the plates has also been compared with the experimental correlation given by Gebhart *et al.* (1988), Equation 3.20. The value of average Nusselt number as calculated from Equation 3.20 is 3.17 for this case. The comparison between the present experiments and the published correlation is thus seen to be quite good.

Analysis of the flow field observed in air in the presence of optical windows is now presented. The experimental conditions are identical to the previous case, namely,  $T_c=16^\circ\text{C}$ ,  $T_h=26^\circ\text{C}$ ,  $\Delta T=10^\circ\text{C}$  and  $\text{Ra}=34,200$ . The cavity is enclosed by optical windows. Air is thus confined on all sides and contact with the outside atmosphere is prevented. The transient evolution of the flow field has been recorded at regular time intervals till the steady state is reached. Here the number of fringes is lower than in the experiments without optical windows. However the number of fringes match the estimate based on  $\Delta T_c$ . The fringe patterns are qualitatively similar to those without windows. The number of fringes were found to be 7 at steady state.



(a)

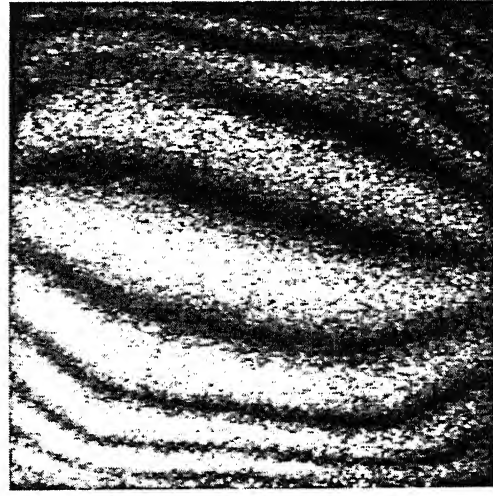


(b)

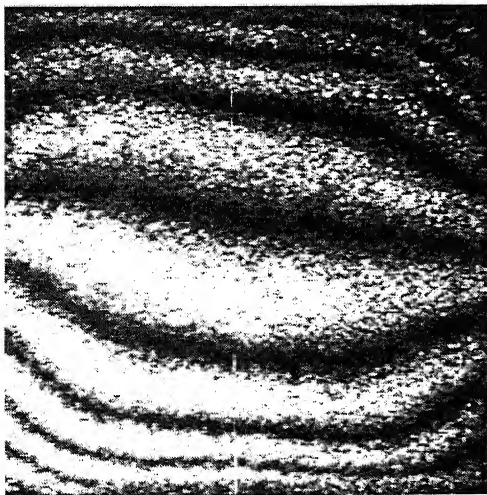
Figure 4.6: Infinite Fringe setting (a) without and (b) with Candle Flame



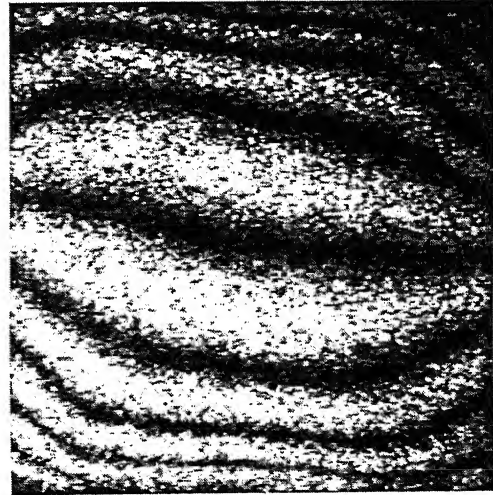
1hour:20minutes (a)



1:25 (b)



1:45 (c)



2:00 (d)

Figure 4.7: Evolution Patterns for Air with Optical Windows for  $T_c=16^\circ\text{C}$ ,  $T_h=26^\circ\text{C}$  and  $Ra=34\ 200$

Figure 4.6 shows the infinite fringe setting without and with a candle flame in the presence of optical windows. Figure 4.7 shows the transient evolution of the thermal field till the steady state is reached. The interferograms were collected in regular intervals of time as shown. The presence of windows did not alter the time required to reach steady state. With the passage of time, the number of fringes increased till the steady state was reached.

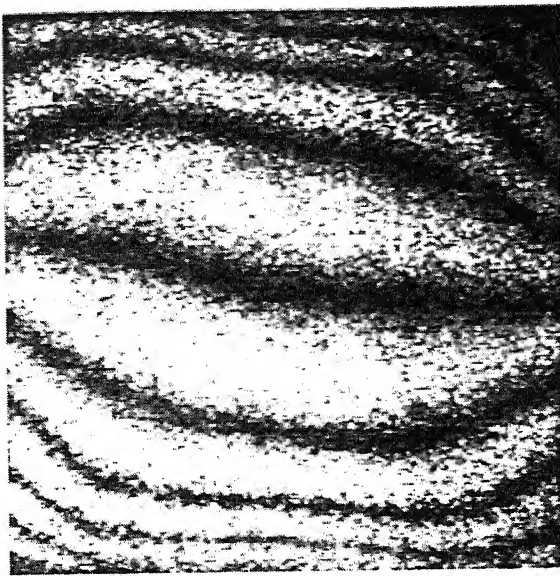
Once the flow field was fully evolved, the fringe patterns were observed to be quite steady and motionless. Figure 4.7(b), Figure 4.7(c) and Figure 4.7(d) show the steady state nature of the flow field. These interferograms were recorded after one and half hours of the experimental run time to ensure the steady state behavior of the convection pattern.

Figure 4.8(a) and Figure 4.8(b) show the original steady state image along with the Fourier filtered image respectively. Figure 4.8(c) shows thinned image and Figure 4.8(d) shows superimposed thinned image for air in the presence of optical windows. From the thinned image, calculation for temperature of fringes and the local Nusselt number can be carried out.

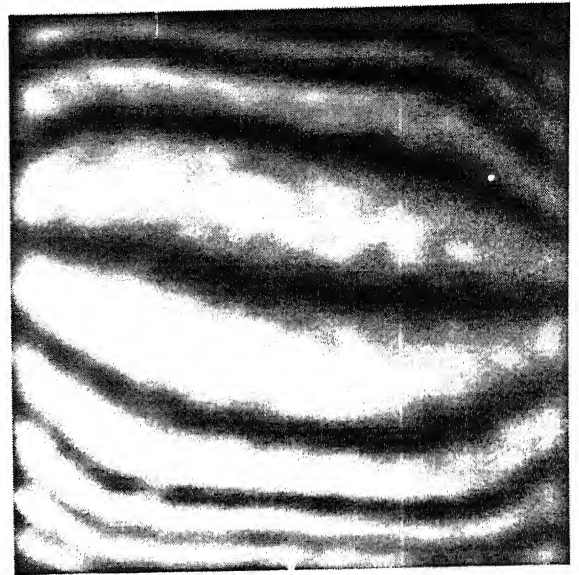
Figure 4.9(a) and Figure 4.9(b) are the Fourier filtered images of Figure 4.7 (d) with different filtering parameters and Figure 4.9(c) and Figure 4.9(d) are the thinned image and the superimposed thinned image respectively. From the calculation of temperature of fringes and Nusselt number, it was observed that there was no effect of the filtering parameter on data analysis.

At steady state, the variation of the temperature field plotted as a function of the vertical distance is shown in Figure 4.10 for two equally spaced columns of the cavity. It is to be recalled that the  $y$ -coordinate is measured from the cold top wall.

Heat transfer rates at the boundary walls in terms of the local Nusselt number has been calculated by using the Equation 3.19.

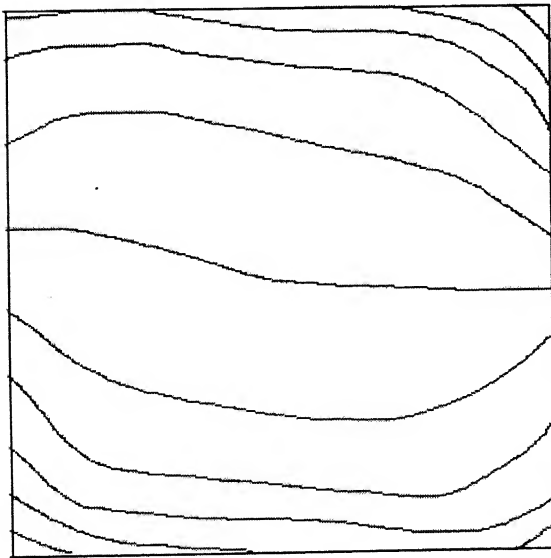


(a)

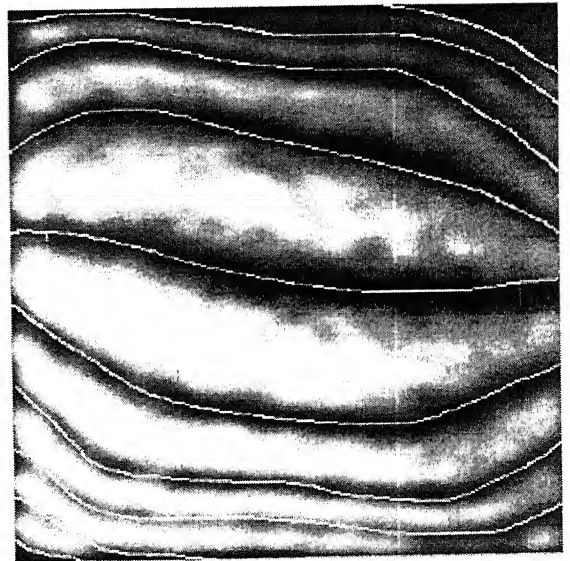


(b)

Figure 4.8: (a) Original Interferogram (b) Filtered Interferogram



(c)



(d)

Figure 4.8: (c) Thinned Image (d) Superimposed Thinned Image for air when the cavity is with optical windows for Air for  $Ra=34,200$

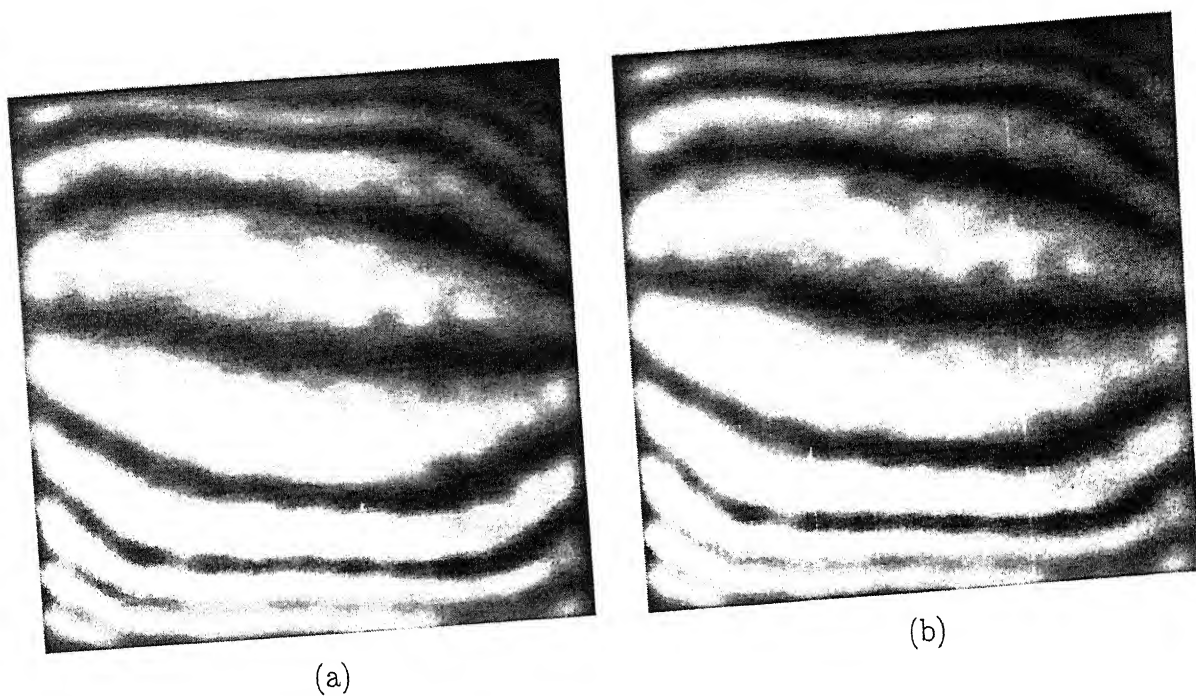


Figure 4.9: Fourier Filtered images with different filtering parameters  
(a) cutoff=50, (b) cutoff=100

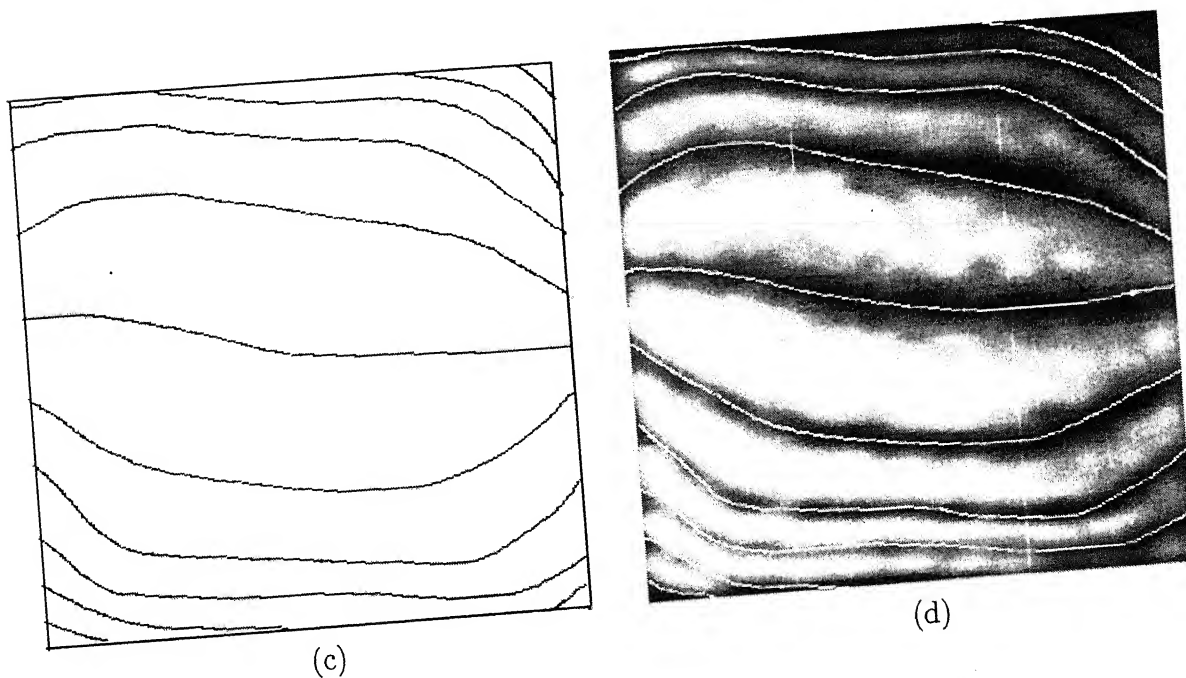


Figure 4.9: (c) Thinned Image (d) Superimposed Thinned Image

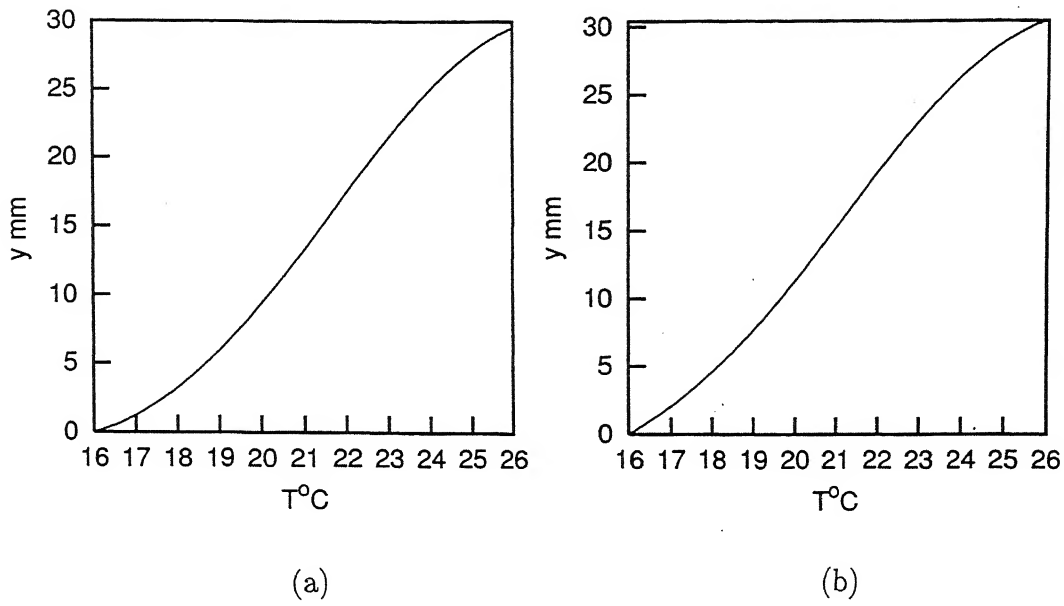


Figure 4.10: Temperature Profiles for two equally spaced columns of cavity for (a)  $x=1.07$  mm and (b)  $x=21.4$  mm

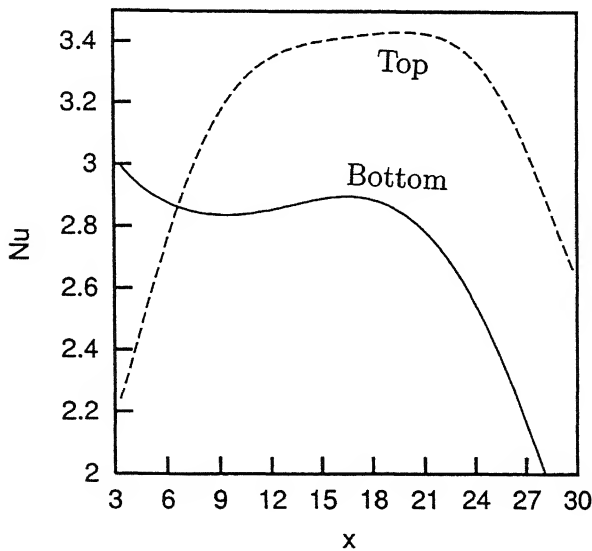


Figure 4.11: Local Nusselt number variation at the top and bottom walls for Air when the cavity is with optical windows for  $Ra=34,200$

Figure 4.11 shows the variation of local Nusselt number at the top and bottom walls of the cavity. The individual plate averaged Nusselt number for the case of air with windows were found to be 2.90 and 3.23 at the cold and the hot surfaces respectively of the cavity. The average Nusselt number for each of the plates has also been compared with the experimental correlation given by Gebhart *et al.* (1988), Equation 3.20. The value of average Nusselt number as calculated from Equation 3.20 is 3.17. The Nusselt number calculated in the present experiment matches well with the reference correlation.

## 4.2 Convection in a water filled cavity

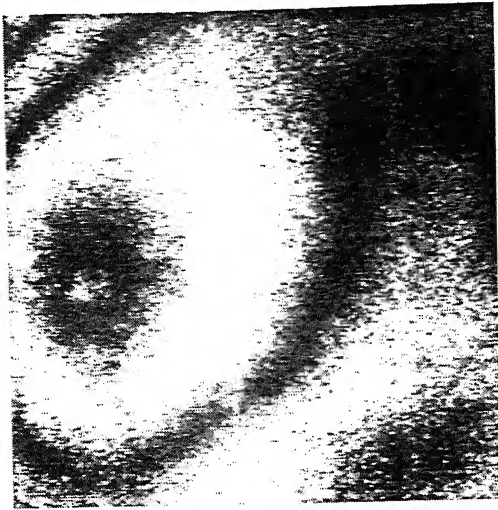
Experiments with the test cell filled with water are reported in the present section. The hot and the cold walls of the cavity were maintained at 16 and 26°C respectively, the effective temperature difference is 10°C. to get meaningful fringe patterns, it was found necessary to fill the reference chamber also with water. The Rayleigh number for the present experiment was calculated to be 16,69,314. Interferograms were recorded at various time instants, but no clear steady state was to be seen. This is understandable because the Rayleigh number for the present experiment stretches well into the turbulent regime. Keeping in mind the low sensitivity of refractive index of water to temperature, one can anticipate a large number of fringes in water.

Figure 4.12 shows the infinite fringe setting of the interferometer without and with a candle flame. The fringes for the candle flame in the presence of the test cell with water confirm that the optical alignment has been proper. Figure 4.13 shows the transient evolution of the thermal field. Since the Rayleigh number is extremely high, the fringe patterns are seen to change rapidly. The patterns show that the flow is in three-dimensional turbulence zone.

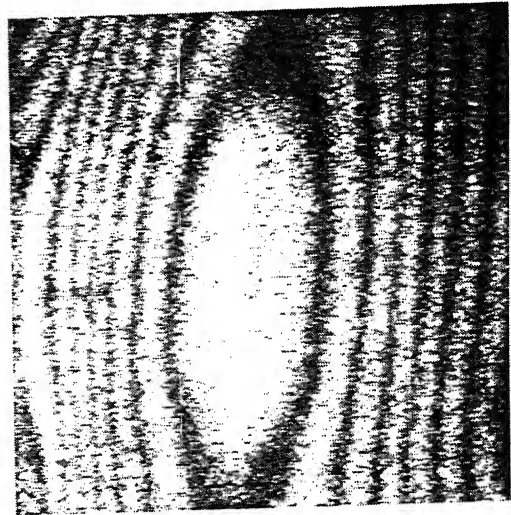
Figure 4.14(a) and Figure 4.14(b) show the original image along with Fourier filtered image respectively.

Figure 4.14(c) shows thinned image and Figure 4.14(d) shows superimposed thinned image for a cold wall temperature  $T_c=16^\circ\text{C}$  and a hot wall temperature  $T_h=26^\circ\text{C}$ .



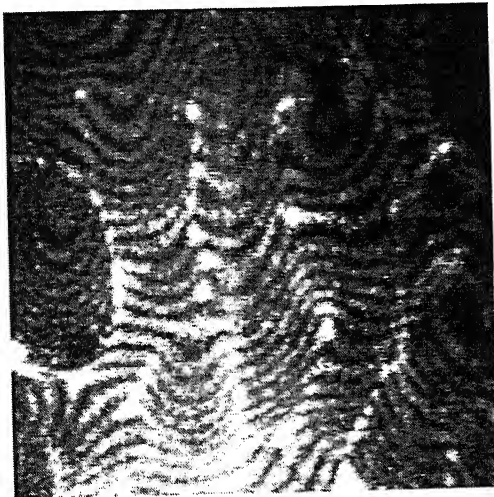


(a)

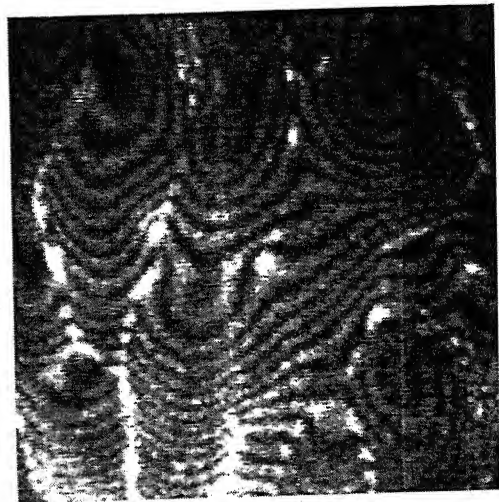


(b)

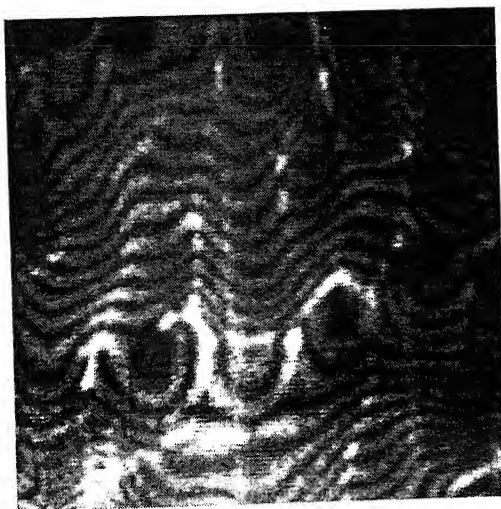
Figure 4.12: Infinite Fringe setting (a) without and (b) with Candle Flame in a Water filled Cavity



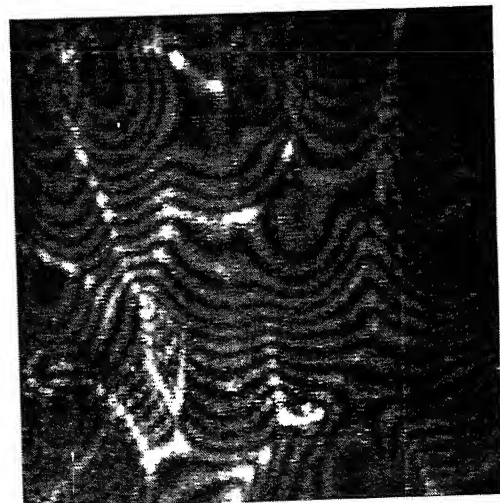
1hour:20minutes (a)



2:20 (b)



3:00 (c)



5:00 (d)

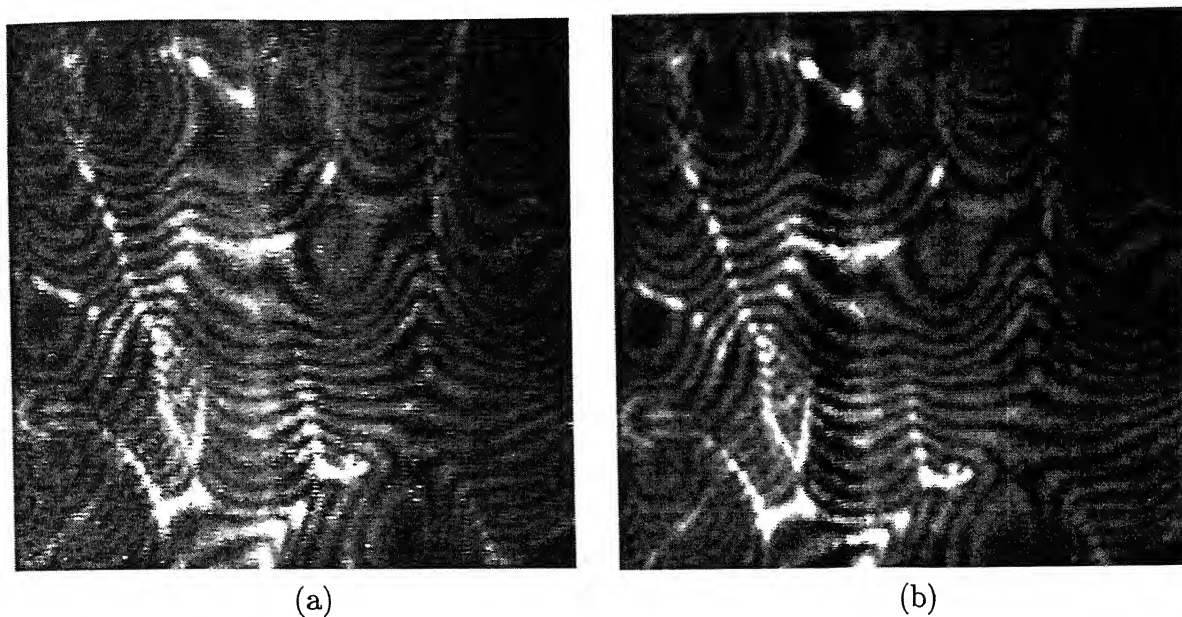


Figure 4.14: (a) Original Interferogram (b) Filtered Interferogram

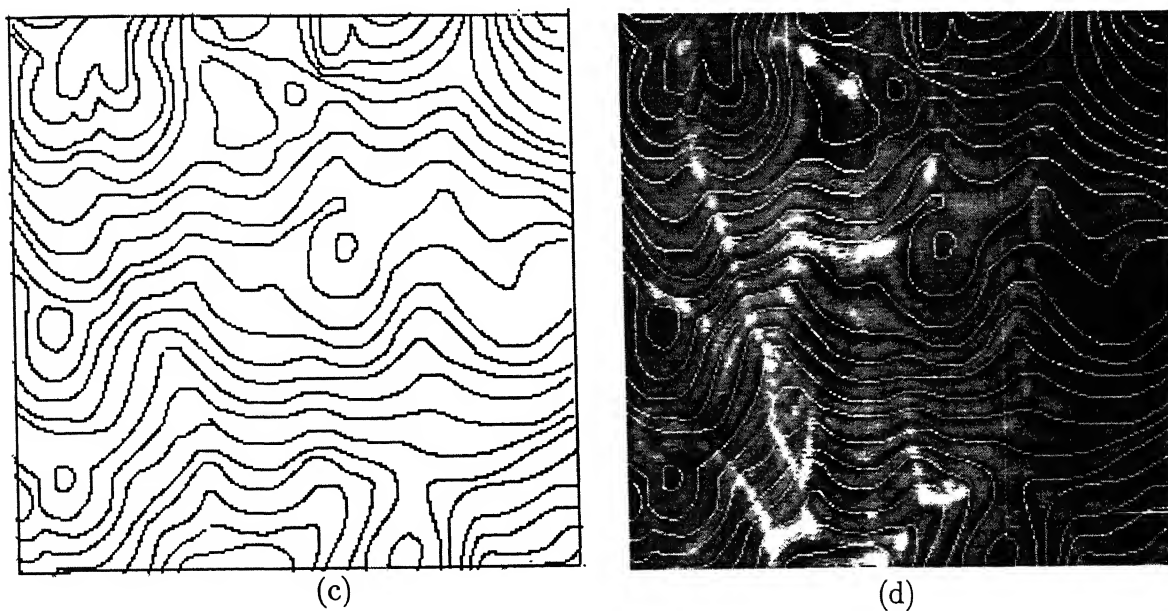


Figure 4.14: (c) Thinned Image (d) Superimposed Thinned Image for Water  $Ra=16,69,314$

In the present experiment it was not possible to clearly identify the near wall fringes for this reason the local as well as the average wall heat transfer rate could not be calculated. Continuous fringes however could be seen in the middle of the test cell. Transverse heat transfer based on the fringe spacing near the core showed the Nusselt number to be close to 0.07. This is to be contrasted with the correlation of Gebhart *et al.* (1988) Equation 3.19, which gives a Nusselt number of 10.0. The difference between the two arises from the fact that the wall heat transfer is diffusion dominated, while in the core of the cavity heat transfer is predominantly by advection.

### 4.3 Convection in a cavity half filled with water

Experiments have been conducted with the test cell filled with water upto the mid-plane. The cavity thus contains two fluid phases, namely air and water. To generate fringe patterns successfully with the interferometer, the reference chamber was also maintained with water upto its mid-plane. An unexpected difficulty was encountered during the alignment of the test and reference beams with respect to the interface. Owing to mild refraction effects, the interface appeared on the screen as a dark band. The width of the band was brought to within limits by improving the alignment of the apparatus repeatedly. Thermal fields above and below the interface could be recorded by the interferometer and being seen to be insensitive to the width of the band. It was however found necessary to check for the alignment of the interferometer individually for the air and the water phases.

Experiments have been conducted with the hot and cold surfaces maintained at 26 and 16°C. The corresponding Rayleigh number in air and water were calculated to be 4,185 and 16,413 respectively. These numbers are based on the half cavity height and the interface temperature calculated as in Appendix A.

#### 4.3.1 Convection in the air phase

Figure 4.15(a) and Figure 4.15(b) show the infinite fringe setting of the interferometer without and with the candle flame respectively. The black band in the center is due to the interference of the reflected and the refracted beams of light from the water and air portions of the cavity. The fluid above the band is air and

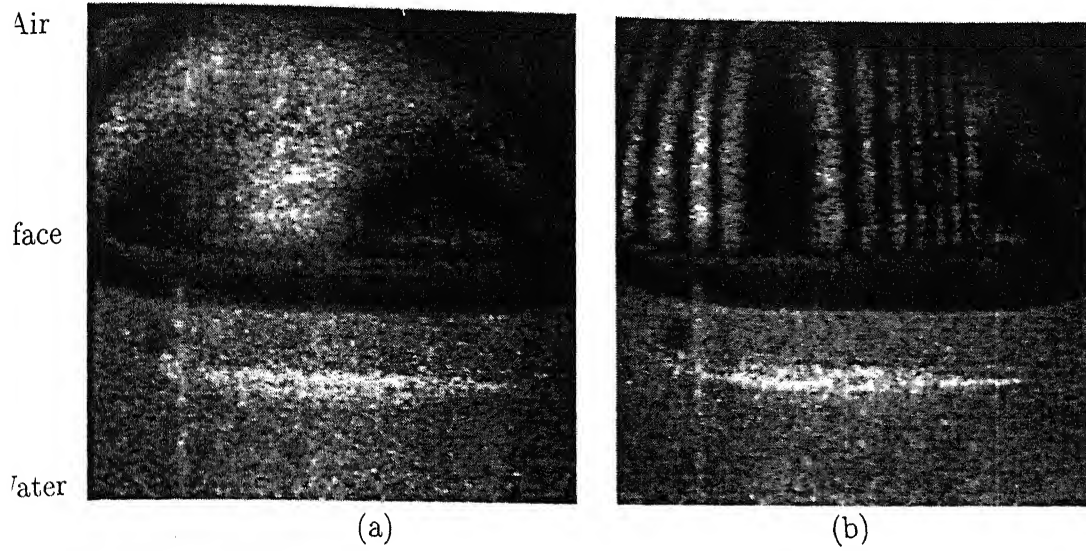


Figure 4.15: Infinite Fringe setting (a) without and (b) with Candle Flame

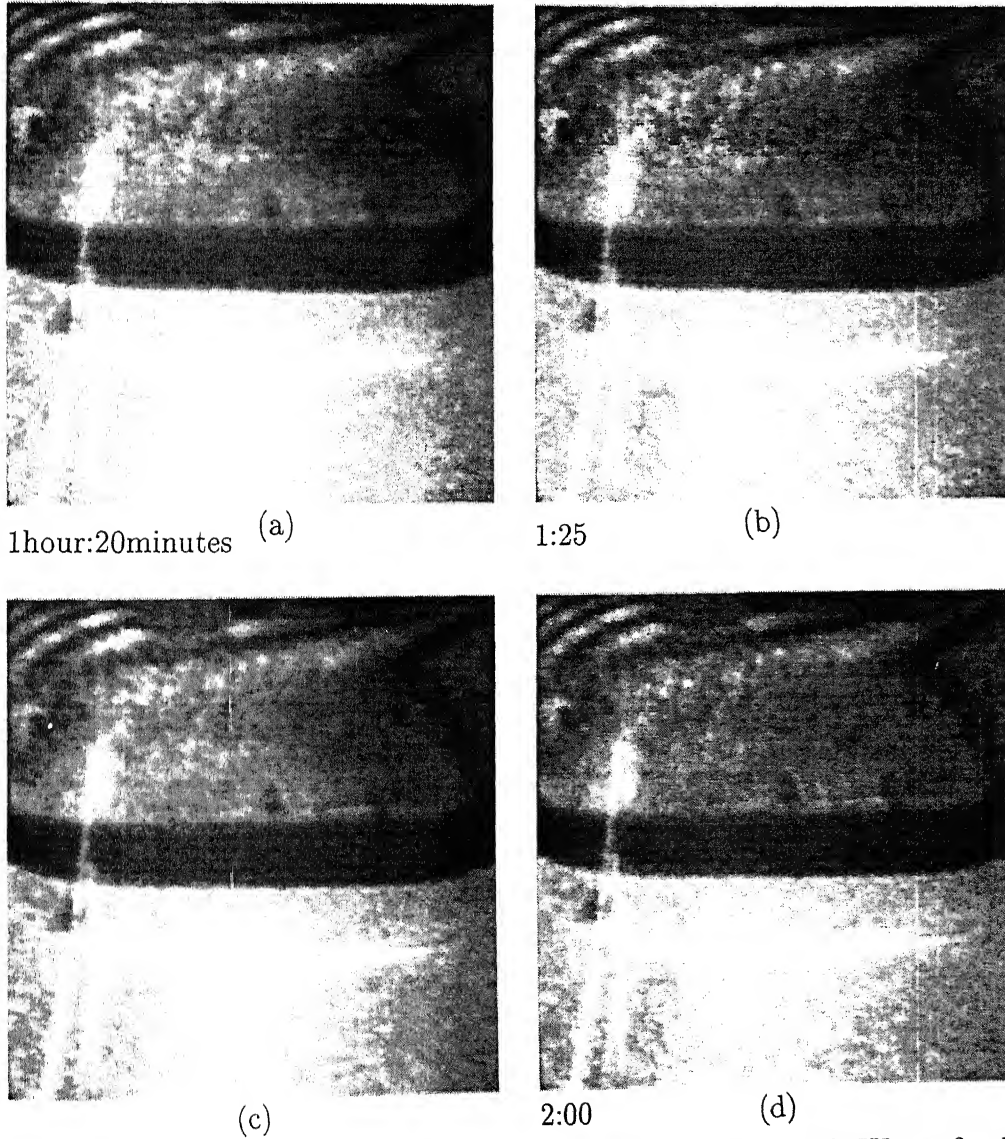


Figure 4.16: Evolution Patterns for air when the cavity is half filled with Water for  $T_c=16^\circ\text{C}$ ,  $T_h=26^\circ\text{C}$  and  $Ra(\text{air})=4.185$  and  $Ra(\text{water})=16,413$



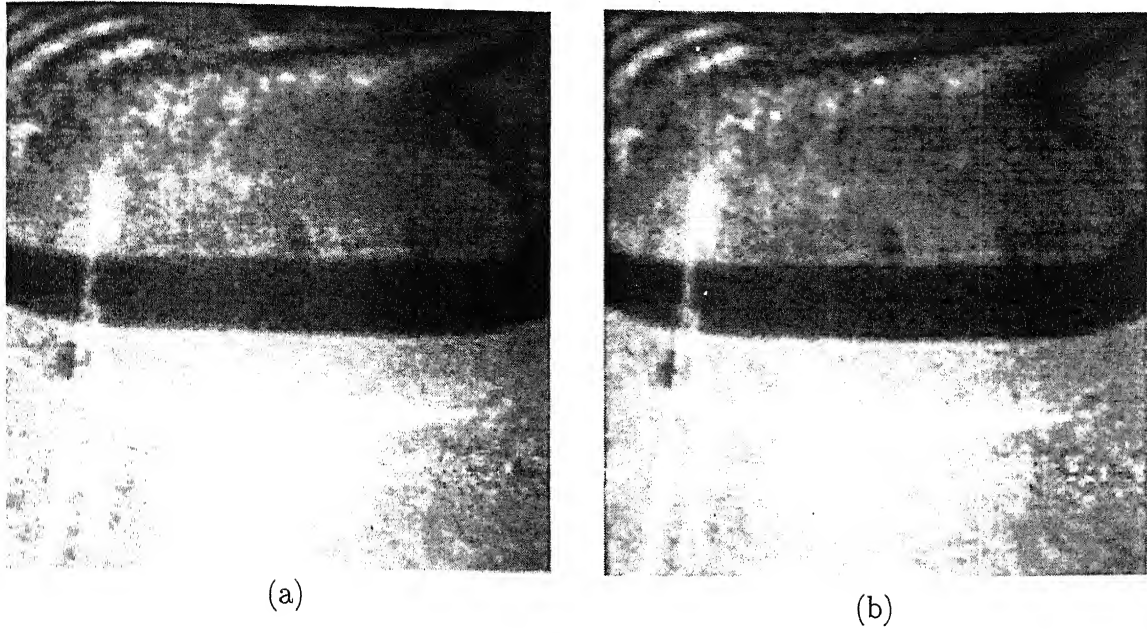


Figure 4.17: (a) Original Interferogram (b) Filtered Interferogram

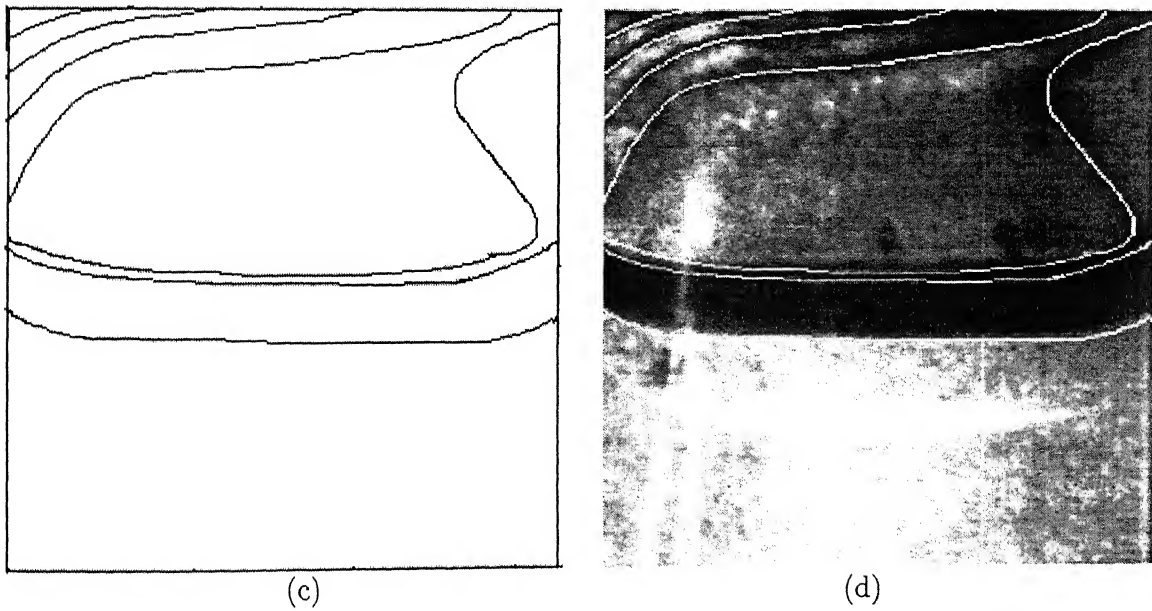


Figure 4.17: (c) Thinned Image (d) Superimposed Thinned Image for Air for  $T_c=16^\circ\text{C}$ ,  $T_h=26^\circ\text{C}$  and  $Ra_{air}=4,185$  and  $Ra_{water}=16,413$

below is water.

Figure 4.16 shows the transient evolution of the thermal field in air till the steady state is reached. The interferograms were collected at regular intervals of time. In this case also steady state obtained very fast. The fringes are not straight lines but have some curvature. From the figure it is clear that the isotherm spacings near the top wall and the interface are less than the spacing in the central region. Here the number of fringes is lower than that of the experiment in which the cavity is filled with air. This is because the Rayleigh number is lower. In the present experiment, we encountered a new problem of dew formation on the optical windows. Hence all the fringes could not be captured. Reflection of light from water in the air portion of the cavity is seen in Figure 4.16.

Once the flow field was fully evolved, the fringe patterns were observed to be quite steady. Figure 4.16 shows the steady state nature of the flow field. These interferograms were recorded after one and half hours of the experimental run time to ensure the steady state behavior of the convection pattern. The number of fringes is around 3 at steady state.

Figure 4.17(a) and Figure 4.17(b) show the original steady state image along with Fourier filtered image respectively. Figure 4.17(c) shows thinned image and Figure 4.17(d) superimposed thinned image for air for  $Ra=4185$ . From the thinned image, local temperature and Nusselt number are calculated.

### 4.3.2 Convection in the water phase

For getting the fringe patterns in water, the water layer in the test cavity was matched with that of the reference cell. Infinite fringe setting was then achieved for the water phase alone.

Figure 4.18(a) and Figure 4.18(b) show the infinite fringe setting of the interferometer without and with the candle flame respectively. The black patch once again represents the interface. Figure 4.19 shows the transient evolution of the thermal field in water till the steady state is reached. The interferograms were collected in regular intervals of time. Figure 4.19(a) has fewer number of fringes than at steady state, namely Figure 4.19(c) and Figure 4.19(d). Figure 4.19(b) was recorded just before the steady state reached. The number of fringes increases continuously till steady state reached.

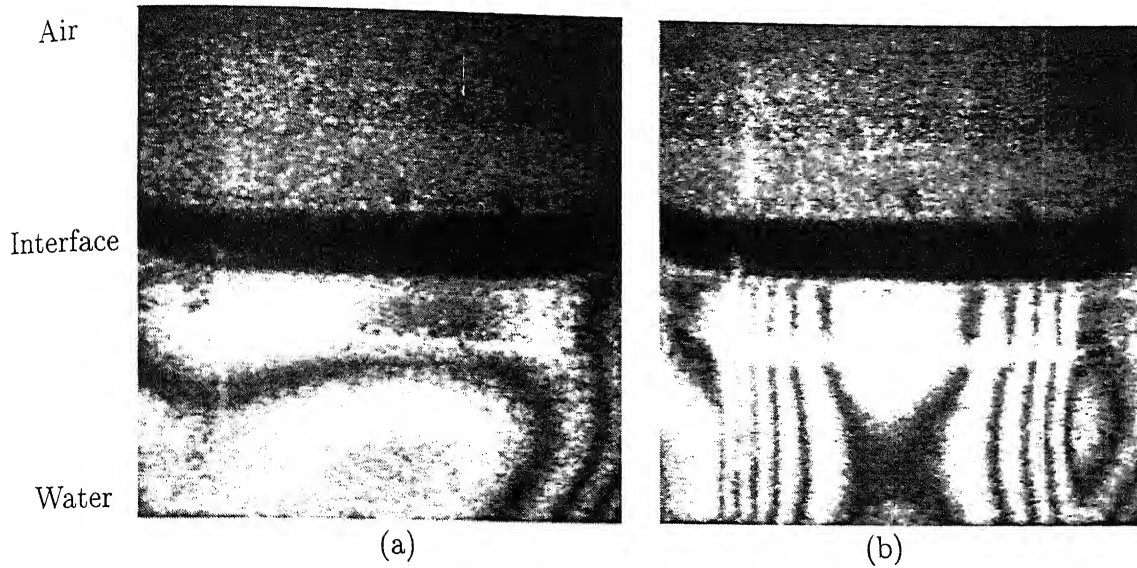


Figure 4.18: Infinite Fringe setting (a) without and (b) with Candle Flame

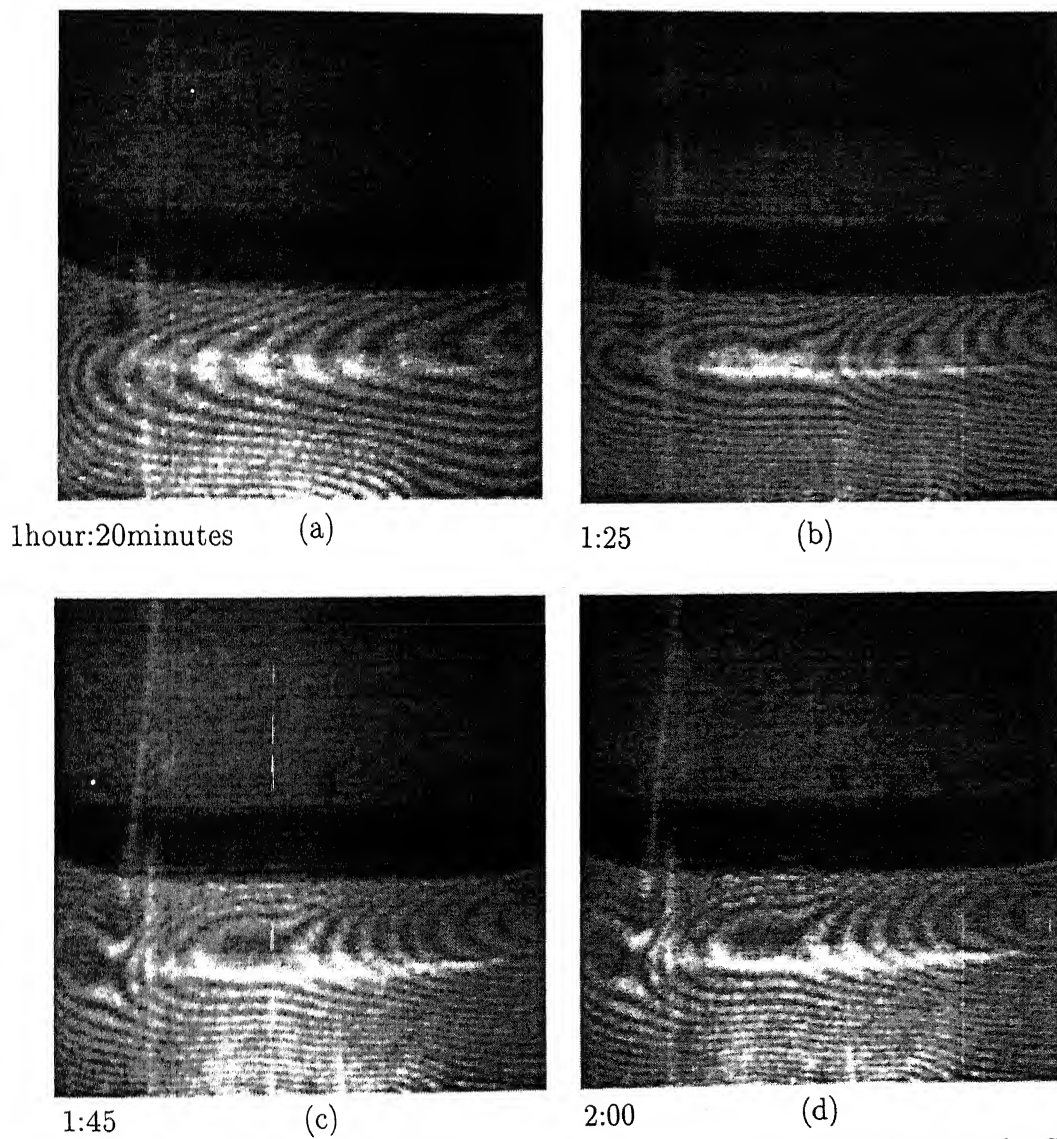


Figure 4.19: Evolution Patterns for Water when the cavity is half filled with Water for  $T_c=16^\circ\text{C}$ ,  $T_h=26^\circ\text{C}$  and  $Ra_{air}=4,185$  and  $Ra_{water}=16,413$

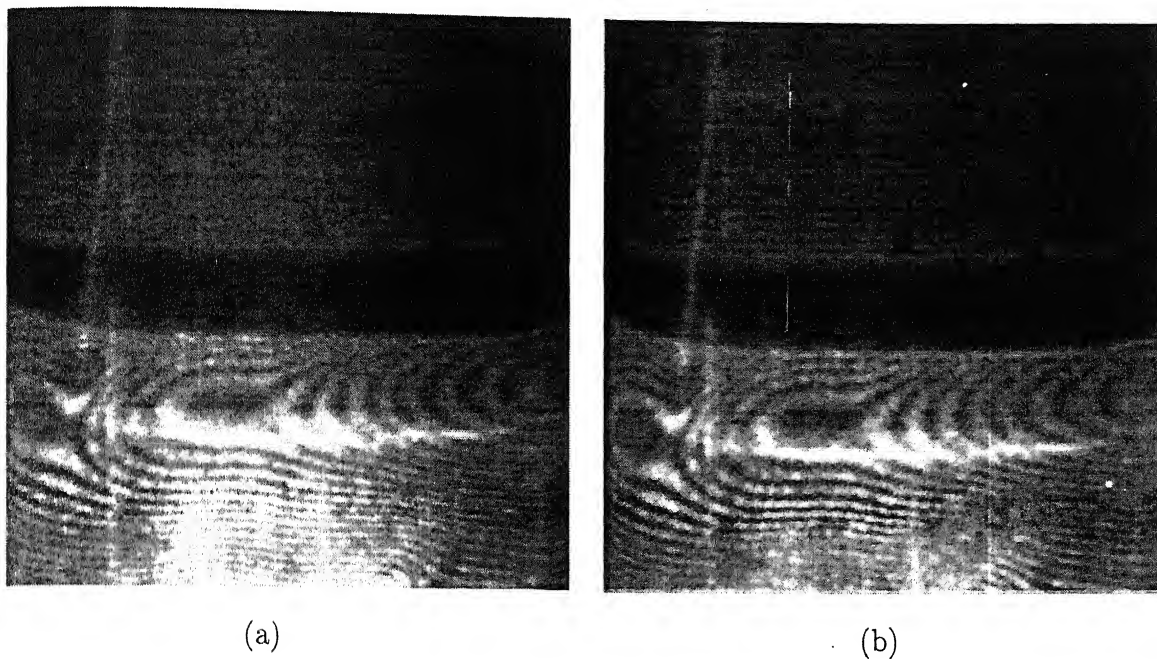


Figure 4.20: (a) Original Interferogram (b) Filtered Interferogram

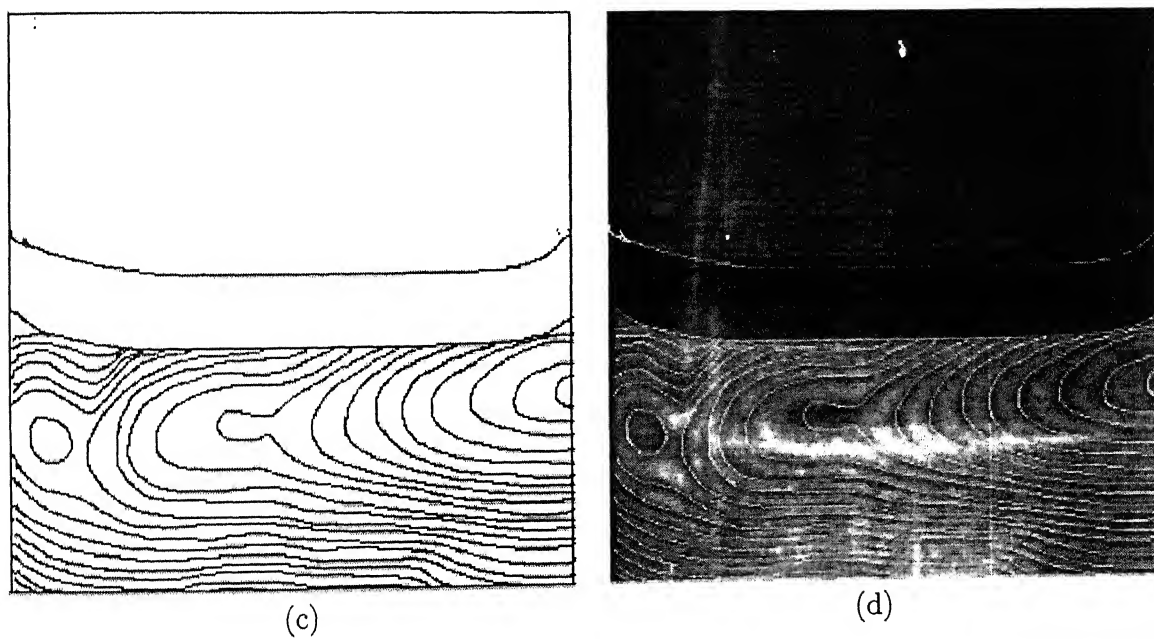
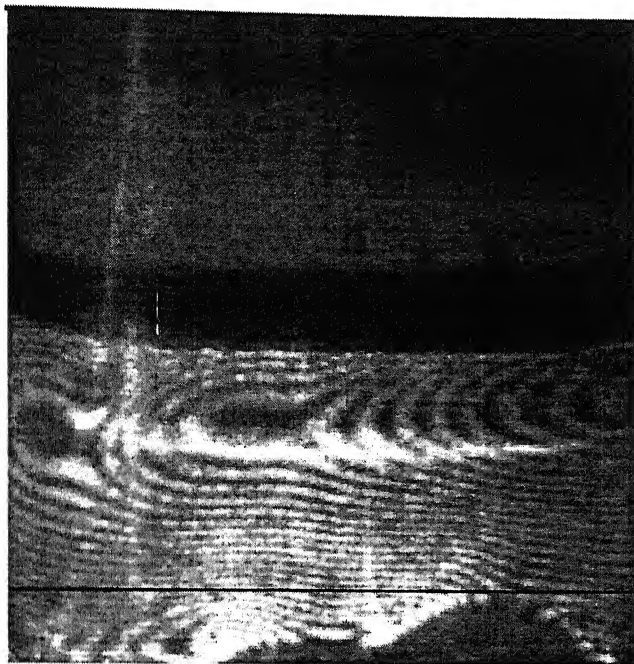


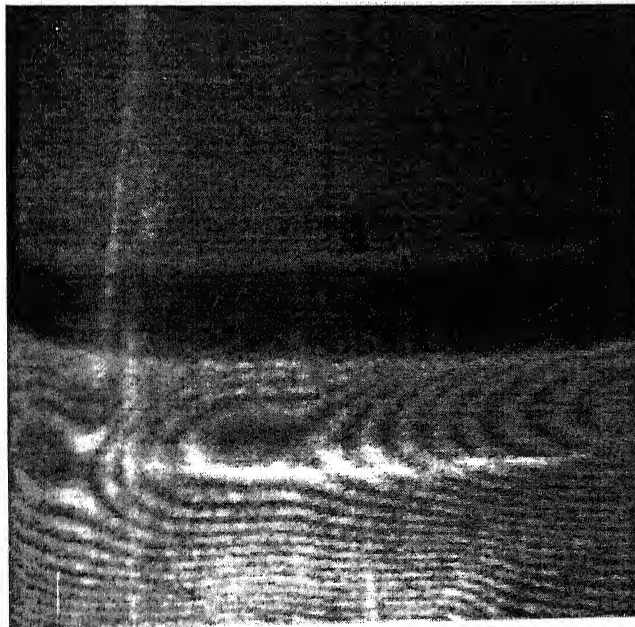
Figure 4.20: (c) Thinned Image (d) Superimposed Thinned Image for Water when the cavity is half filled with water for  $Ra_{air}=4,185$  and  $Ra_{water}=16,413$



Hot Wall



(a)

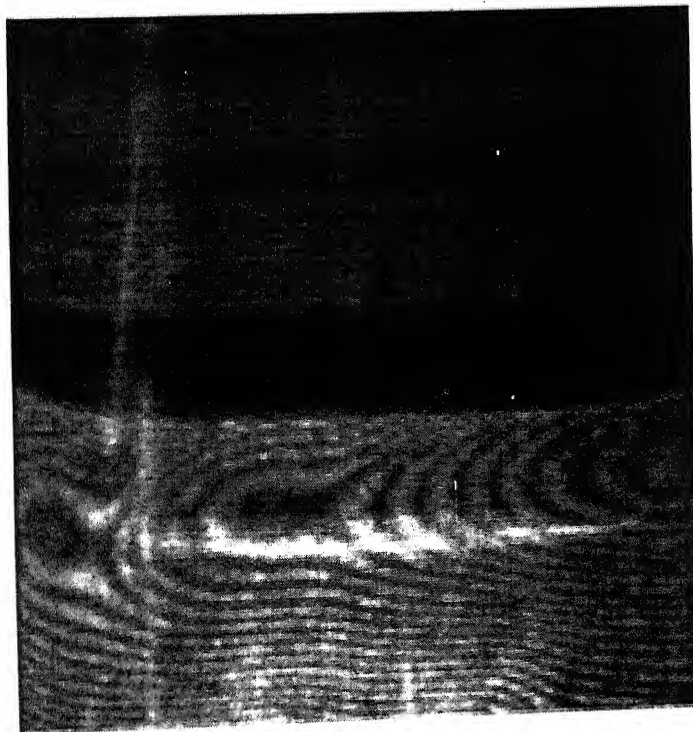


(b)

Figure 4.21: (a) Raw image with extraneous features and (b) Modified image



(a)



(b)

Figure 4.22: Steady state pattern for (a) air and (b) water

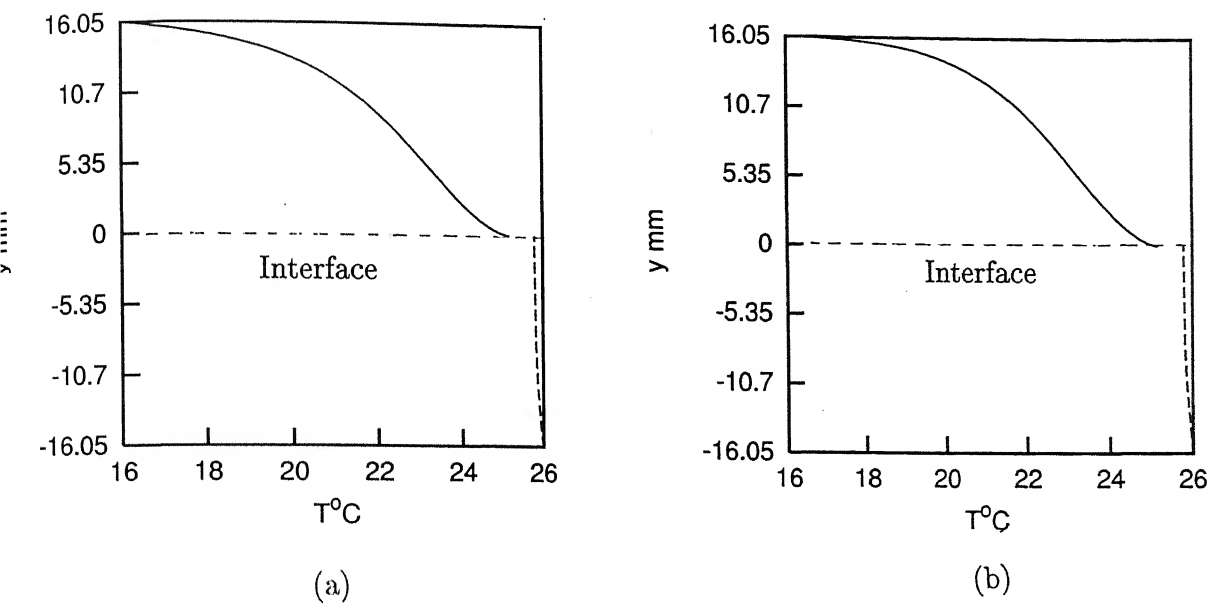


Figure 4.23: Temperature Profiles in the cavity half filled with water at (a)  $x=1.07$  mm and (b)  $x=21.4$  mm

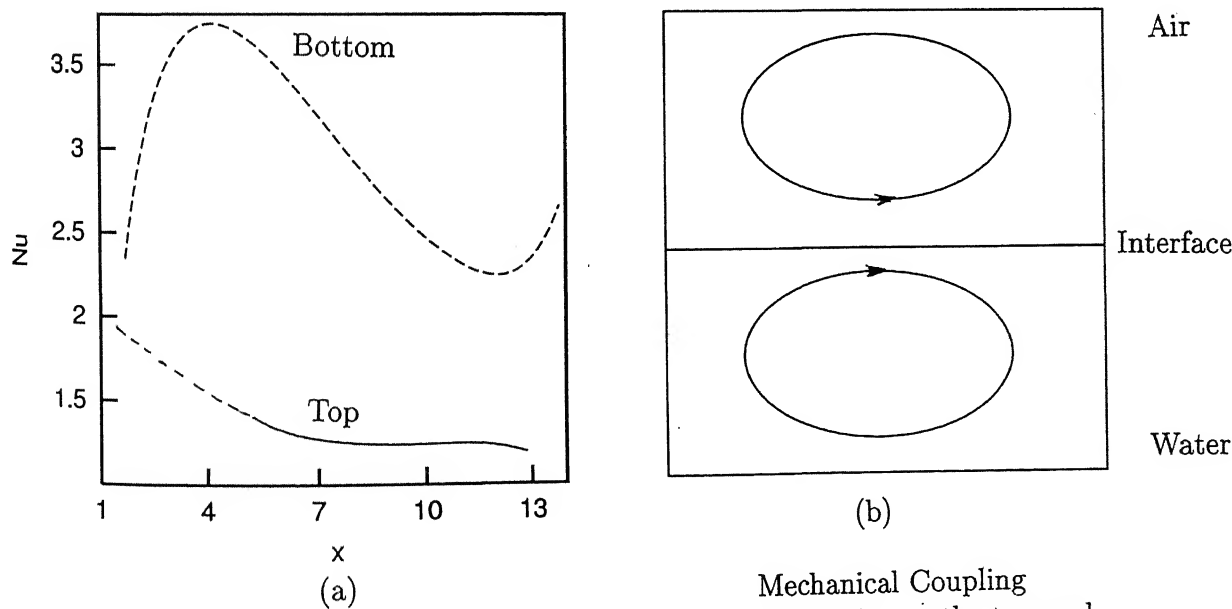


Figure 4.24: (a) Local Nusselt number variation at the top and bottom walls (b) Rolls formation in air and water

The fringes are not straight lines but have a curvature. From the figure it is clear that the isotherm spacings near the interface and bottom wall of the cavity is less than the spacing in the central region of the test section. Here the number of fringes is lower than for the experiment in which the cavity is fully filled with water. This is because the Rayleigh number is lower. Once the flow field has fully evolved, the fringe patterns were observed to be quite steady. Figure 4.19 shows the steady state nature of the flow field. These interferograms were recorded after one and half hours of the experimental run time to ensure the steady state behavior of the convection pattern. The number of fringes is around 12 at steady state.

Figure 4.20(a) and Figure 4.20(b) shows the original steady state image along with Fourier filtered image respectively. Figure 4.20(c) shows thinned image and Figure 4.20(d) shows the superimposed thinned image at  $Ra=16,413$ . From this thinned image, calculation for temperature of the fringes and Nusselt number can be carried out.

While working with two fluid layers of air and water, unexpected difficulties were experienced during interferometry. Two such factors already referred above are the broadening of the interface into a black patch and dew formation on optical windows. In addition, mild refraction effects from the cavity walls got amplified over the balancing arms of the interferometer. The image thus formed was larger than the true size of the cavity. Certain ghost features were also revealed in the interferogram. It was however possible to eliminate the undesirable features of the image by using an eye-judgement. The original and the modified images showing the extraneous features as well as their removal are shown in Figures 4.21(a) and (b) respectively. The Figure 4.22(a) and Figure 4.22(b) are the steady state pattern for air and water when the cavity is half filled with water and air.

At steady state, the variation of the temperature field plotted as a function of the vertical distance as shown in Figure 4.23 for two equally spaced columns along the width of the cavity. The  $y$ -coordinate is measured from the interface. From the figure it is seen that there is more temperature drop in air than in water. Figure 4.24(a) shows the local Nusselt number variation at the top and bottom walls of the cavity.

Figure 4.24(b) shows the roll formation in both the portions. From the convection pattern it is understandable that the fluid layers are mechanically coupled.

पुरुषोत्तम लाल शर्मा  
भारतीय प्रौद्योगिकी संस्थान दिल्ली  
134238  
पृष्ठ सं. A.....

Heat transfer rates at the hot and the cold walls in terms of the local Nusselt number have been calculated by using Equation 3.19. Figure 4.24(a) shows the variation of local Nusselt number at the top and bottom walls of the cavity. The individual plate averaged Nusselt number for the case of two layer problem are 1.26 and 2.33 at the cold and the hot surfaces respectively. The average Nusselt number for each of the plates has also been compared with the experimental correlation given by Gebhart *et al.* (1988), Equations 3.20 and 3.21. The value of average Nusselt number as calculated from Equation 3.20 is 1.85 for air and from Equation 3.21 is 3.68 for water. There is a difference between the Nusselt number from the present experiment and the correlation. The correlation considers the temperature of hot and cold walls where the heat transfer mechanism is conduction. In the present experiment one of the boundaries is an interface between the two fluids and not rigid wall. Heat transfer at the fluid interface is dominated by convective effects.

### 4.3.3 Experiments with a new set of surface temperatures

For most fluids, all thermophysical properties including thermal conductivity and viscosity are temperature dependent. To examine the sensitivity of the thermal field to the average temperature level in the cavity, experiments were repeated with new temperature levels of 34 and 24°C, keeping the cavity temperature difference at the original value of 10°C. The original fringes in air and water as well as the processed images are presented in Figure (4.25-4.31). These figures are seen to be remarkably similar to those presented in Sections 4.3.1 and 4.3.2.

The essential conclusion to emerge from the above experiment is that the thermal field is buoyancy dominated, being dependent on the changes in density with the changes in temperature. The temperature dependence of the conductivity and viscosity play a very insignificant role in deciding the convection pattern.

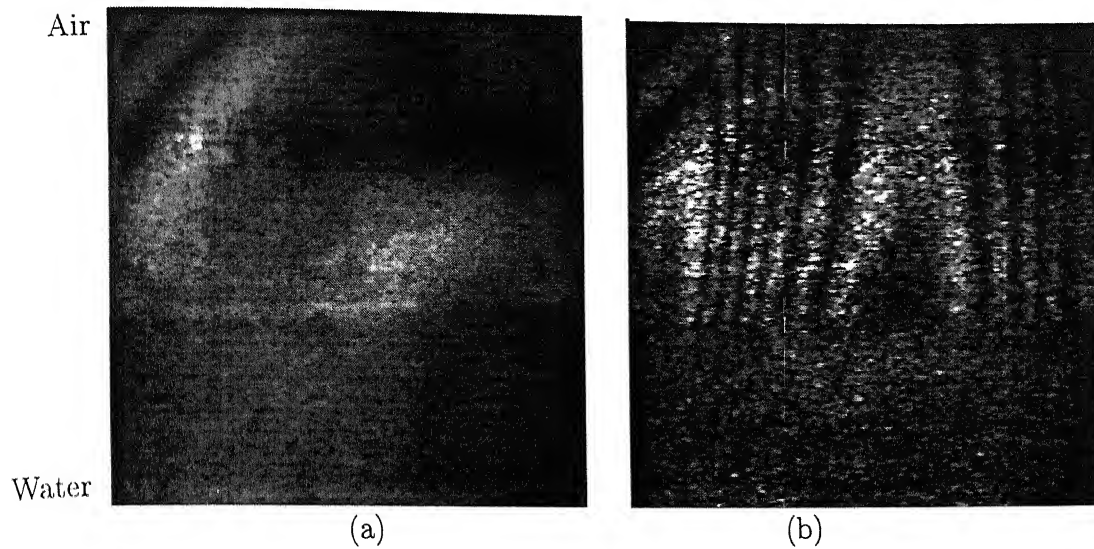


Figure 4.25: Infinite Fringe setting (a) without and (b) with Candle Flame

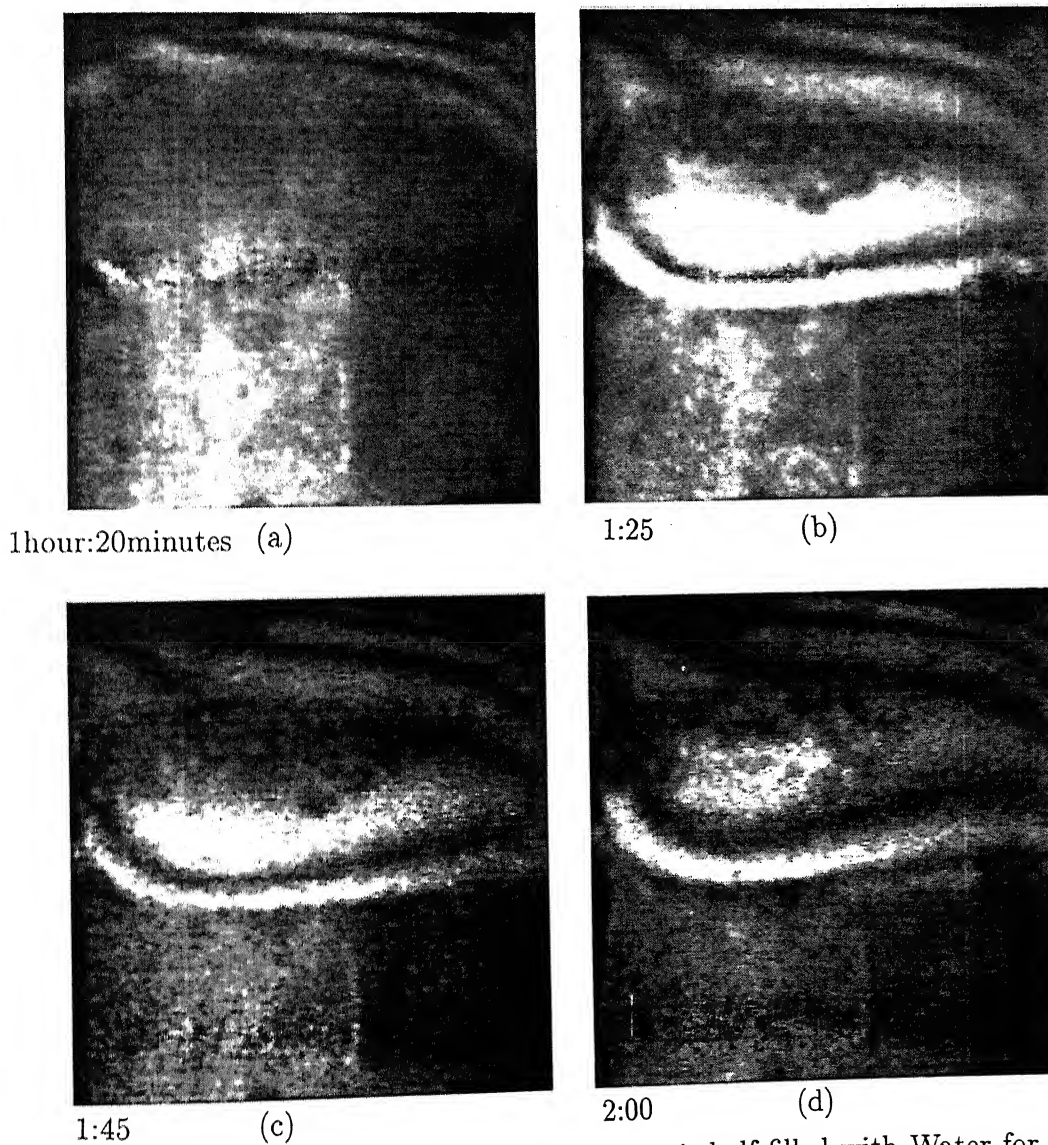


Figure 4.26: Evolution Patterns for Air when the cavity is half filled with Water for  $T_c=24^\circ\text{C}$ ,  $T_h=34^\circ\text{C}$ ,  $Ra_{air}=3,699$  and  $Ra_{water}=22,350$



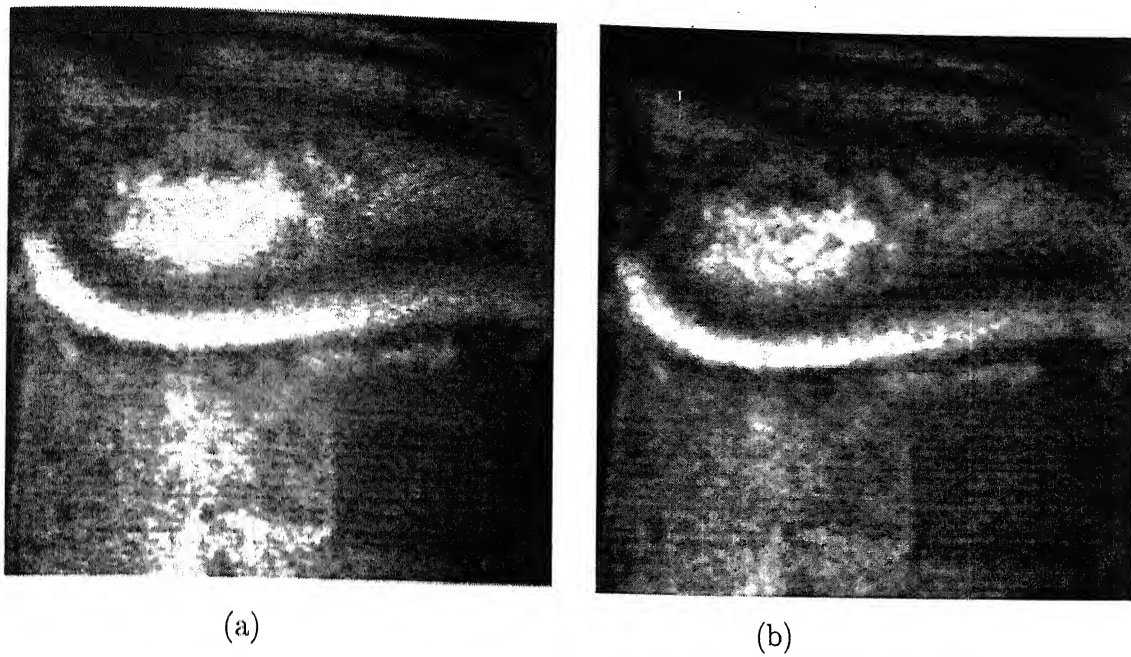


Figure 4.27: (a) Original Interferogram (b) Filtered Interferogram

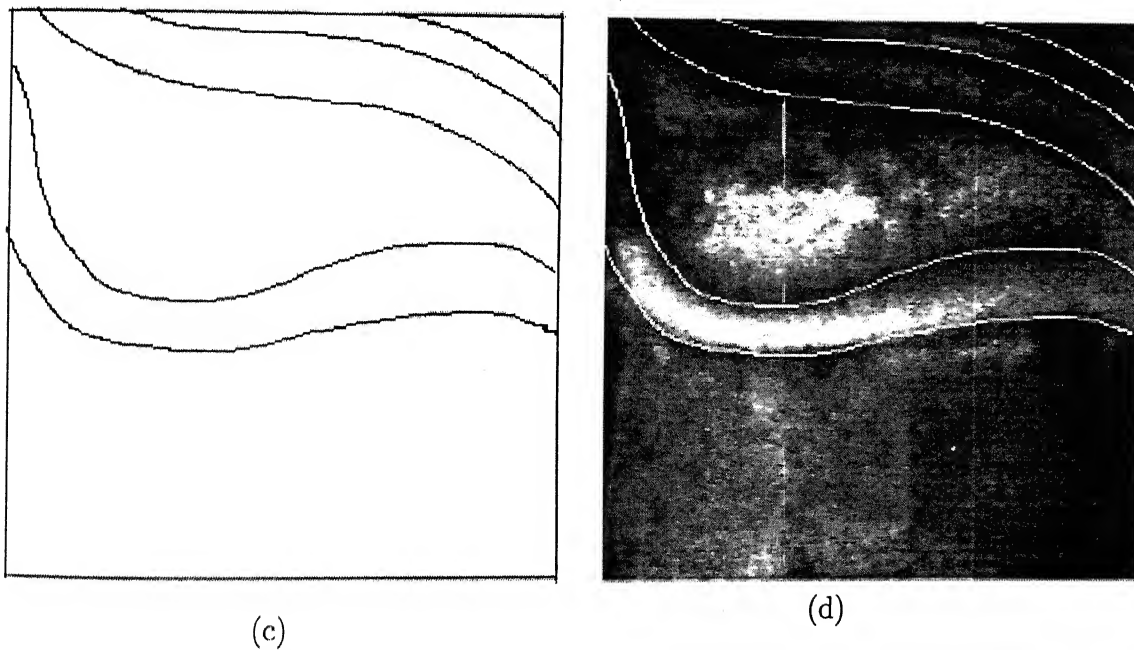


Figure 4.27: (c) Thinned Image (d) Superimposed Thinned Image for Air when the cavity is half filled with water for  $Ra_{air}=3,699$  and  $Ra_{water}=22,350$

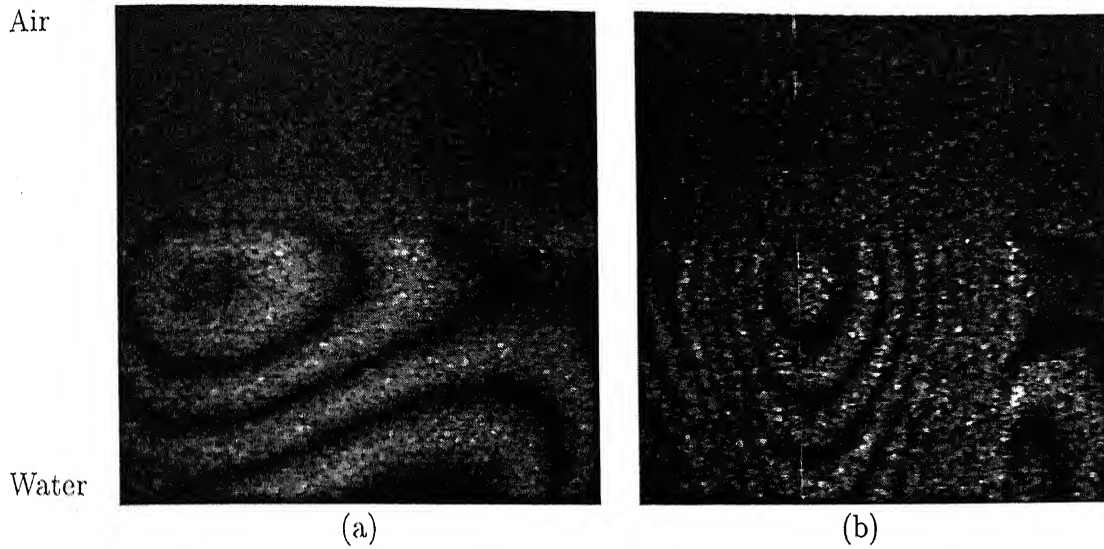


Figure 4.28: Infinite Fringe setting (a) without and (b) with Candle Flame

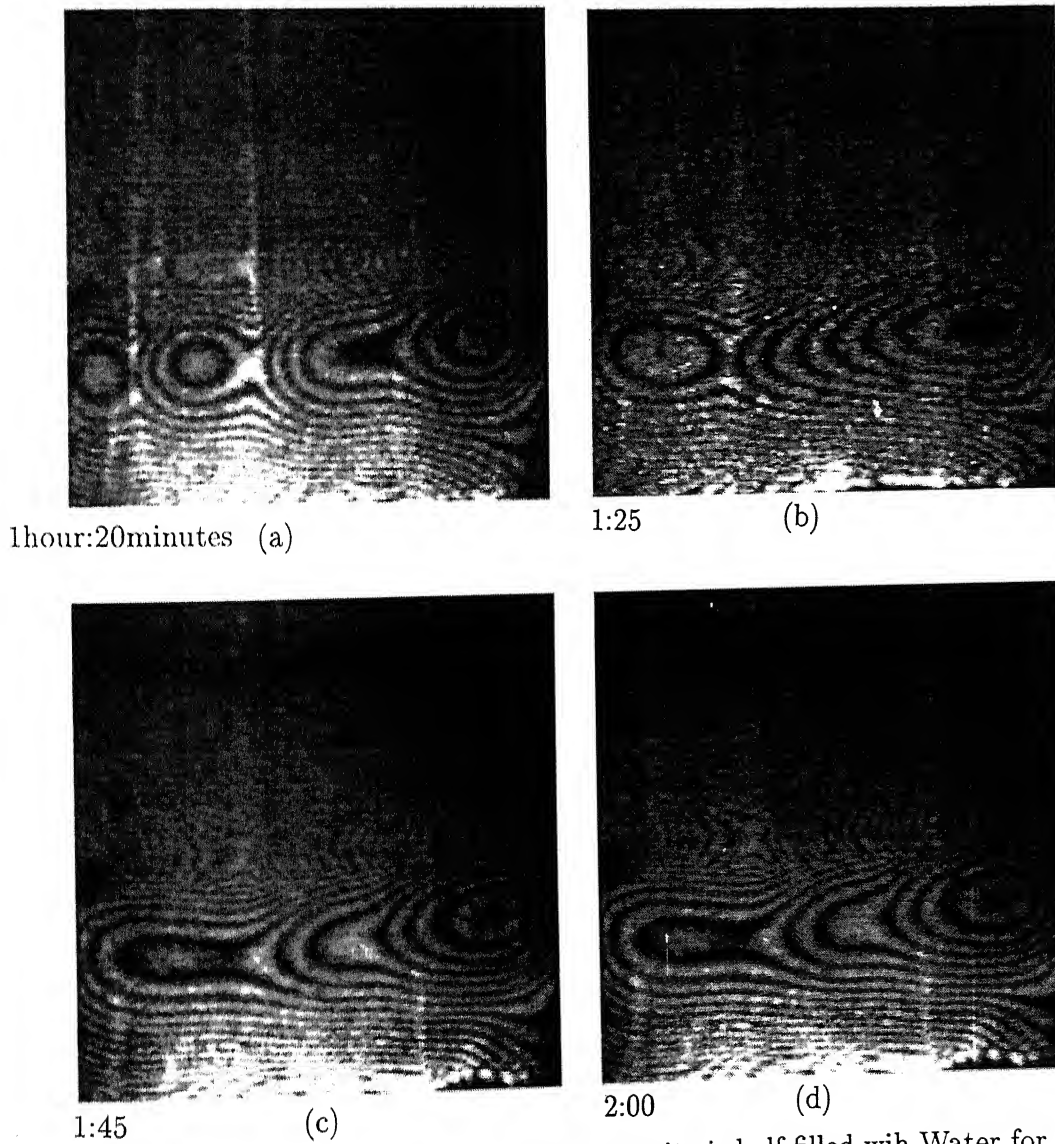


Figure 4.29: Evolution Patterns for Water when the cavity is half filled with Water for  $T_c=24^\circ\text{C}$ ,  $T_h=34^\circ\text{C}$ ,  $Ra_{air}=3,699$  and  $Ra_{water}=22,350$



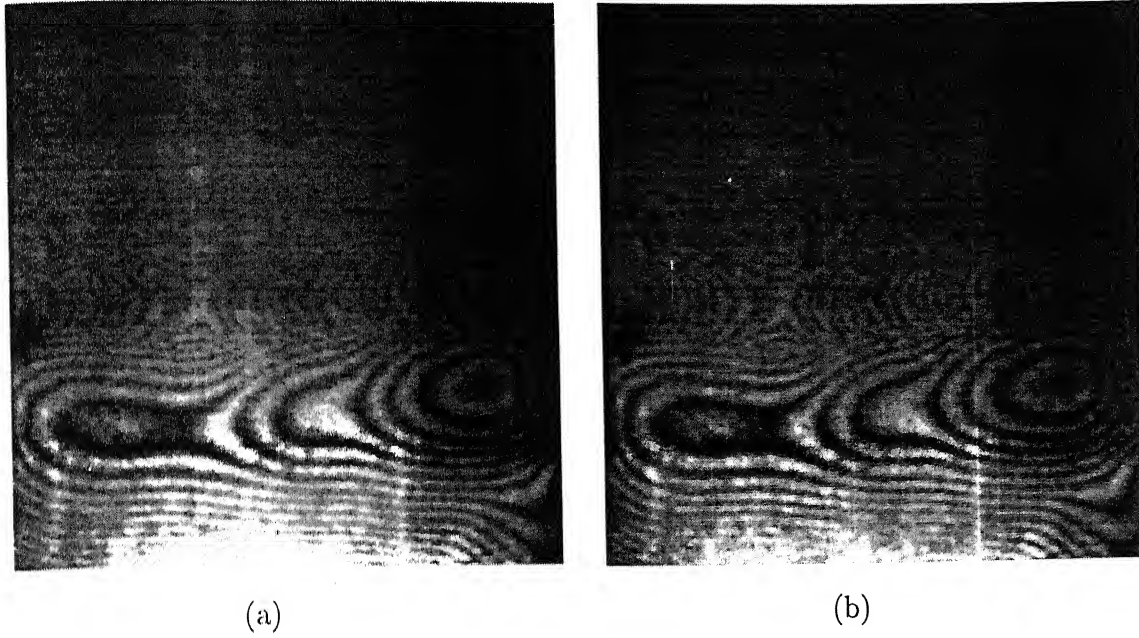


Figure 4.30: (a) Original Interferogram (b) Filtered Interferogram

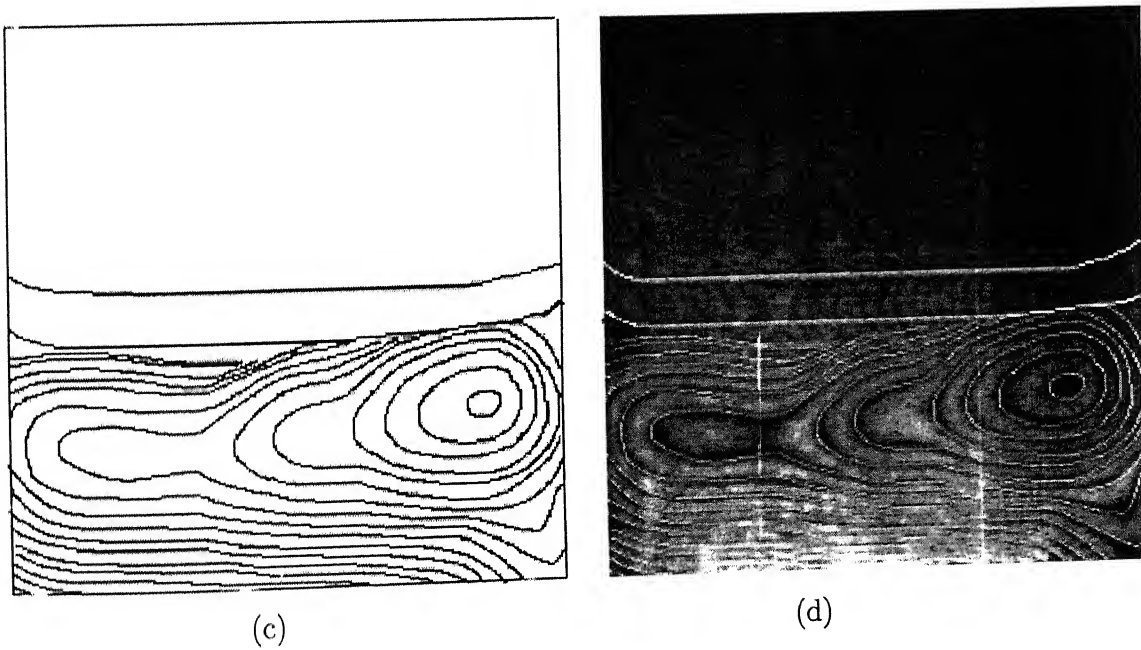


Figure 4.30: (c) Thinned Image (d) Superimposed Thinned Image for water when the cavity is half filled with water for  $Ra_{air}=3,699$  and  $Ra_{water}=22,350$

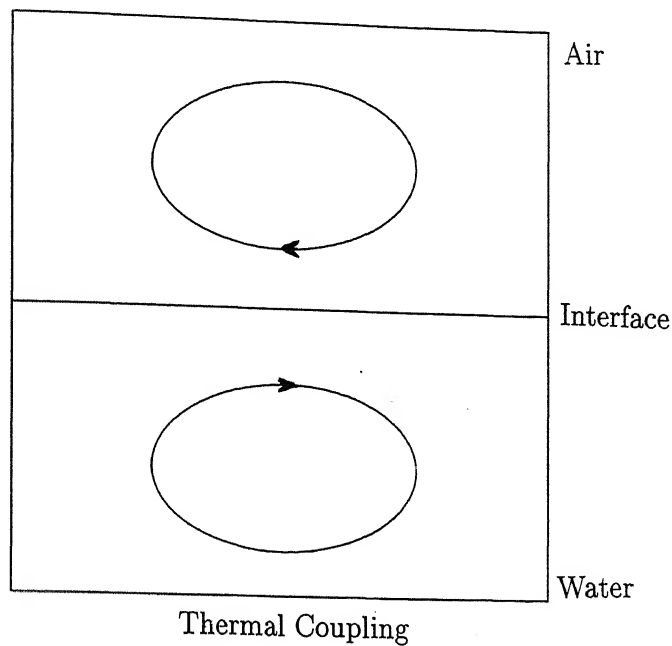


Figure 4.31: Roll patterns in air and water phase for  $Ra_{air}=3,699$  and  $Ra_{water}=22,350$

A few minor differences were however recorded with the experiments employing higher surface temperature levels. These are:

1. The fringe pattern in the air phase shows a reversal in the direction of circulation, while that in water has remained unchanged. This obstruction weakens the result of mechanical coupling between the two phases clearly recorded in the experiments at a lower temperature.
2. The air water interface is not as clearly delineated when the average cavity temperature is higher ( $29^{\circ}\text{C}$ , as in the experiments with a lower average cavity temperature of  $21^{\circ}\text{C}$ ). This can be explained partially by the reduction in surface temperature with increase in temperature and partially by the absence of a shared interface between the test and the reference beam.

## Chapter 5

# Conclusions and Scope for Future Work

Rayleigh-Benard convection in two-dimensional differentially heated fluid layers has been experimentally studied using Mach-Zehnder interferometer. The cavity has been taken to be (a) filled with air, (b) filled with water and (c) half filled with water. The driving potential in all the experiments was  $10^{\circ}\text{C}$ . The following conclusions were arrived at in the present study:

1. A steady two-dimensional convection pattern in air was seen to be established. The average Nusselt number for the cavity matched well with the published correlation.
2. When the cavity is filled with water, the Rayleigh number was extremely high and the flow was unsteady and turbulent.
3. when the cavity was half filled with water, the interface temperature was such as to produce a lower Rayleigh number in both air and water. Nearly steady convective field were seen to establish in both the phases. The interface temperature calculated from the water side was found to be quite close to that from the air side. For a cavity average temperature of  $21^{\circ}\text{C}$ , the two layers were seen to be mechanically coupled. For a cavity average temperature of  $29^{\circ}\text{C}$ , the two layers were thermally coupled.

The present research can be extended in the following manner to cover other areas of practical interest.

1. Effect of layer height on the nature of coupling between air and water.

2. Convection in low Prandtl number liquid with an overlaid air cushion.
3. Convection in superimposed immiscible liquid layers.

## REFERENCES

1. Andereck, C., David et al., Observation of time-dependent behaviour in the two-layer Rayleigh-Benard system, Proceedings of the third Microgravity Fluid Physics Conference, pp. 313-318, 1996.
2. Bejan, Adrian, Convection Heat Transfer, A Wiley-Interscience Publication, New York, 1984.
3. Busse, F.H. and Sommermann, G., Double-layer convection: a brief review and some recent experimental results, Proceedings of the 1995 AMS-IMS-SIAM Joint Summer Research Conference, pp. 33-41, 1996.
5. Dauby, P.C. et al., Linear Benard-Marangoni instability in rigid circular containers, Physical Review E, vol. 56(1), pp. 520-530, 1997.
5. Dijkstra, Henk, A., On the structure of cellular solutions in Rayleigh-Benard-Marangoni flows in small-aspect-ratio containers, J. Fluid Mechanics, vol. 243, pp.73-102, 1992.
6. Gebhart, B. et al., Buoyancy-Induced flows and Transport, Hemisphere Publishing Corporation, Washington, 1988.
7. Golovin, A.A. et al., Nonlinear evolution and secondary instabilities of Marangoni convection in a liquid-gas system with deformable interface, J. Fluid Mechanics, vol. 341, pp. 317-341, 1997.
8. Johnson, D. and Narayanan, R., Experimental observation of dynamic mode switching in interfacial-tension-driven convection near a codimension-two point, Physical Review E, vol. 54(4), pp. R3102-R3104, 1996.
9. Johnson, D., Narayanan R. and Dauby, P.C., The effect of Air Height on the pattern formation in Liquid-Air Bilayer Convection, Fluid Dynamics at Interface, Cambridge University Press, Cambridge, pp. 15-30, 1999.
10. Nield, D.A., Surface tension and buoyancy effects in cellular convection, J. Fluid Mechanics, vol. 19, pp. 341-352, 1964.
11. Prakash, A. and Koster, J.N., Steady Rayleigh- Benard Convection in a Two-Layer system of Immiscible Liquids, Transactions of the ASME, J Heat Transfer, vol. 118, pp. 366-373, 1996.
12. Prakash, A. et al., Flow Coupling mechanisms in two-layer Rayleigh-Benard convection, Experiments in Fluids, vol. 23, pp. 252-261, 1997.

13. Rasenat, S., Busse, F.H. and Rehberg, I., A theoretical and experimental study of double-layer convection, *J. Fluid Mechanics*, vol. 199, pp. 519-540, 1989.
14. Schatz, M.F. et al., Time-independent square patterns in surface-tension-driven Benard convection, *Physics of Fluids*, vol. 11(9), pp. 2577-2582, 1999.
15. Zaks, M.A., Auer, M., Busse, F.H., Undulating rolls and their instabilities in a Rayleigh-Benard layer, *Physical Review E*, vol. 53(5), pp. 4807-4819, 1996.
16. Zeren, R.W. and Reynolds, W.C., Thermal instabilities in two-fluid horizontal layers, *J. Fluid Mechanics*, vol. 53(2), pp. 305-327, 1972.

# Appendix A

## Numerical Simulation for Interface Temperature

### A.1 Design of Test Cell

This appendix throws light on the steady state calculation for the respective temperature drops in air and water for the two layer problem.

For the convective flow to be in 2-dimensional steady state regime for air and water in a two phase convection problem the Rayleigh numbers should fall in the flow regime given by *R. Krishnamurti* (1970), Figure 2.2. Individual Rayleigh numbers are calculated by using equation

$$Ra = \frac{g\beta\Delta T d^3}{\alpha\nu} \quad (A.1)$$

$$Ra = \frac{g\beta\Delta T d^3 \rho^2 c_p}{\mu\kappa} \quad (A.2)$$

where  $d$  is the half of the cavity height.

For this Here, the Nusselt numbers for air and water are calculated by using correlations given by Hollands *et al.* (1975). For air, the correlation is given by:

$$Nu_a = 1 + 1.44[1 - \frac{1708}{Ra}] + [(\frac{Ra}{5830})^{1/3} - 1] \quad (A.3)$$

And for water, the correlation is

$$Nu_w = 1 + 1.44[1 - \frac{1708}{Ra}] + [(\frac{Ra}{5830})^{1/3} - 1] + 2\frac{(Ra)^{1/3}}{140}[1 - \ln\frac{(Ra)^{1/3}}{140}] \quad (A.4)$$

Where the terms within square brackets are taken as zero if they have negative value. The additional term for water is suggested by Hollands *et al.* (1975) to be

due to the existence of thermals. For  $Ra \leq 1708$ , the heat across the fluid layers occurs by conduction and  $Nu=1$ .

By the law of conservation of energy in terms of heat given by  
 heat conducted through bottom plate=heat convected in water  
 =heat convected in air=heat conducted in top plate

It is assumed that the thickness of the top and bottom surfaces are much smaller than that of the fluid layers. Hence temperature gradients occur only due to convection in fluids. Using

heat convected in water=heat convected in air

$$h_w(T_h - T_i)A = h_a(T_i - T_c)A \quad (A.5)$$

where

$$h_w = \frac{Nu_w K_w}{d_w} \quad (A.6)$$

and

$$h_a = \frac{Nu_a K_a}{d_a} \quad (A.7)$$

where  $d_w$  and  $d_a$  are the characteristic length of the fluids. In the case of cavity filled with half water characteristic lengths are equal ( $d_w = d_a$ ). Hence

$$Nu_w K_w (T_h - T_i) = Nu_a K_a (T_i - T_c) \quad (A.8)$$

The interface temperature  $T_i$  is calculated from the above equation. For a given cavity height and top and bottom wall temperatures, one can get the properties of the fluids, since the properties of the fluids such as  $\rho$ ,  $c_p$ ,  $\mu$ ,  $K$ ,  $\beta$ ,  $\alpha$ ,  $\nu$ , depend on temperature. Curve fitting is done by using equation:

$$y = a_0 + a_1 T + a_2 T^2 \quad (A.9)$$

where  $y$  can be  $\rho$ ,  $c_p$ ,  $\mu$ ,  $K$ ,  $\beta$ ,  $\alpha$ , and  $\nu$ . For air  $\beta = \frac{1}{T_{\text{average}}}$ . By this the properties of air and water are obtained for the required temperature. For air the properties are taken at the average temperature  $\frac{T_c + T_i}{2}$ . For water the average temperature is  $\frac{T_i + T_h}{2}$ , where  $T_c$  is the cold (upper) wall temperature and  $T_h$  is the hot (lower) wall temperature,  $T_i$  is the interface temperature.

After calculating the interface temperature, number of fringes in water and air can be calculated by using formula

$$\text{number of fringes in water} = \frac{(T_h - T_i)}{\Delta T_{\epsilon(\text{water})}} \quad (A.10)$$



and

$$\text{number of fringes in air} = \frac{(T_i - T_c)}{\Delta T_{\epsilon(\text{air})}} \quad (\text{A.11})$$

respectively.

Using above formulation for different cavity heights and for different surface temperatures Rayleigh numbers, Prandtl numbers, interface temperatures are calculated for water and air, which are shown in Table-A.1, Table-A.2 and Table-A.3.

Table-A.1

h	Th	Tc	Ra (air)	Ra (water)	Nu (hot)	Nu (cold)	Ti
20 mm	20	10	1116	2538	2.120	1.0	19.81
	30	20	954	3907	2.527	1.0	29.84
	35	15	1913	8992	3.186	1.155	34.70

Table-A.2

h	Th	Tc	Ra (air)	Ra (water)	Nu (hot)	Nu (cold)	Ti
25 mm	20	10	2179	5085	2.717	1.311	19.80
	30	20	1865	7215	2.996	1.121	29.85
	35	15	3725	21830	3.923	1.779	34.63

Table-A.3

h	Th	Tc	Ra (air)	Ra (water)	Nu (hot)	Nu (cold)	Ti
30 mm	20	10	3756	9983	3.265	1.785	19.78
	30	20	3212	15350	3.629	1.674	29.81
	35	25	2975	18177	3.769	1.614	34.82

From the tables it is observed that the temperature drop in air is much higher than that of water.

# Appendix B

## Numerical Simulation of Fluid Flow and Heat Transfer

The present appendix is concerned with the numerical solution of the buoyancy-driven flow in a fluid filled square cavity. The dimensions of the test cell are the same as considered in the experimental work. The numerical solutions have been presented for  $Ra=34,200$  and  $Pr=0.7$  (air) and for  $Ra=10,000$  and  $Pr=0.05$  (liquid metal). Open as well as closed cavities have been considered.

Natural convection in the fluid is governed by the laws of conservation of mass, momentum and energy. These are mathematically represented by the continuity equation, Navier-Stokes equation and the energy equation, which are represented in 2-dimensional cartesian system as follows:

Continuity:

$$\frac{\partial u}{\partial x} + \frac{\partial v}{\partial y} = 0 \quad (B.1)$$

$x$ -momentum:

$$\rho[u\frac{\partial u}{\partial x} + v\frac{\partial u}{\partial y}] = -\frac{\partial p}{\partial x} + \mu\nabla^2 u \quad (B.2)$$

$y$ -momentum:

$$\rho[u\frac{\partial v}{\partial x} + v\frac{\partial v}{\partial y}] = -\frac{\partial p}{\partial y} + \mu\nabla^2 v - (\rho - \rho_0)g \quad (B.3)$$

Energy:

$$\rho c_p[u\frac{\partial T}{\partial x} + v\frac{\partial T}{\partial y}] = k\nabla^2 T \quad (B.4)$$

The above equations have been recast in a nondimensional form using the following quantities:

**Dimensionless temperature:**

$$\theta = \frac{T - T_c}{T_h - T_c} \quad (B.5)$$

Dimensionless length:

$$\mathbf{x} = \left( \frac{x}{h}, \frac{y}{h} \right) \quad (\text{B.6})$$

Dimensionless velocity:

$$\mathbf{u} = \frac{(u, v)}{\nu/h} \quad (\text{B.7})$$

Dimensionless pressure:

$$P = \frac{p + \rho_0 g y}{\rho(\nu/h)^2} \quad (\text{B.8})$$

The non-dimensional parameter responsible for the buoyancy induced flows in the cavity namely the **Grashoff** number is defined as

$$\text{Gr} = \frac{\text{Ra}}{\text{Pr}} \quad (\text{B.9})$$

where Ra is the Rayleigh number and is defined as

$$\text{Ra} = \frac{g\beta(T_h - T_c)h^3}{\nu\alpha} \quad (\text{B.10})$$

and Pr is the Prandtl number defined as

$$\text{Pr} = \frac{\nu}{\alpha} \quad (\text{B.11})$$

Biot number Bi is defined as

$$\text{Bi} = \frac{h(V/A)}{k} \quad (\text{B.12})$$

Marangoni number Ma is defined as

$$\text{Ma} = \frac{\sigma\Delta TH}{\mu\alpha} \quad (\text{B.13})$$

To solve the governing equations for flow and temperature, a  $\psi-\omega-\theta$  formulation has been employed. The  $u$  and  $v$  velocities have been defined as

$$u = \frac{\partial\psi}{\partial y} \quad (\text{B.14})$$

$$v = -\frac{\partial\psi}{\partial x} \quad (\text{B.15})$$

One can now derive the following: Stream Function Equation:

$$\text{Since, } \omega = \frac{\partial v}{\partial x} - \frac{\partial u}{\partial y} \quad (\text{B.16})$$

$$\omega = -\left(\frac{\partial^2\psi}{\partial x^2} + \frac{\partial^2\psi}{\partial y^2}\right) \quad (\text{B.17})$$

Vorticity Equation:

$$u \frac{\partial \omega}{\partial x} + v \frac{\partial \omega}{\partial y} = \left( \frac{\partial^2 \omega}{\partial x^2} + \frac{\partial^2 \omega}{\partial y^2} \right) + \left( \frac{Ra}{Pr} \right) \frac{\partial \theta}{\partial x} \quad (B.18)$$

Energy Equation:

$$u \frac{\partial \theta}{\partial x} + v \frac{\partial \theta}{\partial y} = \frac{1}{Pr} \left( \frac{\partial^2 \theta}{\partial x^2} + \frac{\partial^2 \theta}{\partial y^2} \right) \quad (B.19)$$

For computation of the stream function, vorticity and temperature, three geometries have been studied: (1) cavity is closed, (2) open from the top, and (3) the surface tension term is included at the free surface. The boundary conditions for the three sides *i.e.*, for the lower wall and the two side walls are identical for all the three cases. But for the top walls the boundary conditions are different. The top wall boundary conditions for all the cases can be represented as

CLOSED CAVITY:

$$\psi = 0 \quad (B.20)$$

$$\omega = -\frac{\partial^2 \psi}{\partial y^2} \quad (B.21)$$

$$-\frac{\partial \theta}{\partial y} = Bi\theta \quad (B.22)$$

OPEN CAVITY:

$$\psi = 0 \quad (B.23)$$

$$\omega = 0 \quad (B.24)$$

$$-\frac{\partial \theta}{\partial y} = Bi\theta \quad (B.25)$$

OPEN CAVITY with SURFACE TENSION:

$$\psi = 0 \quad (B.26)$$

$$\omega = Ma \frac{\partial \theta}{\partial x} \quad (B.27)$$

$$-\frac{\partial \theta}{\partial y} = Bi\theta \quad (B.28)$$

The remaining boundary conditions are as follows:

Bottom Wall:

$$\psi = 0 \quad (B.29)$$

$$\omega = -\frac{\partial^2 \psi}{\partial y^2} \quad (B.30)$$

$$\theta = 1 \quad (\text{B.31})$$

Side Walls:

$$\psi = 0 \quad (\text{B.32})$$

$$\omega = -\frac{\partial^2 \psi}{\partial x^2} \quad (\text{B.33})$$

$$\frac{\partial \theta}{\partial x} = 0 \quad (\text{B.34})$$

At All Corners:

$$\omega = -2.0 \frac{\partial^2 \psi}{\partial r^2} \quad (\text{B.35})$$

The following initial conditions have been applied:

$$\psi = 0 \quad (\text{B.36})$$

$$\omega = 0 \quad (\text{B.37})$$

$$\theta = 1 - y \quad (\text{B.38})$$

The governing equations have been discretised using an implicit finite difference scheme. A uniform grid of  $81 \times 81$  is used. The convective terms of the momentum equations are discretized using the 2nd order upwind scheme while central difference discretisation has been applied to the diffusive terms. The matrix inversion is by the Gauss-Siedel method. The results of numerical simulation for  $Ra=34,200$  and  $Pr=0.7$  and for  $Ra=10,000$  and  $Pr=0.05$  have been presented below. For these two fluids three cases are considered:

1. Cavity is closed,
2. Cavity is open at the top surface,
3. Cavity is open, but surface-tension on the free surface is non zero.

Figure B.1(a), Figure B.1(b), Figure B.1(c) and Figure B.1(d) show the numerically generated velocity vectors, streamlines, isovorticities and isotherms for  $Ra=34,200$  and  $Pr=0.7$  for a closed cavity. As seen from the plots of the isotherms, the fluid accelerates on one side of the mid-plane, reaches a maximum at this point and decelerates to small values on the other side of the cavity, as it approaches the side walls. The overall flow pattern in the cavity is hence unicellular with the roll moving in a clockwise direction.

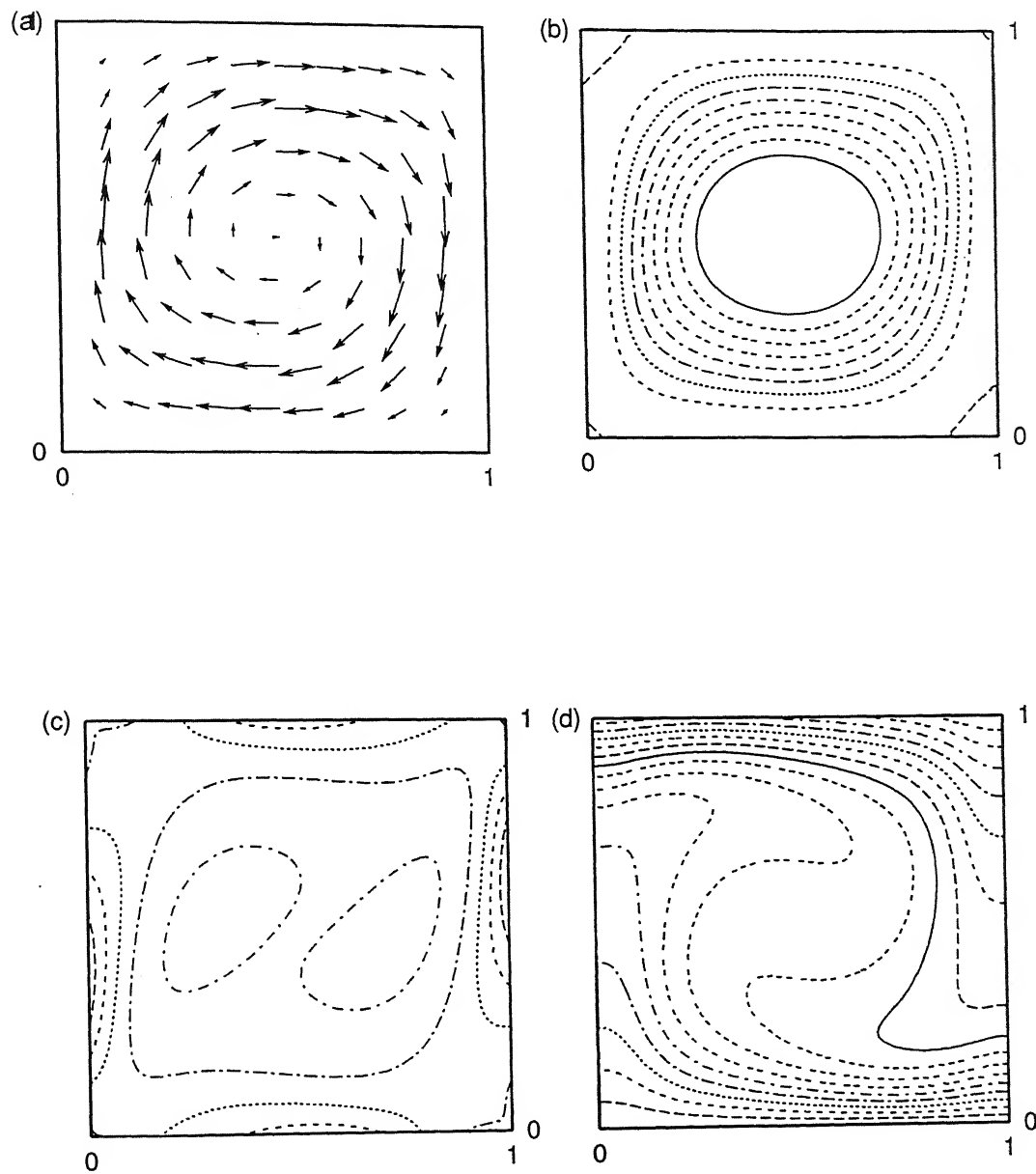


Figure B.1: Numerically generated (a) Velocity Vectors, (b) Streamlines, (c) Isovorticities, and (d) Isotherms for  $Ra=34,200$  and  $Pr=7.0$  for a Closed cavity

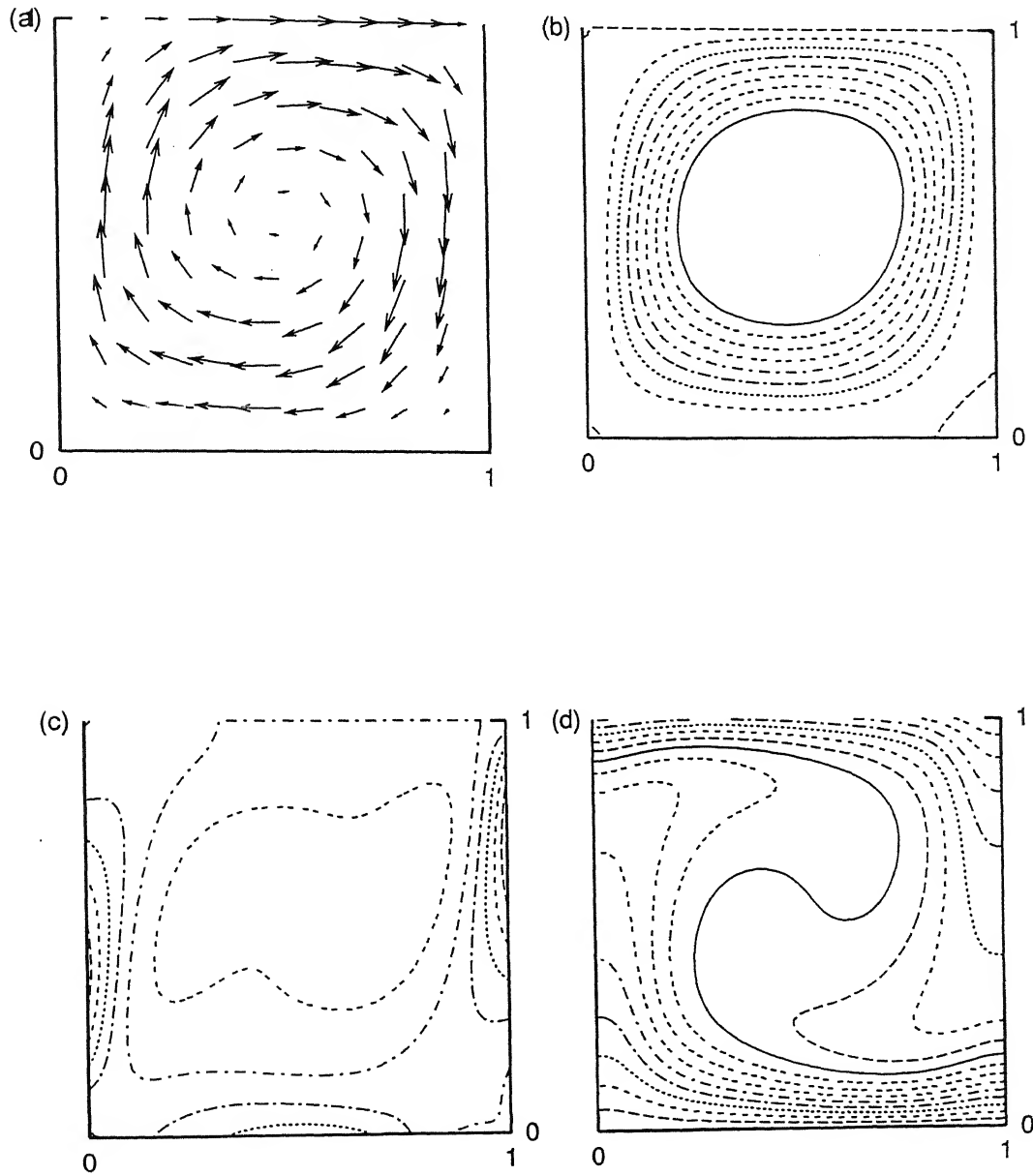


Figure B.2: Numerically generated (a) Velocity Vectors, (b) Streamlines, (c) Isovorticities, and (d) Isotherms for  $Ra=34,200$  and  $Pr=7.0$  for an Open cavity

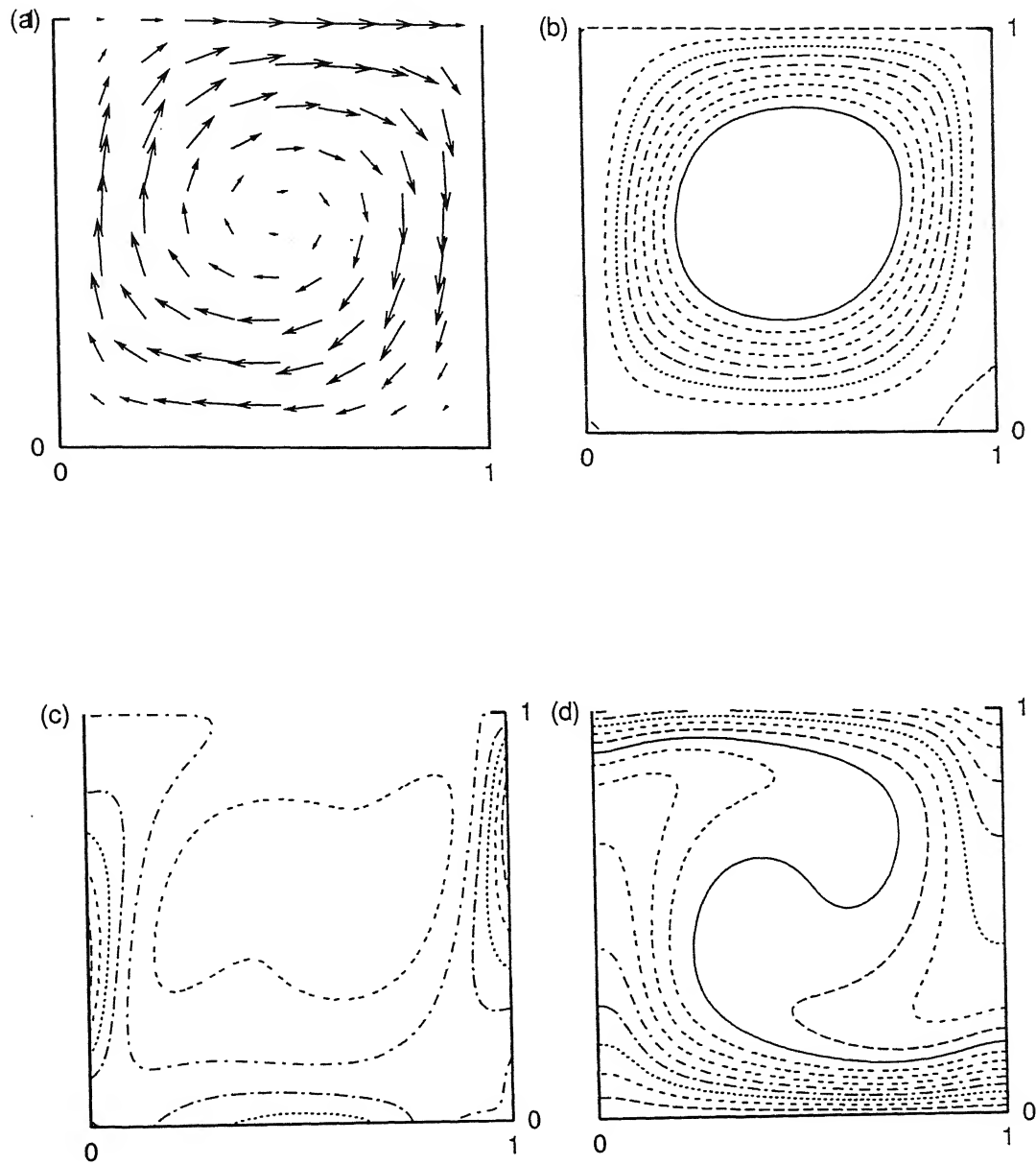


Figure B.3: Numerically generated (a) Velocity Vectors, (b) Streamlines, (c) Isovorticities, and (d) Isotherms for  $Ra=34,200$  and  $Pr=7.0$  for an Open cavity with Surface-Tension



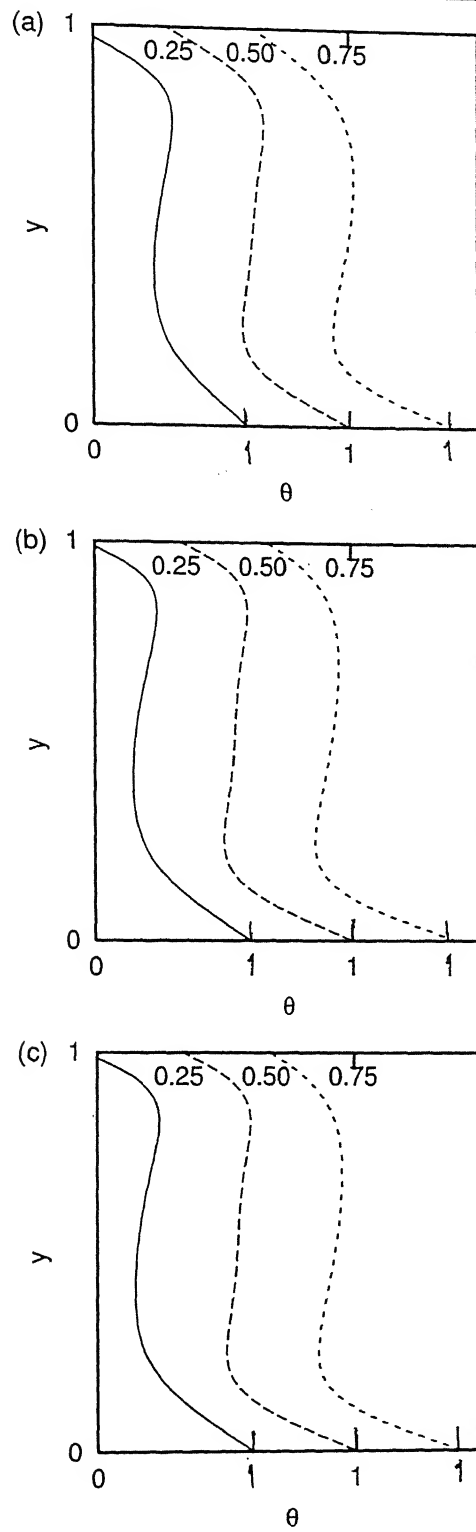


Figure B.4: Temperature Profiles at 3 columns in (a) Closed cavity  
 (b) Open cavity without and (c) with Surface-Tension at  $x=0.25$ ,  
 $0.50$ ,  $0.75$  for  $Ra=34,200$ ,  $Pr=0.70$ ,  $Bi=10.0$  and  $Ma=1.0$

Figure B.2(a), Figure B.2(b), Figure B.2(c) and Figure B.2(d) show the numerically generated velocity vectors, streamlines, isovorticities and isotherms for  $Ra=34,200$  and  $Pr=0.7$  for an open cavity without considering the effect of surface tension. The overall flow pattern in the cavity is unicellular with the roll moving in a clockwise direction.

A value of  $Pr=0.7$  is generally seen for a fluid medium in the gaseous phase. If the working fluid is a gas, free surface boundary conditions as discussed in the present Appendix are not applicable. There is partial evidence that the flow patterns in gases as well as liquids are quite similar, particularly at lower Rayleigh numbers. For this reason, the flow fields computed with  $Pr=0.7$  can be expected to be structurally similar to those in a liquid such as water, whose Prandtl number is in the range of 5-10. The above analogy can not be extended to low Prandtl number fluids such as liquid metals.

Figure B.3(a), Figure B.3(b), Figure B.3(c) and Figure B.3(d) show the numerically generated velocity vectors, streamlines, isovorticities and isotherms for  $Ra=34,200$  and  $Pr=0.7$  for an open cavity including the effect of surface tension. The overall flow pattern in the cavity is unicellular with the roll moving in a clockwise direction. Figure B.4 shows the temperature variation as a function of vertical coordinates at three different equally spaced columns along the length of the cavity for all the three cases discussed above.

## B.1 Numerical Simulation for $Ra=10,000$ and $Pr=0.05$

The results of numerical simulation for  $Ra=10,000$ ,  $Pr=0.05$  and  $Bi=10.0$  have been presented in this section. It may be noted that a low prandtl number is encountered with liquid metals.

Figure B.5(a), Figure B.5(b), Figure B.5(c) and Figure B.5(d) show the numerically generated velocity vectors, streamlines, isovorticities and isotherms for  $Ra=10,000$ ,  $Pr=0.05$  and  $Bi=10.0$  for a closed cavity. As seen from the plots of the isotherms, the fluid near the walls accelerates on one side of the mid-plane, reaches a maximum at this point and decelerates to small values on the other side of the cavity, as it approaches the side walls. The overall flow pattern in the cavity is hence unicellular with the roll moving in an anticlockwise direction.

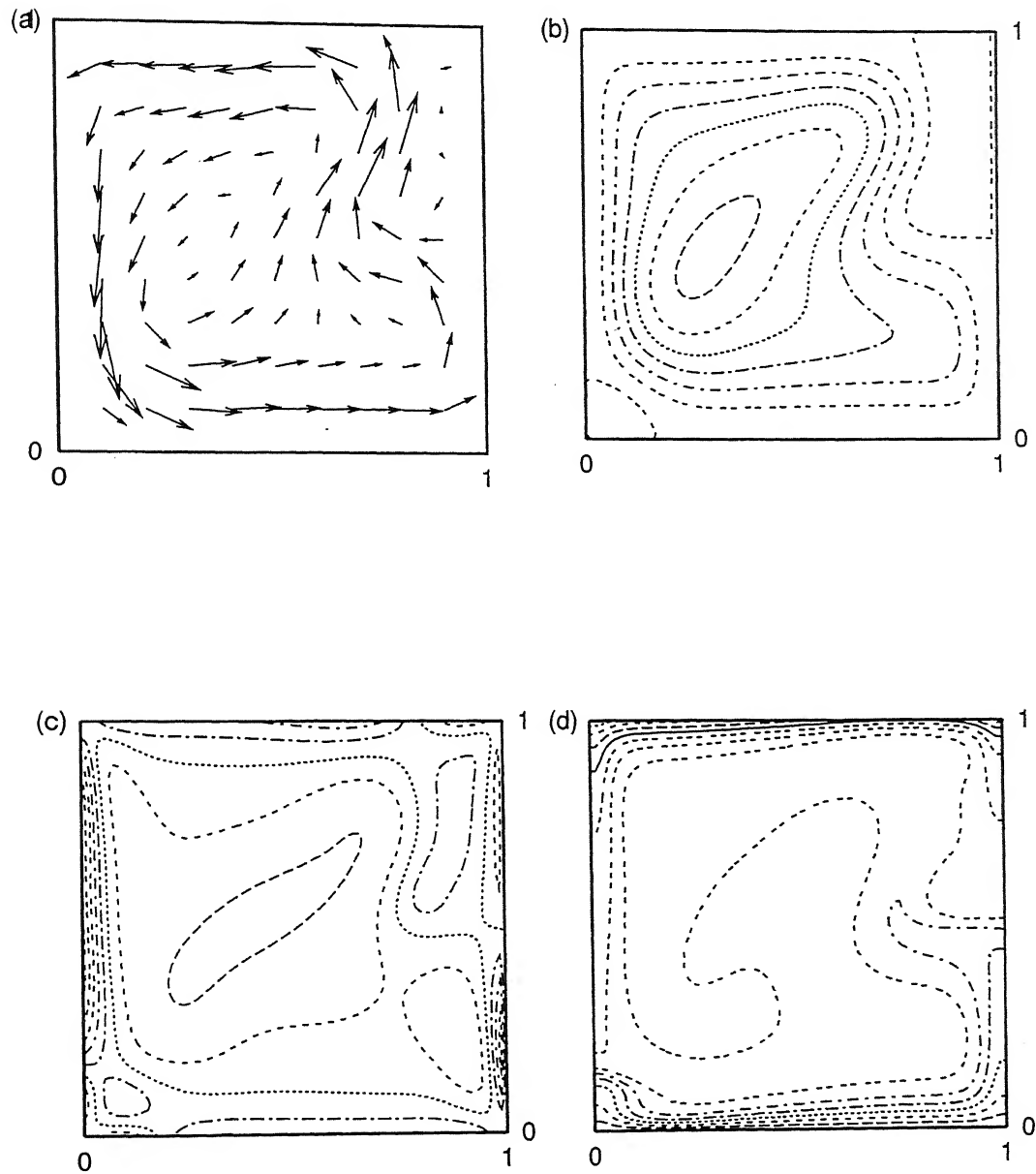


Figure B.5: Numerically generated (a) Velocity Vectors, (b) Streamlines, (c) Isovorticities, and (d) Isotherms for  $RA=10,000$  and  $PR=0.05$  for a Closed cavity

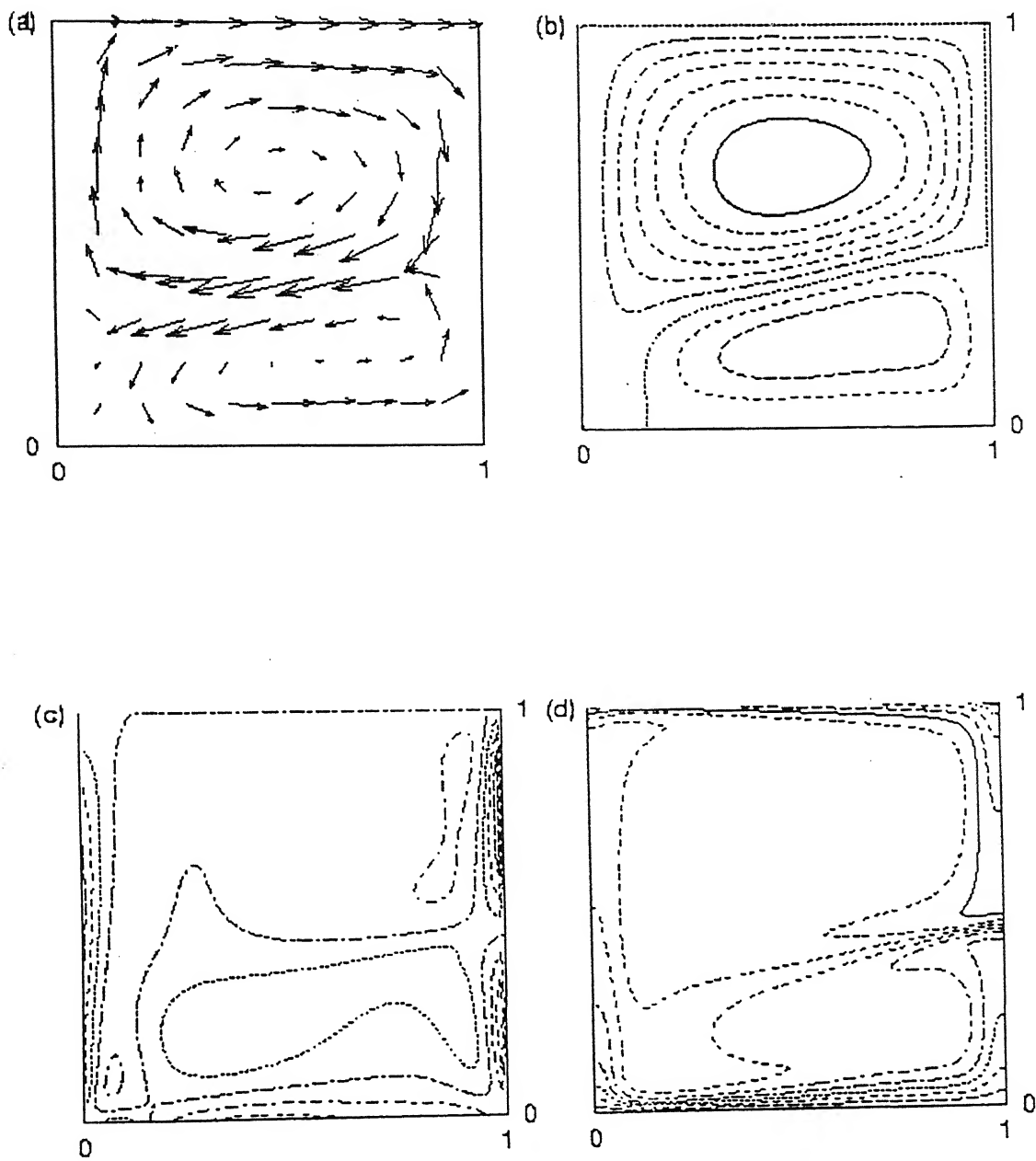


Figure B.6: Numerically generated (a) Velocity Vectors, (b) Streamlines, (c) Isovorticities, and (d) Isotherms for  $Ra=10,000$  and  $Pr=0.05$  for an Open cavity

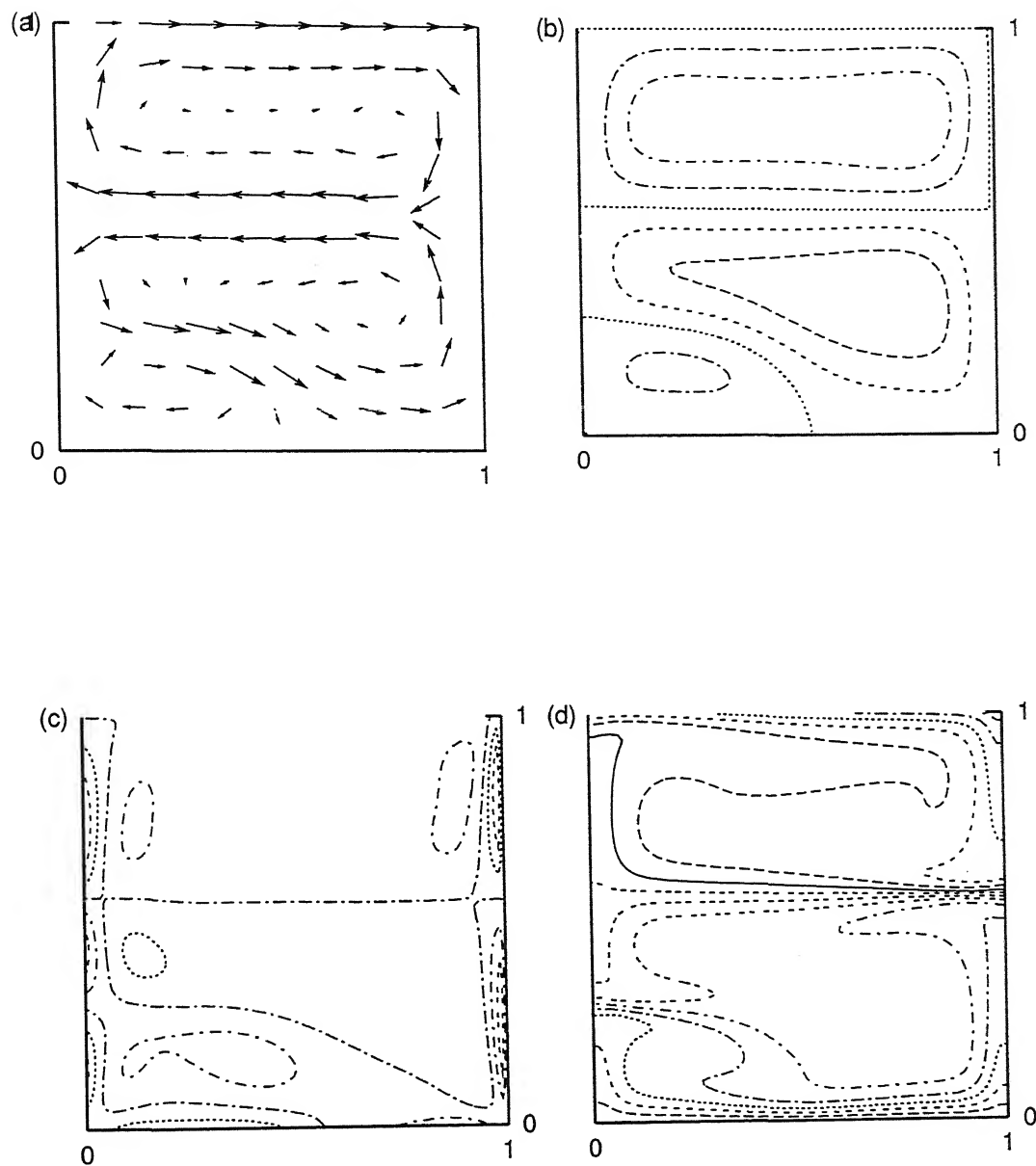


Figure B.7: Numerically generated (a) Velocity Vectors, (b) Streamlines, (c) Isovorticities, and (d) Isotherms for  $Ra=10,000$  and  $Pr=0.05$  for an Open cavity with Surface-Tension

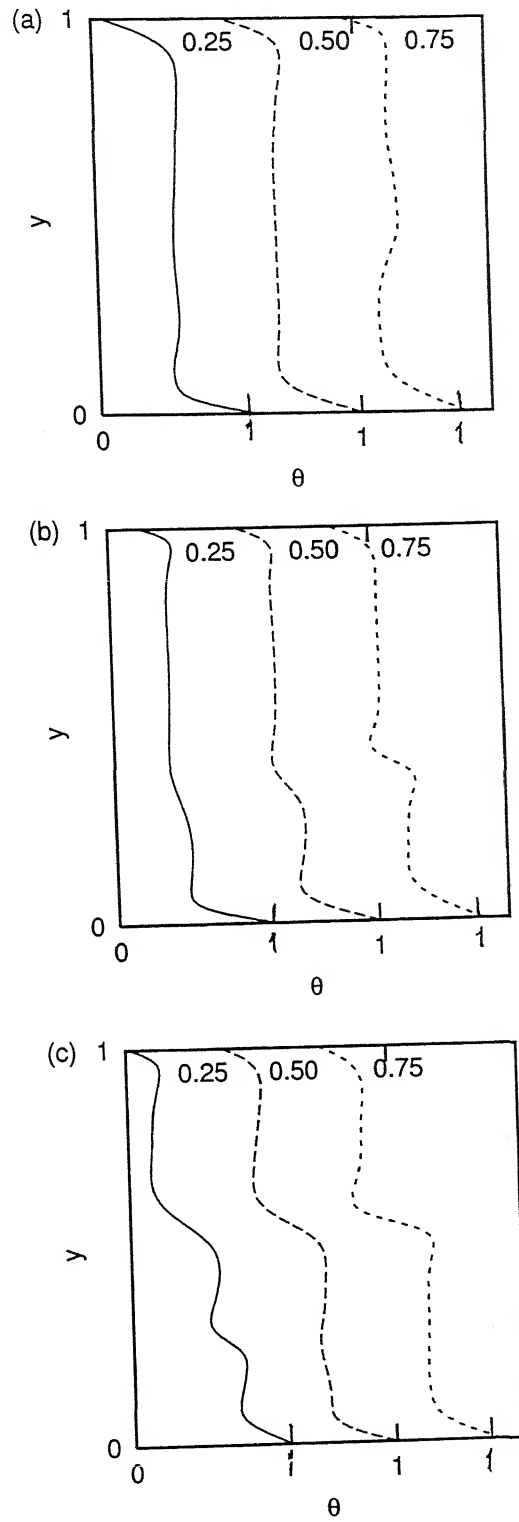


Figure B.8: Temperature Profiles at 3 columns in (a) Closed cavity  
 (b) Open cavity without and (c) with Surface-Tension at  $x=0.25, 0.50, 0.75$  for  $Ra=10,000$ ,  $Pr=0.05$ ,  $Bi=10.0$  and  $Ma=1.0$

However smaller cells are also visible here near the top right and lower left corners.

Figure B.6(a), Figure B.6(b), Figure B.6(c) and Figure B.6(d) show the numerically generated velocity vectors, streamlines, isovorticities and isotherms for  $Ra=10,000$  and  $Pr=0.05$ ,  $Bi=10.0$  for an open cavity without considering the effect of surface tension. The overall flow pattern in the cavity is bicellular with two rolls moving in clockwise and anticlockwise directions.

Figure B.7(a), Figure B.7(b), Figure B.7(c) and Figure B.7(d) show the numerically generated velocity vectors, streamlines, isovorticities and isotherms for  $Ra=10,000$ ,  $Pr=0.05$  and  $Bi=10.0$  for an open cavity including the effect of surface tension. The overall flow pattern in the cavity is bicellular with two rolls moving in clockwise and anticlockwise directions. The strength and the size of the rolls have now changed in relation to Figures B.6(a-d), the lower roll being more prominent.

Figure B.8 shows the temperature profiles for liquid metal for closed, open without and with surface-tension for equally spaced three columns.

## B.2 Effect of Surface-Tension on the shape of the Free Surface

Figure B.9(a) and Figure B.9(b) show the surface deformation due to surface-tension for a fluid with  $Pr=7.0$ , a cavity height  $h=16.05\text{mm}$  with  $\frac{d\sigma}{dT}=0$ , that is for constant  $\sigma$  and for  $\frac{d\sigma}{dT}=\text{constant}$  that is for nonconstant  $\sigma$  respectively. For water, the contact angle at the cavity walls was taken to be 0.78 radians. The figures show that the displacement of free surface owing to convection is 5.4 mm for constant surface-tension and 6.9 mm for non-constant surface-tension. Figure B.10(a) and Figure B.10(b) show the surface deformation due to surface-tension for a fluid with  $Pr=0.05$ , a cavity height  $h=16.05\text{ mm}$  with  $\frac{d\sigma}{dT}=0$ , that is for constant  $\sigma$  and for  $\frac{d\sigma}{dT}=\text{constant}$  that is for nonconstant  $\sigma$  respectively. For a liquid metal, the contact angle at the cavity wall was taken to be 2.34 radians. The calculations show that the displacement of free surface owing to convection is 6.9 mm for constant surface-tension and 7.0 mm for non-constant surface-tension.

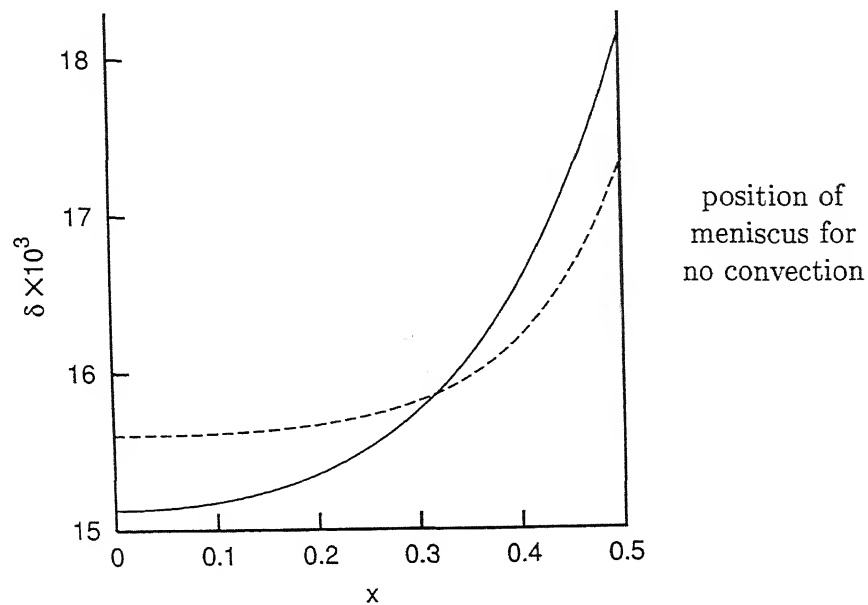


Figure B.9(a): Effect of Constant Surface-Tension on the displacement of the free surface owing to convection in water,  $Ra=34,200$ ,  $Pr=7.0$ ,  $Bi=10.0$ ,  $Ma=1.0$

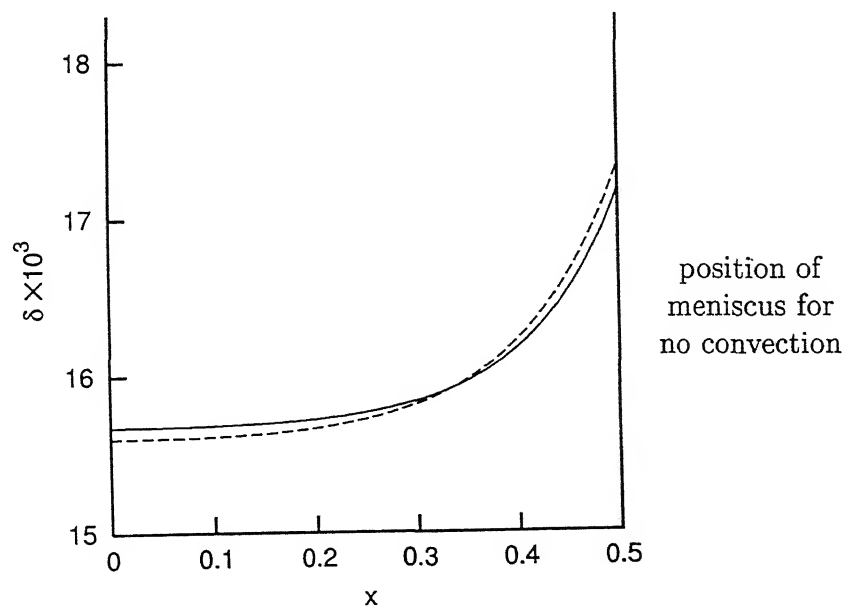


Figure B.9(b): Effect of Non-Constant Surface-Tension on the displacement of the free surface owing to convection in water,  $Ra=34,200$ ,  $Pr=7.0$ ,  $Bi=10.0$ ,  $Ma=1.0$



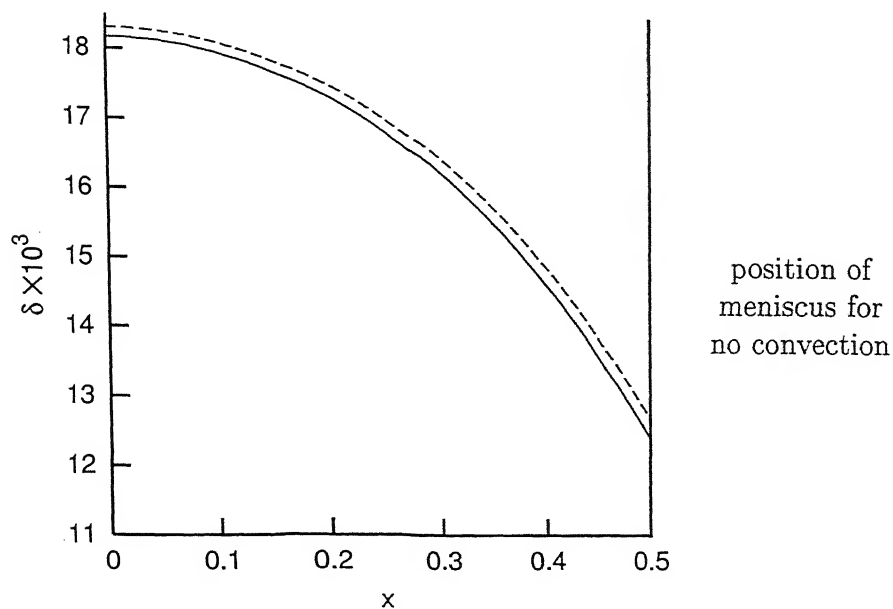


Figure B.10(a): Effect of Constant Surface-Tension on the displacement of the free surface owing to convection in a liquid metal,  $Ra=10,000$ ,  $Pr=0.05$ ,  $Bi=10.0$ ,  $Ma=1.0$

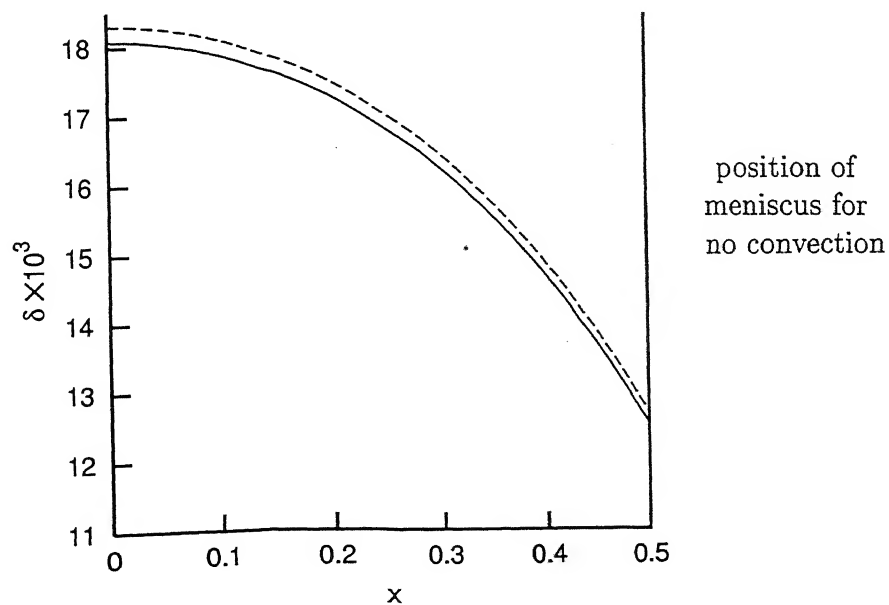


Figure B.10(b): Effect of Non-Constant Surface-Tension on the displacement of the free surface owing to convection in a liquid metal,  $Ra=10,000$ ,  $Pr=0.05$ ,  $Bi=10.0$ ,  $Ma=1.0$